12-2021

# Applications in Multi-band Isolation of Spectra with Data-Adaptive Sub-banding (MIDAS): Using Multi-criteria Decision Analysis to Optimize MIDAS-based De-noising Methods When Processing Infrasound and Other Signals of Interest

Everett Raymond Coots

# Applications in Multi-band Isolation of Spectra with Data-Adaptive Sub-banding (MIDAS): Using Multi-criteria Decision Analysis to Optimize MIDAS-based De-noising Methods When Processing Infrasound and Other Signals of Interest

by Everett Raymond Coots

Bachelor of Science in Electrical Engineering

Florida Institute of Technology

1993

Master of Science in Systems Engineering

Florida Institute of Technology

2007

Master of Science in Engineering Management

Florida Institute of Technology

2008

A dissertation submitted to the College of Engineering and Science

at the Florida Institute of Technology

in partial fulfillment of the requirements for the degree of

Doctor of Philosophy

in

Systems Engineering

Melbourne, Florida

December 2021

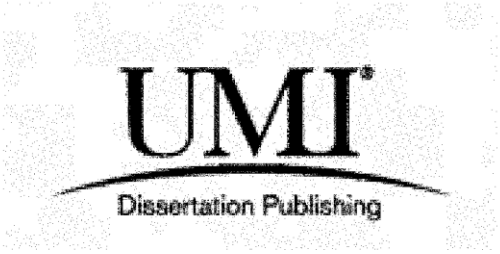

"Applications in Multi-band Isolation of Spectra with Data-Adaptive Sub-banding (MIDAS): Using Multi-criteria Decision Analysis to Optimize MIDAS-based De-noising Methods When Processing Infrasound and Other Signals of Interest"

A dissertation by Everett Raymond Coots

Approved as to style and content.

---

William W. Arrasmith, Ph.D.

Professor, College of Engineering and Sciences

Major Advisor

---

Adrian M. Peter, Ph.D.

Associate Professor, College of Engineering and Sciences

---

Luis D. Otero, Ph.D.

Associate Professor, College of Engineering and Sciences

---

Carlos E. Otero, Ph.D.

Associate Professor, College of Engineering and Sciences

---

Philip Bernhard, Ph.D.

Associate Professor and Department Head, College of Engineering and Sciences

# Abstract

Applications in Multi-band Isolation of Spectra with Data-Adaptive Sub-banding (MIDAS): Using Multi-criteria Decision Analysis to Optimize MIDAS-based De-noising Methods When Processing Infrasound and Other Signals of Interest

By Everett Raymond Coots

Major Advisor: William W. Arrasmith, Ph.D.

The ever-present challenge faced by the signal processing analyst is to get more from the available data, whether it be exploiting the same data in new ways to garner new information, or simply to increase the confidence in existing qualitative metrics. Traditional techniques include filtering (to improve the signal to noise ratio of detected signals or images or to isolate and possibly remove interfering signals), feature detection/extraction (identifying key characteristics within the signal) and signal decomposition (identification of dominant signals of interest relative to noise terms). Current research by our team began with an emphasis on the filtering of signals of interest within the infrasound band but has been shown to also be effective in other applications including image processing. The Multi-stage Isolation of Spectra with Data-Adaptive Sub-banding (M.I.D.A.S.) filter begins with a wavelet pre-processing stage and follows with a spectral sub-banding stage for isolation of

key signal content. The MIDAS filter is a coherent filter, so the filtering of a complex input produces a phase-preserved complex output. With many other infrasound and seismic data filtering tools such as the Pure State Filter [Olsen, 2009], a real-valued time-domain input is required and thus no phase information can be extracted from the filtered output data set. A typical signal processing scenario where phase preservation is critical is image processing. If the applied filter distorts or even destroys the phase data it will be impossible to correctly recover the image. Both qualitative and quantitative image quality metrics are used within this research and demonstrate that the MIDAS filter is effective at removing channel noise artifacts from images while preserving the phase information. Such noise artifacts might be caused by bit errors during the transmission of an image, or by quantization errors during the digitization or capture of the image.

# Table of Contents

## Contents

# List of Figures

# List of Tables

# Acknowledgement

Many professional and academic peers and colleagues have contributed time and energy to support the execution of this research effort. I would like to thank Dr. Dean Clauter of the Air Force Technical Applications Center (AFTAC) for providing valuable source data and supporting numerous technical discussions over the years. I thank Eric Skowbo of Northop Grumman Corporation for participating in the industry partnership with the Florida Institute of Technology and connecting our research team with his infrasound research as well as helping us secure our own infrasound sensor subsystem. Eric and his team not only provided numerous seismic and infrasound datasets reviewed during this research, but I would like to specifically thank him for providing the raw data and ground truth data associated with the U.S. Coast Guard boat experiment used in section 5.3.1 of this dissertation. I would also like to thank the members of my committee for their guidance and feedback through this process: Dr. Adrian Peter, Dr. Luis Otero and Dr. Carlos Otero. I would especially like to thank my advisor, Dr. William Arrasmith for his outstanding leadership, skillful mentoring and thoughtful insights throughout the process.

# Dedication

I would like to dedicate this work to my family. This long and difficult journey could not have been completed without the love and support of my wife and children.

"*It does not matter how slowly you go, so long as you do not stop*"

-Confucius

# 1 Introduction

## 1.1 Research Motivation

The analysis of infrasound and seismic signals of interest presents a host of challenges to the signal processing analyst. The desired information may be obscured within the input data due to the presence of unwanted noise and interfering signals. The environment being measured may be cluttered with other signal sources that are not of interest, yet are in band and are captured by the sensor(s) along with the desired information. Additionally, the acquisition system itself may introduce noise into the measured data in the form of sensor noise, Analog/Digital conversion noise, or compression noise. The task of the signal processing analyst is to examine this ensemble of data and noise and extract that which is of interest. This is typically done with various filtering techniques to help isolate the signals while reducing the noise, thus improving the signal-to-noise ratio of the measured data. Additional processing may be employed to identify, isolate and exploit key characteristics of the signal through feature extraction techniques such as neural networks. This research is focused on the filtering aspect of the signal processing flow and presents a new technique for improving the signal-to-noise ratio of sensor system data. When used as a pre-filter in conjunction with canonical signal processing tools, the MIDAS filter

can improve the performance of existing tools relative to standard filtering techniques such as band-pass filtering.

Early infrasound data analysis tools such as Matseis often missed, or under-reported infrasound events because detections and the associated arrival azimuths were calculated using F-K (frequency-wavenumber) analysis which is prone to spatial aliasing [Garces, et. al.]. The low SNR of these signals made accurate detection challenging and many arrivals went unreported as a result. The MIDAS filter is shown to improve the detection capability of these tools when used to pre-process the input data.

## 1.2 Infrasound Overview

Infrasound waves occupy the lower regions of the acoustic spectrum (0.01-20Hz) and are below the range of human hearing which is typically said to be 20Hz-20KHz. Figure 1-1 below shows the infrasound pressure levels versus frequency. A convenient aspect of an infrasound signal's low frequency is the long propagation duration due to the low atmospheric attenuation. See Figure 1-2. This makes detection of infrasound events at the regional or even global level possible.

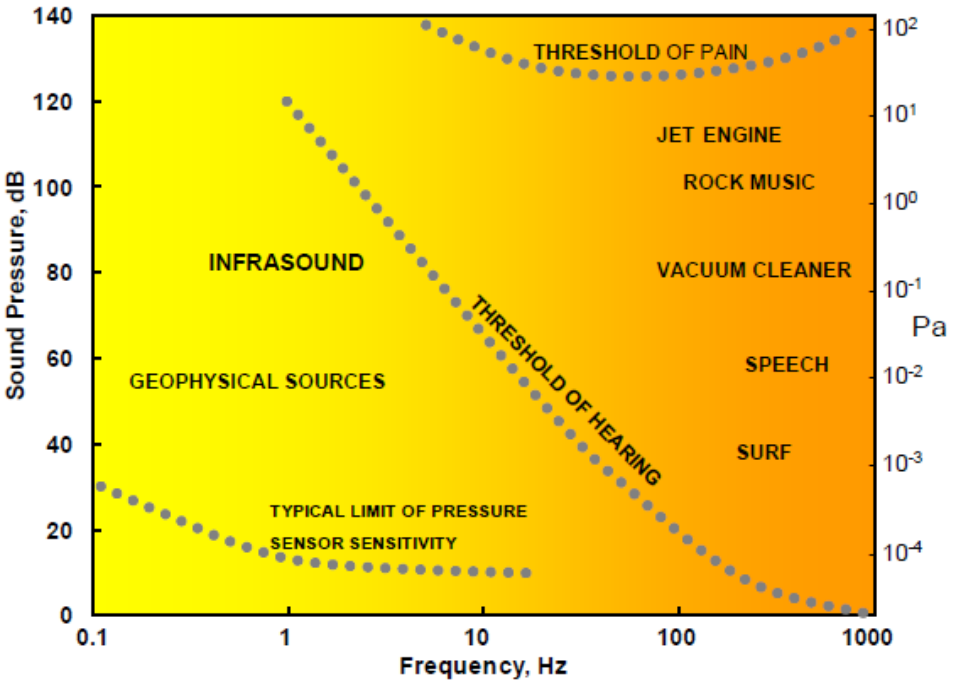


Figure 1-1 Sound pressure amplitude as a function of frequency compared with the threshold of human hearing at lower frequencies. [Bedard and Georges, 2000]

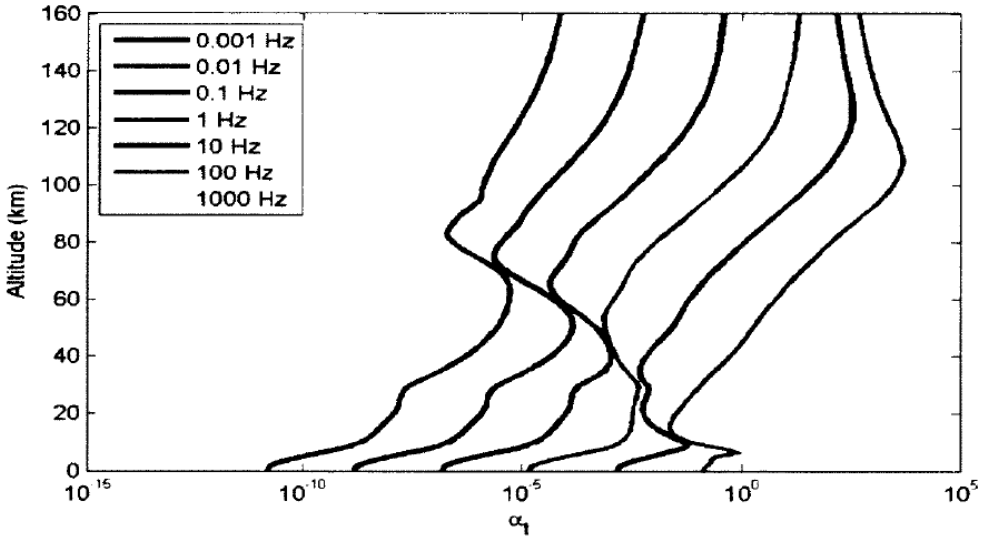


Figure 1-2 Infrasound Attenuation Factor, α vs. Altitude [Bass, 2006]

In addition to the low attenuation, Infrasound is able to travel over very large distances due to the various thermal gradients in the atmosphere called “Ducts”. Since the speed of sound varies with the changes in temperature as a function of altitude (see Figure 1-3 below), these ducts are created in the atmosphere which support the propagation of the infrasonic energy waves. This propagation is subject to attenuation and dispersion due to air temperature and density as well as the direction and velocity of the prevailing winds.

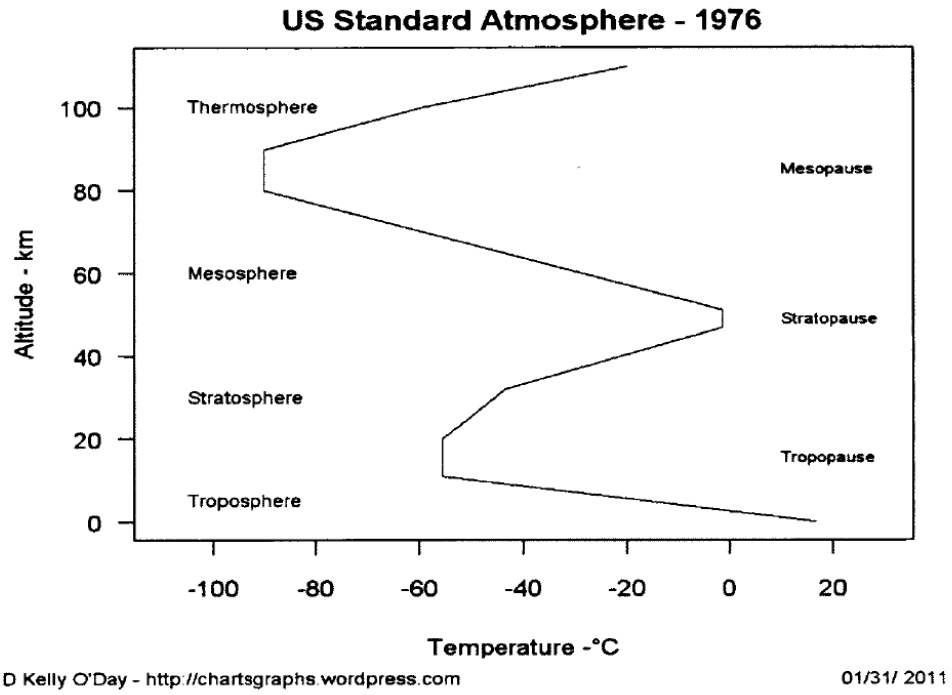


Figure 1-3 Atmospheric Temperature vs. Altitude [O'Day, 2011]

Sources of infrasound can be environmental (volcanos, earthquakes, meteors, tornados)[Beddard, 2005, Hale, 2010, Farges, 2010, Shao, 2016], natural (such as elephants, giraffes and whales) [Berchok, 2006, Le Pichon, 2002, and Wijayakulasooriya, 2011] or man-made (rockets, missiles, explosions, aircraft, land vehicles, etc.) [McLaughlin, Szuberla, 2009]. Figure 1-4 below shows examples of the wide variety of sources that may produce infrasound signals of interest. In some cases these signals are monitored to satisfy humanitarian and peacekeeping objectives such as severe weather and volcano eruption detection and monitoring

[Mutschlecner, 2005, Pepyne, 2011, Sciotto, 2006]. In some cases, infrasound signals are monitored for intelligence gathering [Kijima, 2018].

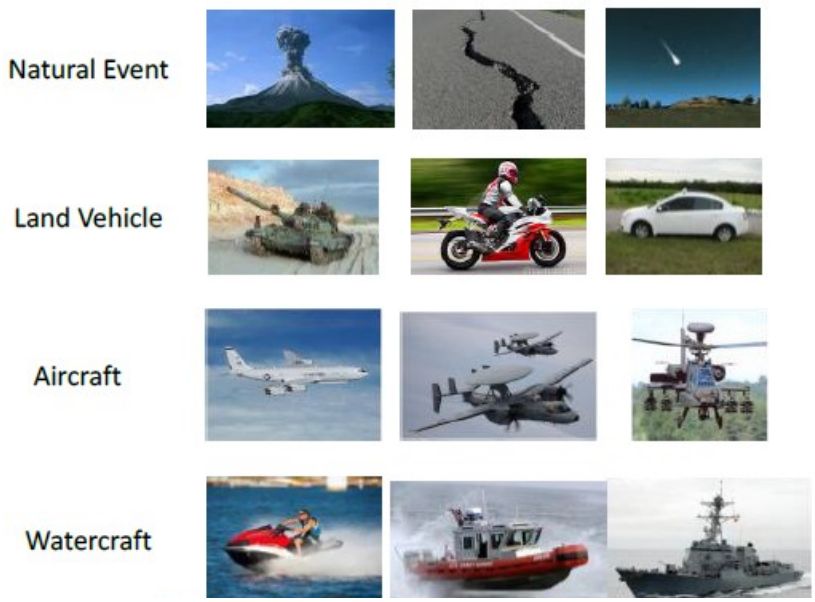


Figure 1-4 Example Infrasound Sources

On-going research into infrasound signal monitoring and processing is being pioneered in large part by an international consortium of scientists and researchers who operate, maintain and extend a world-wide seismic and infrasound sensor array network that makes up the International Monitoring System (IMS). The IMS includes a planned 60-sensor network with the primary charter of verifying the Comprehensive Nuclear Test Ban Treaty (CNTBT), a multi-national agreement by cosigned nations to refrain from unmonitored nuclear weapons testing. The

distribution of monitoring stations around the globe has the objective of reliably detecting a detonation of at least 1-kiloton yield anywhere in the world with two-sensors (Two sensors are needed to determine the location of the detonation). Poor signal quality and/or low SNR makes detection and location difficult or impossible given the desired reliability and uncertainties involved. Green (2005) has shown that the current 59-station IMS network can achieve the desired 95% confidence level for detection probability. The seismic and infrasound sensors making up the IMS network enable a continuous, global monitoring capability that also provides a rich data source for natural and man-made event detection and monitoring. The diverse nature and quality of these signals presents processing challenges to the signal analyst.

## 1.3 Sensor/Array-Based Noise Reduction Methods

In order to maximize the signal-to-noise ratio of collected sensor or array data at a particular infrasound or seismic station, the very location must be selected with care. A site is typically chosen based on isolation from man-made sources of infrasound and seismic radiation such as population centers, highways, industrial zones and windfarms. In addition to man-made noise sources, the station location should seek to minimize interference from natural noise sources such as wind and coastal tidal activity. A preferred site topography is a heavily populated forest region where the

station would be naturally shielded from surface wind activity [Christie, 2010]. Locating a station in such an area is not always possible and some stations are highly susceptible to wind noise as a consequence. Wind noise mitigation has traditionally been focused on specific site and sensor configuration strategies. The oldest and most common wind mitigation technique is the use of noise-reducing hose arrays connected to the sensor (see Figure 1-5 below). This technique relies on spatial averaging across numerous porous hoses attached to the sensor to reduce the noise. An assumption in the design of the infrasound array (as well as the signal processing) is that the sound-pressure waves incident on the array are effectively along a planar wavefront. This is due to the regional or even global propagation distances involved in infrasound monitoring. Since the signal is assumed to be coherent over the spatial extent of the sensor array, it is summed coherently, while the noise sums incoherently This assumption is the basis for most of the infrasound signal processing metrics such as cross-correlation, back-azimuth projection, and phase velocity [Bedard, 2005].

The cross-correlation is a measure of the phase across the sensor aperture. The back-azimuth is a projection along the compass direction of the angle from which the source signal originated. The phase velocity and the back-azimuth combine to form the "slowness vector." In general, adding additional sensor sites to the array network will improve the signal to noise ratio but the coherency of a signal across additional stations is more difficult to maintain.

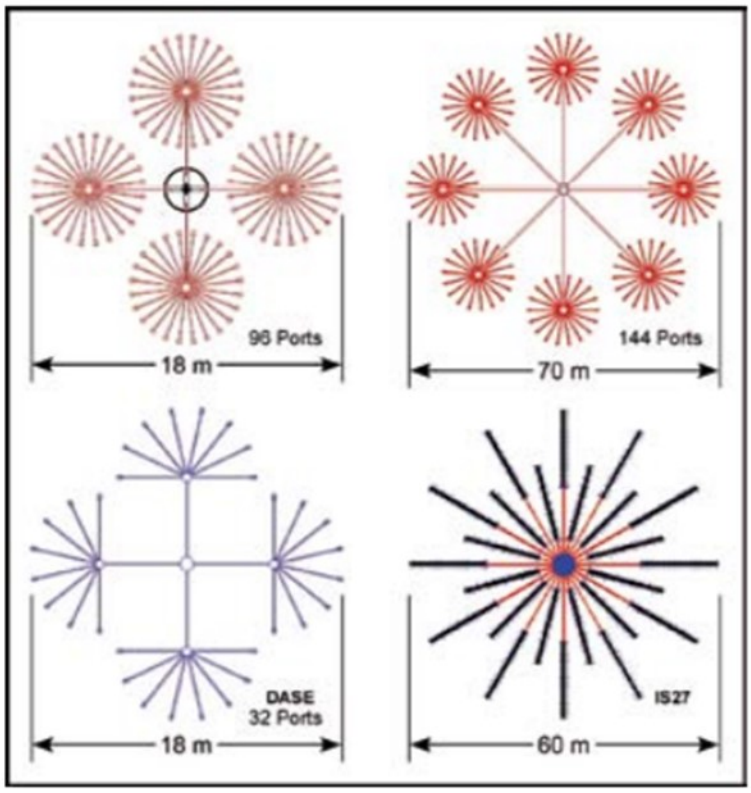


Figure 1-5 Infrasound Sensor Noise Reduction Topologies [Christie]

The array topologies with fewer hoses are typically used at sites with lower ambient infrasound noise. Conversely, the larger, higher density sensor geometries are used in locations where the noise is higher and a SNR improvement of the output data is desired. When the received signal is being coherently summed across an array, the number of hoses is proportional to the sensor output signal-to-noise ratio as given by:

$$\Delta SNR \sim \sqrt{\#\ of\ inlets}$$

It is generally believed that the spatial filtering benefits of the multi-pipe sensor geometries have reached practical limits [Christie, 2010]. In an effort to identify improvements in the SNR of test stations, an alternative to the hose geometry has been developed and investigated. Structures called wind barriers are erected around the sensor to shield it from the incident wind noise (see Figure 1-6 below). Since infrasound noise scales with wind speed, reducing the velocity and turbulence of the wind around the sensor (inside the wind barrier) improves the SNR of the detected signals of interest. In this situation, the wind barriers are typically designed with a 50% coverage ratio, with blockage on the horizontal axis (parallel to the ground). Further isolation from the wind can be achieved by adding a mesh to the surface of the wind barrier. Improvements of up to 90% over the ambient noise baseline have been reported [Hedin, 2003].

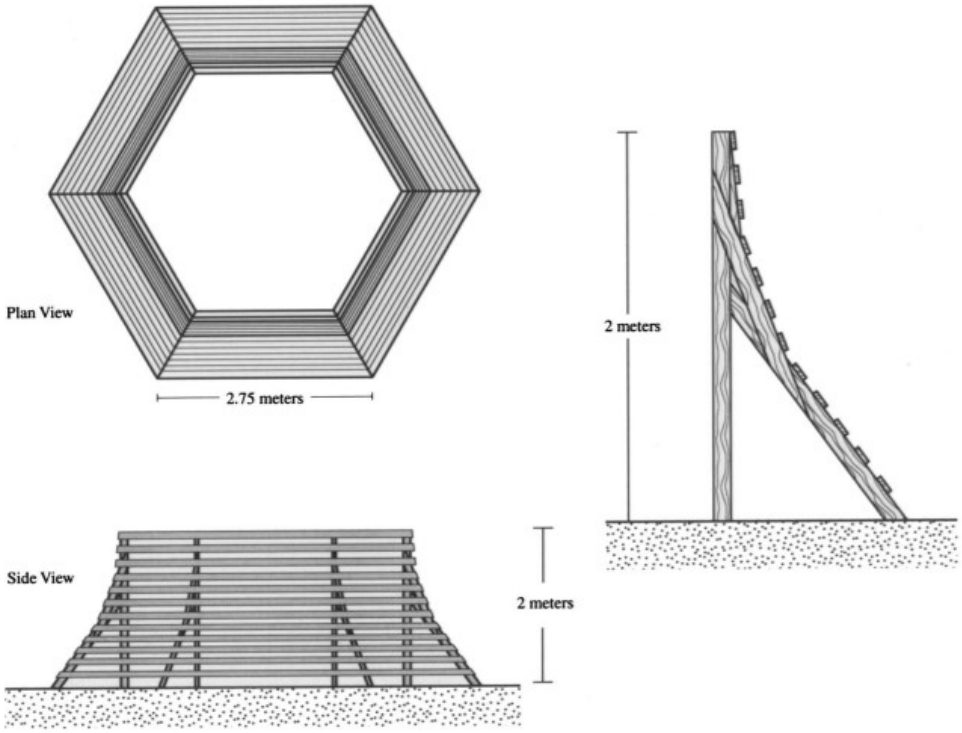


Figure 1-6 Infrasound Wind-noise Reduction Using Spatial Filters [Hedlin, 2005]

## 1.4 Infrasound Signal Processing Methods

The infrasound signal data processing flow begins with detection/location and classification. For example, a remotely deployed sensor operating in a passive "listening" mode may detect that an infrasound signal has occurred. The signal, represented by the response of the sensor versus time, is recorded and stored locally by the sensor's data acquisition (DAQ) sub-system. The location estimator algorithm may use a method such as back azimuth projection to determine a general direction of origin and distance to the source that may be hundreds of miles over the horizon. Next, the task is to determine what caused the received sound. Here the goal is to classify the source as being perhaps a natural event (such as a volcano), or possibly an aircraft or watercraft. Then we want to further specify the source by identifying the type of aircraft (e.g. fixed wing, rotary wing, drone, jet) or the type of watercraft. Afterwards, with even more precise analysis we desire to know information about the attitude or aspect of the source (characterization). Is the detected aircraft taking off or landing? Is the detected ship approaching or moving away? Finally, all of this information must be transferred to the users in the dissemination step. The means and speed with which this is done can vary based on the particular application. Near real-time processing could facilitate the rapid transfer of critical intelligence to

battlefield commanders. Or, in a more mundane application the data could be transferred from the sensor station via the internet to a centralized server for post-processing at a later time. The data flow diagram for a typical infrasound signal processing system is shown below in Figure 1-7.

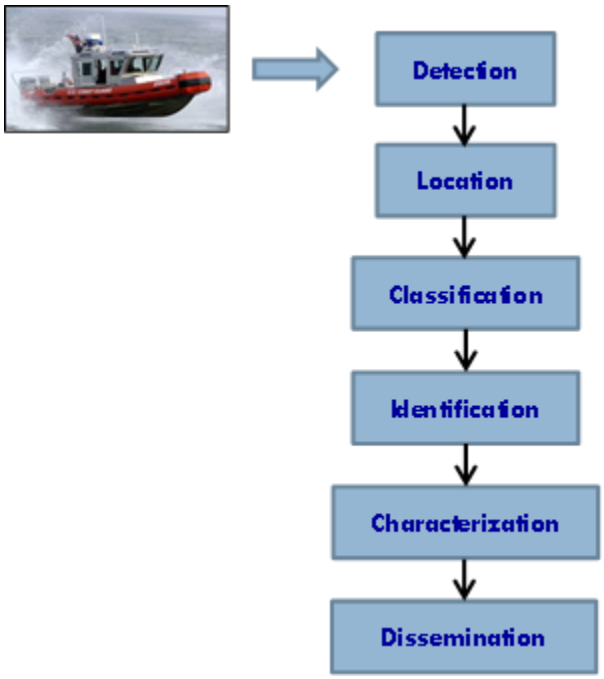


Figure 1-7 Infrasound Signal Processing Flow

## 1.5 Research Purpose and Problem Statement

This research aims to investigate specific signal processing challenges faced by the infrasound and seismic communities, but the applied methods are applicable to a

wider base of practitioners. Wind generated noise caused by microbaroms at the sensor array are typically dealt with via spatially filtering hose arrays. This solution is not always practical given the physical and spatial constraints of the array site. A means to deal with wind noise in a “pre-processing” filter stage could mean the difference between a dataset with exploitable signal(s) of interest or an unusable data set.

To address these objectives a software tool called the MIDAS filter was developed. The Multi-band Isolation of spectra with Data-adaptive Sub-banding filter employs user-defined spectral weighting with tailorable input parameters to isolate signals of interest from a variety of background clutter including uncorrelated or channel-correlated noise, undesired harmonics of the source signal and unwanted stray signals.

# 2 Related Work/Literature Review

This research, (and this dissertation in general), made use of two infrasound-based software tools developed independent of, and in no way connected with this research. First, this research used the InfraMonitor software tool developed primarily by Steven Arrowsmith while at Los Alamos National Laboratories. This tool was originally developed based on work published in the 2008-2012 timeframe. The software is essentially unmaintained, but continues to see use in the signal processing community, especially for infrasound analysis (see Table 2-1 below). This tool was used as a benchmark to evaluate the various test signals for their detection and coherence coefficient results after filtering by band-pass, Pure-State and MIDAS methods.

Table 2-1 Software Test Parameters Used with InfraMonitor Software [Arrowsmith, 2012]

| Parameter | Significance |
|---|---|
| Correlation coefficient, a measure of S/N | Index of signal quality and a measure of confidence in the accuracy of other parameters |
| Azimuth | Critical measure of the direction from which sound is originating |
| Phase speed (indicating the elevation angle) | Angle of arrival can indicate the location of source regions aloft |
| Spectral content | The dominant frequency (frequencies) can indicate important characteristics of the sources |
| Sound pressure level | The amplitude, although a measure of source strength, is greatly affected by propagation |
| Duration | Typical vortex-related signals continue for tens of minutes or more. Signals of very short durations (e.g., ~1 min) are unlikely to be related to a coherent vortex. |
| Persistence | Even at low S/Ns, confidence can be obtained in the characterization of signal sources if they persist for significant periods of time. Histograms of parameters over interval can quantify distributions and, e.g., identify source direction even for weak signals |

The second software tool that this research leveraged was the Pure-State filter. This algorithm was originally developed by John V. Olsen at the University of Fairbanks and was first patented in 2011. The Pure State filter is also used in the infrasound

processing community so it provides a relevant, comparative tool when evaluating the MIDAS filter capability when processing infrasound signals.

With the requisite operation and maintenance in support of the Comprehensive Nuclear Test Ban Treaty (CTBT), the International Monitoring System (IMS) provides a rich source of infrasound and seismic data for analysis of signals of interest and on-going development of sensor and network technology. The detection capability and location accuracy of current network stations and sensors can be greatly improved. A primary error source for most sensors is wind noise due to turbulence at the sensor as a result of the local geography. Park (2005) points out that much of this error can be attributed to the 6-8 second period of microbarom signals and a 1-50 Hz bandpass filter preprocessing step could sufficiently reduce the noise due to wind for some applications. However, there are many situations where this simple approach is not sufficient, such as when the signal of interest is below the 1Hz cut-off of the bandpass filter (such as a volcano). Most sites make use of wind noise-reduction by way of pipe arrays that sum the incident energy at the microbarometer sensor. [Christie], [Hale]. This spatial averaging technique has not changed appreciably since 1959 and is thought to have reached its practical limits in terms of array size and port configurations. As a result, a new approach to wind-noise reduction is needed [Christie]. Green (2010) characterized detection errors and noise

contribution from sources such as atmospheric turbulence and parametric site models. With the objective of determining the detection probability rate of the worldwide infrasound monitoring network, he concluded that several factors influence the networks overall performance capability including how the infrasound energy propagates from the source to the receiver, the noise characteristics of the receiver and the ability to correctly detect the signal.

In addition to the detection capability identified above, source location (or localization) is also a critical aspect of infrasound sensor network and signal processing capability. Many source location methods are based on the association arrival data from a group of several arrays which are individually processed for Direction-of Arrival (DOA). The localization provided by increased numbers of arrays can reduce the error of the location estimate. Errors using this method can be attributed to atmospheric effects such as wind and thermal variations as well as unique channel noise errors at any of the individual array sensors. Localization uncertainties on the order of 100m can be achieved using back-azimuth methods. In other methods, the individual arrays are summed together to create synthetic arrays having larger effective apertures. The confidence factors for localization estimates using the synthetic aperture methods have been shown to be an order of magnitude higher than those of back-azimuth methods where sensor arrays are processed individually [Szuberla, et.al].

# 3 Theoretical/Analytical Background

## 3.1 Validation Case #1: Extraction of Signals of Interest from Low SNR Data Sets

The objective of any signal processing filter is to remove unwanted noise from the input data to maximize the SNR of the subject data set. A measure of the quality of the filter is how well it can achieve this while minimizing any distortion to the data of interest. A more subtle nuance of this performance is the ability of the filter to isolate desired signals that are embedded in low SNR data and successfully extract usable information. To demonstrate and quantify these desired filter performance characteristics for the MIDAS filter, a tailored validation test case was developed. This test case was composed of a composite waveform having multiple, independent sinusoids overlaid onto a baseline signal of simulated "channel noise". The channel noise was made up of normally distributed white noise. The test signal was arbitrarily added to the middle of the "channel noise" data. This structure simulates the composite signal appearing at some point in the sensor data stream, being present for some number of samples and then disappearing. The sensor channel then returned to the ambient "noise" condition. This waveform was run through the MIDAS filter in two different permutations, a high-SNR version and a

low-SNR version. In each case the amplitude coefficients for each of the sinusoids were given a unique weighting function.

Table 3-1 Validation Case #1 Sinusoidal Coefficients

| Validation Case Sinusoid Coefficients | | | |
|---|---|---|---|
| Coefficient | Frequency (Hz) | Low-SNR Waveform | High-SNR Waveform |
| A | 100 | 0.2 | 1.0 |
| B | 125 | 0.15 | 0.75 |
| C | 150 | 0.25 | 0.55 |
| D | 175 | 0.10 | 0.60 |
| E | 200 | 0.35 | 0.85 |
| F | 225 | 0.30 | 0.80 |

The general form of the test waveform was given by:

$$y(t) = Acos(2\pi f_1 t) + Bsin(2\pi f_2 t) + Ccos(2\pi f_3 t) + \cdots$$

$$\ldots + Dsin(2\pi f_4 t) + Ecos(2\pi f_5 t) + Fsin(2\pi f_6 t) + e(t)$$

where $e(t)$ represents the normal, or Guassian-distributed noise added to the waveform.

The experiment included 4 simulated channels with a 500 sample/second sampling rate collected for 1 hour. This generated a total record length of 1,800,000 points. The simulated Channel #1 response is shown below in Figure 3-1. In this case, the time-history of the high-SNR waveform is shown. Here, one can readily observe the desired waveform that was inserted into the middle of the test signal. In this example, the test waveform was inserted at the mid-point of the 1-hour collection window. The test waveform inserted into the middle of the record had a signal duration of 3 minutes.

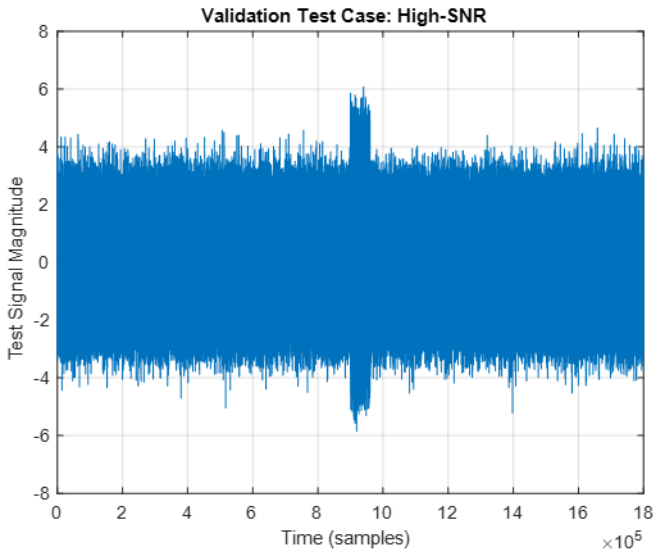


Figure 3-1 Validation Test Case #1 – High SNR Waveform

In Figure 3-2 below, the time-history of the low-SNR version of the test waveform is shown. This waveform is based on the same 1,800,000 record as the previous plot. The 3-minute test waveform was inserted into the center of this record as before. However, in this case, the "low-SNR" waveform coefficients from Table 3-1 above were used to weight the test waveform. In contrast to the high-SNR version seen previously, the test waveform is buried in the simulated channel noise and is therefore not readily visible in the plot.

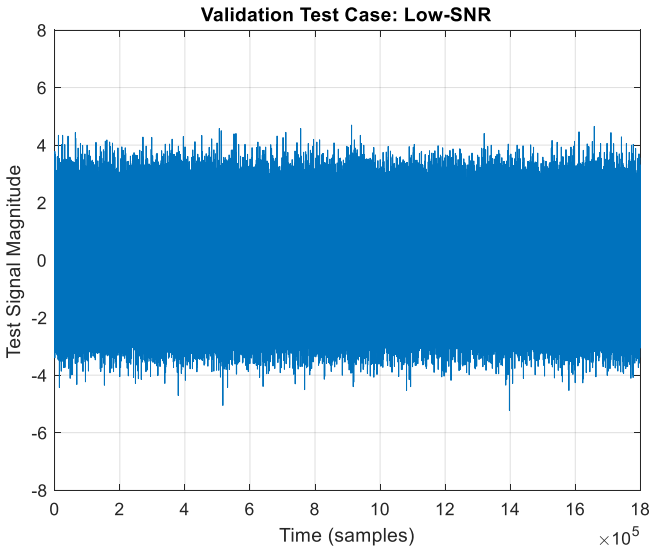


Figure 3-2 Validation Test Case #1 – Low SNR Waveform

Figure 3-3 below shows the time history plots for the channel noise and the test waveforms. To help clarify the difference in the waveform record between the test signal and the channel noise, a plot from the record showing each of the unique responses is presented. The test waveform occurs just after the midpoint in the

waveform record and is highlighted in the figure by the green box. The red box highlights a section of the waveform record just prior to the start of the test waveform and this section represents a portion of the channel noise. The difference in the raw magnitude of the data provides a clue regarding the higher amplitude coefficients used with the test waveform for the high-SNR test case and where that information exists in the data stream.

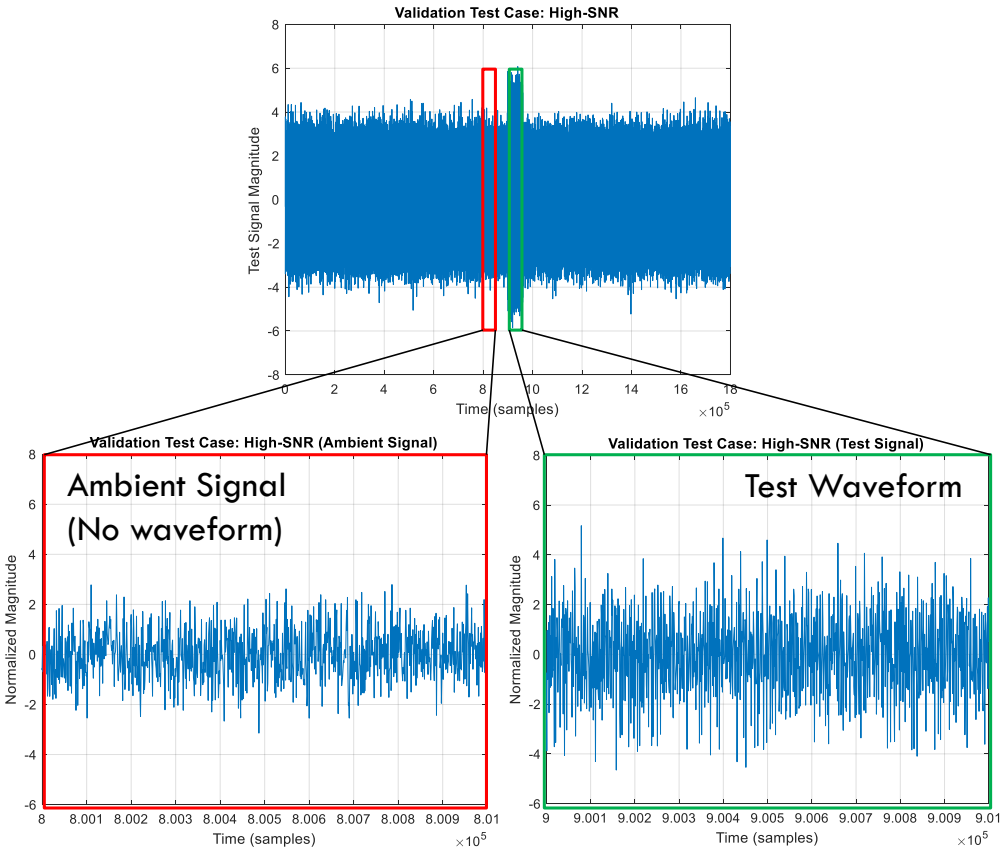


Figure 3-3 Validation Test Case #1 – High SNR Waveform Detail

Figure 3-4 below shows the comparison between the time-history plots for the high and low-SNR waveforms as compared to the corresponding “Detection Maps”. These detection map plots were created by processing the 1,800,000-point record with a sliding window of 1000 point width. Each window was processed using Welch’s [Welch, 1967] estimate for the power spectral density of the encapsulated data elements. The corresponding signal-to-noise ratio of the windowed power spectral density estimate was computed. As a detection scheme, the SNR should increase when the windowed segment aligns with the segment of the waveform record that includes the test sample. For the high-SNR test case, the expectation would be not only to detect the test waveform at the correct location (just beyond the midpoint of the waveform record) but to also see a larger reported SNR than the low-SNR case. In the two lower plots, the SNR of the MIDAS-filtered data is used as an indicator of the success that the filter had in identifying where in the data stream the test waveform occurred (detection) and to what degree the test waveform was isolated from the background channel noise. In this example, the High-SNR test waveform was detected and a SNR of approximately 8dB was achieved. In the Low-SNR case, the test waveform was initially buried in the background noise (SNR=0) but the MIDAS filter was able to detect the test waveform and provide approximately 3dB of SNR.

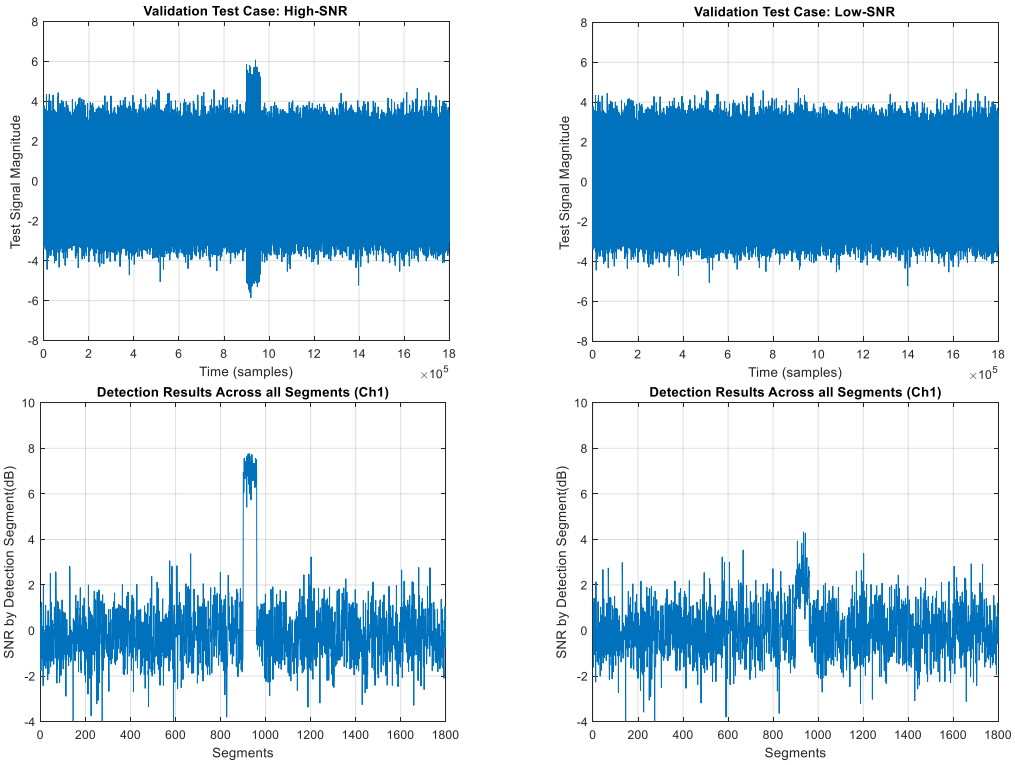


Figure 3-4 Validation Test Case #1 – Waveform Detection Results

In Figure 3-5 below, the waveform record is divided into low, mid and high frequency segments. These correspond to prior-to, during and after the test waveform appeared in the data stream. Each segment is then processed for the corresponding power spectrum. The high-SNR case is plotted on the top of the figure and the low-SNR case is plotted on the bottom. As expected, not only does the MIDAS filter detect the presence of signals of interest at the correct location in the data stream (the mid-point) but the filter also correctly identified the individual

frequencies that made up the composite test waveform. Refer back to Table 3-1, to confirm the 100, 125, 150, 175, 200 & 225 Hz tones that were used.

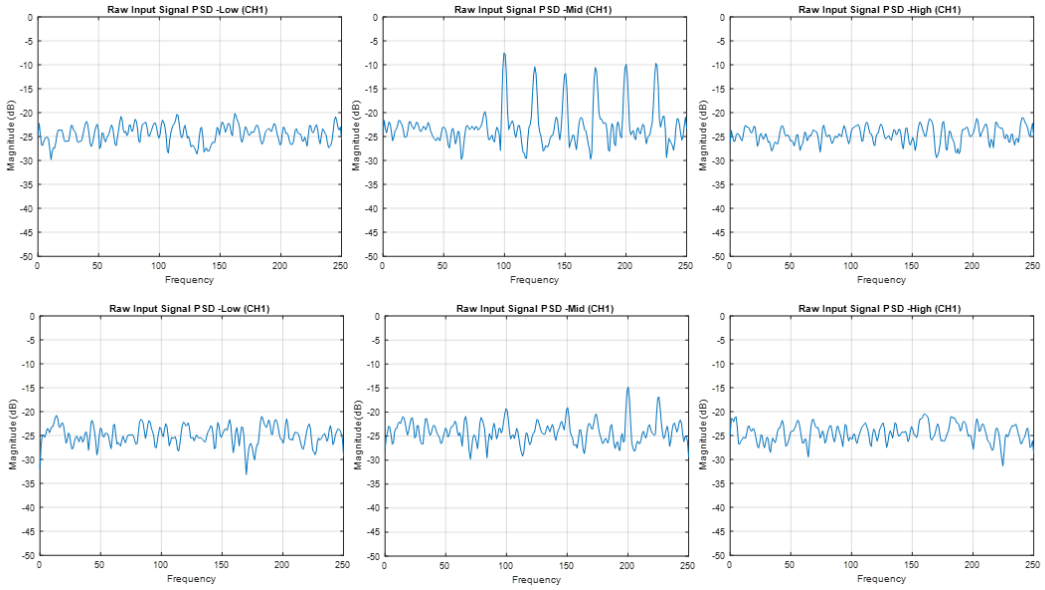


Figure 3-5 Validation Test Case #1 – MIDAS filtered Output for Test Waveform

## 3.2 Validation Case #2: Variable/Selectable Filter Bandwidth

Another important feature of the MIDAS filter is its ability to support user-selectable filter bandwidths. This gives the signal analyst the ability to isolate one or more frequencies within the available spectrum and apply in-band or out-of-band weighting to each frequency. In doing so, individual, or groups of tones can be isolated, and unlike band-pass filters, the MIDAS filter can exclude one or more

frequencies from among a group of desired frequencies (e.g., drop one undesired frequency from the middle of an already selected passband). To demonstrate this capability a test data set is presented that consists of a single guitar note which was struck, and then recorded for 4 seconds as it resonated. The particular note played was resonant at 440Hz. The 440Hz note (play an ”A” note on the 5$^{th}$ fret above middle “C”) is a standard tuning note used by musicians and is referred to as the “concert pitch.” To simulate additive channel noise, the guitar data was augmented with gaussian white noise with variance=0.1 and mean=0. Figure 3-6 below shows the noiseless time domain response of the guitar data in the top panel, the frequency domain response in the center panel and the spectrogram in the bottom panel. The power spectrum plot is used to show the magnitude of the spectral content within a signal, while the spectrogram is used to show when each frequency is present within the signal. In this example, the spectrogram clearly shows the natural tendency of the higher-order harmonics to fade out over time.

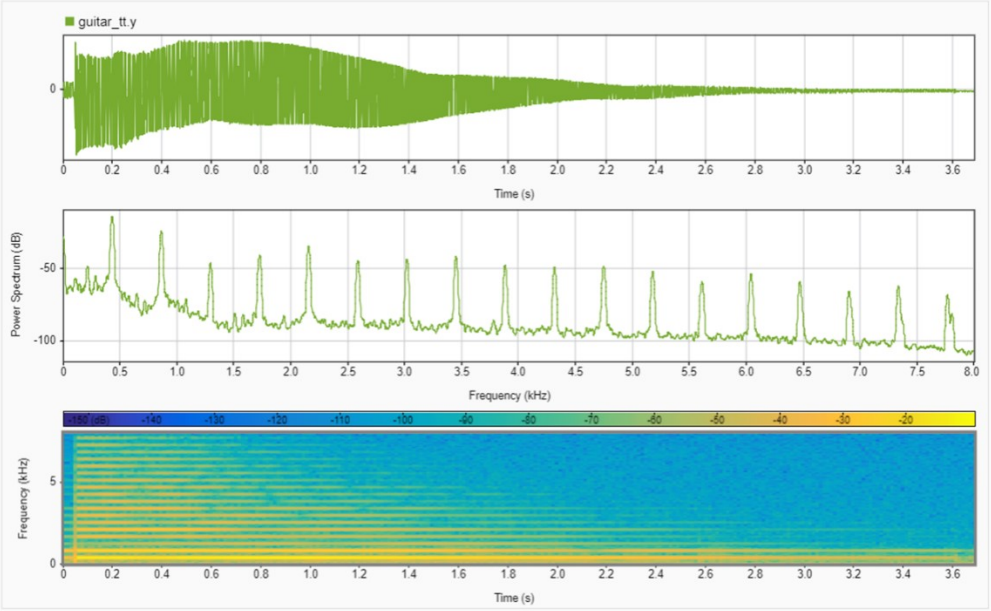


Figure 3-6 Validation Test Case #2 – Time Domain (top), Frequency Domain (middle) and Spectrogram (bottom) Responses for Guitar Note at 440 Hz

The power spectrum plot from the central panel in Figure 3-6 above shows the frequency response of the guitar when the "A" note is played. Table 3-2 lists the frequencies of the first 10 harmonics for the fundamental 440Hz tone.

Table 3-2 Partial Frequency “Map” of the Guitar “A” Note

| Guitar "A" Note | |
|---|---|
| | **Frequency** |
| Fundamental | 440 Hz |
| 1st Harmonic | 880 Hz |
| 2nd Harmonic | 1320 Hz |
| 3rd Harmonic | 1760 Hz |
| 4th Harmonic | 2200 Hz |
| 5th Harmonic | 2640 Hz |
| 6th Harmonic | 3080 Hz |
| 7th Harmonic | 3520 Hz |
| 8th Harmonic | 3960 Hz |
| 9th Harmonic | 4400 Hz |
| 10th Harmonic | 4840 Hz |

Figure 3-7 below shows the raw guitar data with the additive noise applied (left) as well as the MIDAS filtered output data with noise reduced (right).

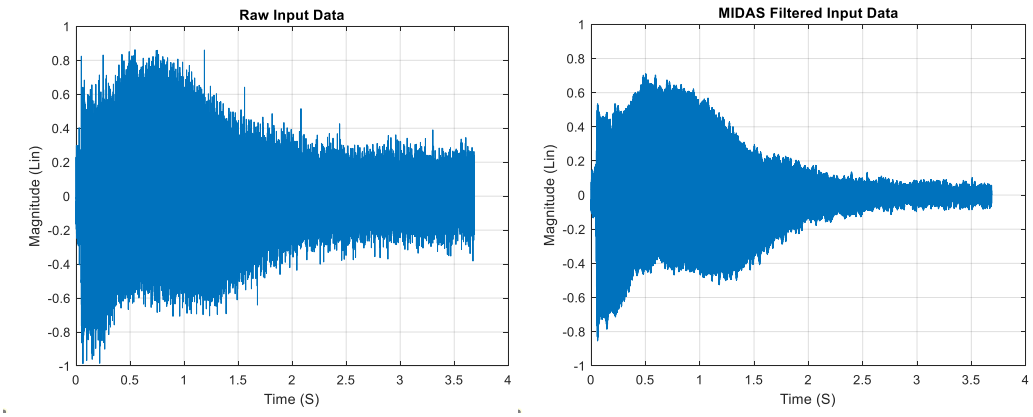


Figure 3-7 Validation Case #2 – MIDAS Filtered Guitar Tone

Figure 3-8 below shows the frequency domain plot for the guitar data with 10dB of out-of-band attenuation applied. In this example, the filter bandwidth was 400Hz and the in-band noise can be seen adjacent to each of the 3 dominant frequencies (440Hz, 880Hz & 2200Hz). The inset plot in Figure 3-8 below shows the Power Spectral Density plot for the guitar data and indicates the 3 dominant frequencies (440Hz, 880Hz & 2200Hz) selected by the filter (shown in blue and red) as well as the extent of the filter bandwidth in frequency space.

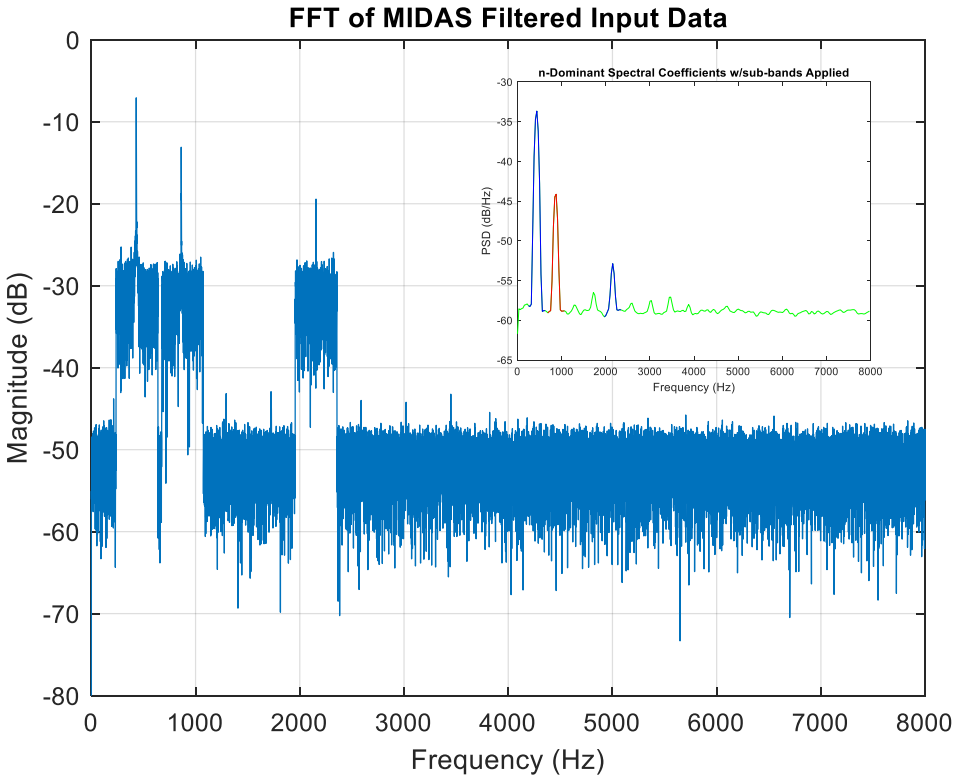


Figure 3-8 Validation Case #2- Guitar Spectrum Showing Resonant Frequency Behavior and MIDAS Filter Sub-banding

Similar to what was presented above, Figure 3-9 below shows the frequency domain plot for the guitar data with 10dB of out-of-band attenuation applied. This example also shows each of the 3 dominant frequencies (440Hz, 880Hz & 2200Hz), however, in this case the adjacent in-band noise is significantly reduced, as the chosen filter bandwidth was reduced to 40Hz. The inset plot in Figure 3-9 below shows the Power Spectral Density plot for the guitar data and indicates the 3 dominant frequencies (440Hz, 880Hz & 2200Hz) selected by the filter (shown in blue and red) as well as the extent of the filter bandwidth in frequency space.

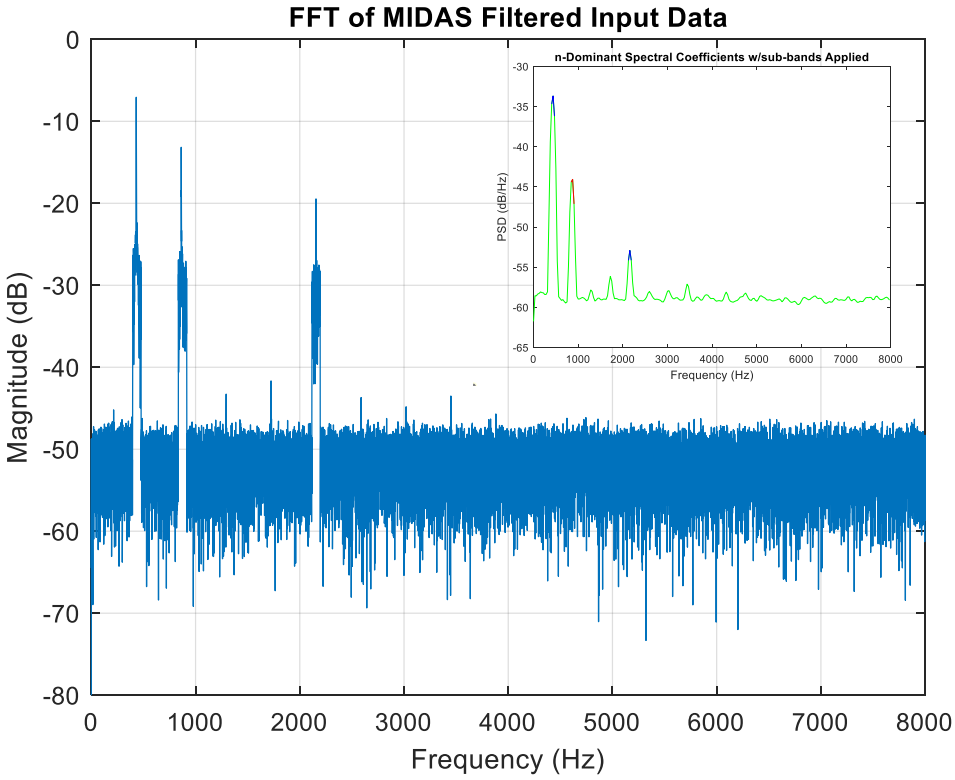


Figure 3-9 Validation Test Case #2 – Guitar Spectrum for a Single 440Hz Note After Processing with MIDAS Filter (Selected Frequencies Isolated)

In Figure 3-8 and Figure 3-9 above, 3 frequencies of interest were selected for retention during the filter operation. However, several other harmonics are also evident in the spectral plot. A comparison of the spikes seen in the spectral plots with the data in Table 3-2 confirms the presence of harmonics 2,3,5,6,7 & 8. In this example, since these frequencies were not selected for retention, the 10dB attenuation factor was applied. In addition to the 440Hz, 880Hz & 2200Hz selected above Figure 3-10 below shows the same 440Hz guitar tone as before, however in

this case the data has been prefiltered with a 500Hz low-pass filter. In this example, the higher frequencies and the higher-order harmonics have been removed leaving only a few of the lower frequencies including the fundamental 440Hz tone. In practice, this operation would severely change the "richness" of the guitar note and would not normally be desired. However, for the sake of this demonstration we have assumed that the analyst desired to separate out some of the higher-order data and isolate signal content near the 440Hz fundamental tone.

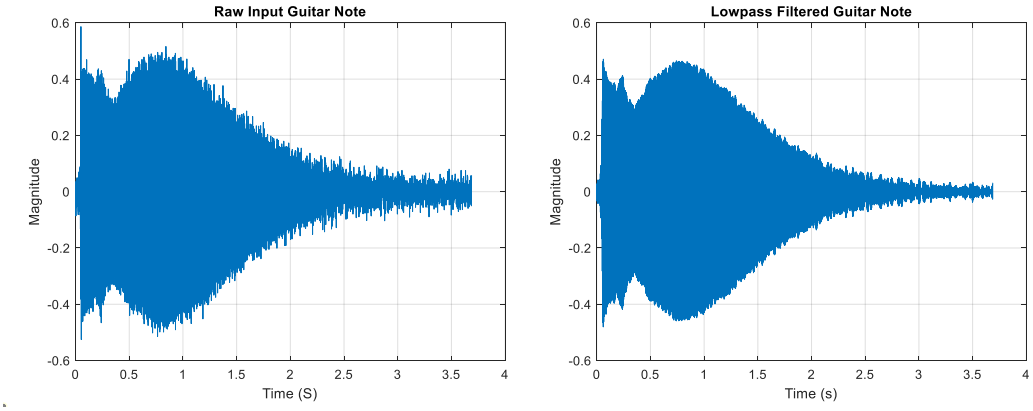


Figure 3-10 Validation Test Case #2 – Time Domain Plot of Raw and Bandpass-filtered Guitar Data for a 440Hz Note

In this example the low-pass filter has removed a noticeable amount of the additive noise from the data. Initially this appears to be a quite good result, however the improvement came at the expense of the quality of the signal. While the signal appears to be markedly improved by 500Hz low-pass filtering, the removal of all of the signal content above 500Hz has changed the sound of the remaining tones and

the composite signal. It may not be obvious upon visual inspection of the time history, however, listening to each signal clearly identifies the difference between the original signal and the low-pass filtered signal.

# 4 Description of Research Method

## 4.1 The Applied MIDAS Filter

From a functional perspective, the MIDAS filter follows a 9-step algorithm. In many of the steps the signal analyst is able to tailor the performance of the filter by modifying input parameters. In practice, the filter is designed to be used in an iterative manner, with the initial (default) analysis parameters intended to provide a "first-pass" evaluation for the analyst to review. Depending on the particular objectives of the analysis and/or the nuances of the data set, the filter parameters can be modified and the data processed again to investigate alternative results. In this way, the analyst can tease out particular aspects of the signals of interest, or evaluate one portion of the data bandwidth and then evaluate another.

## 4.2 Detailed Review of the MIDAS Algorithm

1) In the first step of the algorithm, the raw input data is transformed via an FFT operation from the time domain to the frequency domain.
2) In the second step of the algorithm the frequency data is passed through a wavelet denoising step. This step makes use of block thresholding (James-Stein) which looks to find optimal local and global thresholding parameters.

3) Next, compute the power spectrum of the wavelet-filtered input data. This pre-filtering step provides a broad-band, general reduction in the noise of the input data set. The typically modest improvement in the signal-to-noise ratio (SNR) of the Fourier transformed data set results from the reduction of broadband channel, station or processing noise that are generally not of interest to the analyst. The improved SNR of the transformed data also helps to identify the dominant frequencies within the input spectrum.

4) Next, the power spectral density (PSD) is computed. The MIDAS algorithm uses Welch's definition of the PSD plot [Welch, 1967]. Improved estimation of the power spectrum is achieved when the spectrum is segmented and those segments are averaged. These segments are further modified through the application of a windowing function, such as a Bartlett or Hamming window [Oppenheim, 2010]. The need for a windowing function is a consequence of the use of the Discrete Fourier Transform. In addition to providing the windowing function, Welch's method provides for an overlap of segments which reduces the tapering at the edges of the segment that is typically caused by the windowing function. A key benefit of the PSD function at this stage of the MIDAS algorithm is the "mapping" of the input data set to a reduced sample data set produced by the PSD processing. Surveying the reduced sample size PSD plot allows the analyst to more clearly see the dominant spectral content within the data set.

5) Next the analyst may use the MIDAS graphical user interface (GUI) tool to identify the spectral components that are desired, while simultaneously identifying those that will be filtered. In this case, each selected frequency point is represented on the PSD plot by a red asterisk. The initial PSD plot is generated based on the default MIDAS parameters which can be tailored by the analyst. A "Prominence" variable determines the initial frequencies that are identified by the analyst as being "dominant" in the data set. In this context, dominant is defined as one frequency having a peak power level greater than its neighbors by the value of the prominence variable. Each frequency identified/selected during this step is presented in tabular form in the left panel of the GUI. The analyst can select individual frequencies from the table and press the "Delete Row" button to remove them from the PSD plot. This removes the frequency entry from the table as well as the associated red asterisk in the PSD plot. The analyst may also add a frequency to the table by pressing the "Add Row" button and then clicking anywhere on the signal trace in the PSD window. The tool will automatically "fix" to the nearest actual data point. A "Precision" variable determines how close the user needs to be to the true value in the data file. A new row will be added to the table with the associated magnitude and frequency values. This action will also add a red asterisk to the PSD plot at the selected point.
6) Surrounding each frequency point selected in the PSD plot is a frequency sub-band. This sub-band is represented by the "Sub-bandwidth" variable and

is represented by the red lines in the trace. The sub-band represents how many adjacent frequencies the analyst wants to include in the filter once a desired frequency has been selected. Varying this parameter allows the user to select very narrow target bandwidths when the input data supports it, or conversely, a wider setting allows for the inclusion of adjacent points in the event the input data is not extremely spectrally pure.

7) Now that the desired frequency content from the data set has been identified, the selected points from the PSD data set are mapped back into the full-size raw dataset. Here, the associated data points and sub-bands are identified.
8) Next the full-size raw data set is weighted by either the selected sub-band mask or the rejection weight. The "in-band attenuation" variable is applied to all raw data points within the sub-band mask (ie: frequency points that the user selected to pass-thru the filter). The "out-of-band attenuation" variable is applied to all raw data points outside of the sub-band mask (ie: frequency points that the user wants to filter out or attenuate down).
9) Finally, the MIDAS filtered data set is inverse Fourier Transformed back to the time domain for plotting and comparison to the raw input time series.

The MIDAS filter is intended to be used by the signal processing analyst in an iterative manner in which the default system variables only provide an initial, "suggested" output. The analyst must review this initial result and make informed adjustments to the system variables to improve the MIDAS filter results for the given

input data set. The ability of the MIDAS filter to support this iterative process allows the analyst to fully investigate various aspects of the input data. Figure 4-1 below shows the detailed flow diagram of the MIDAS algorithm.

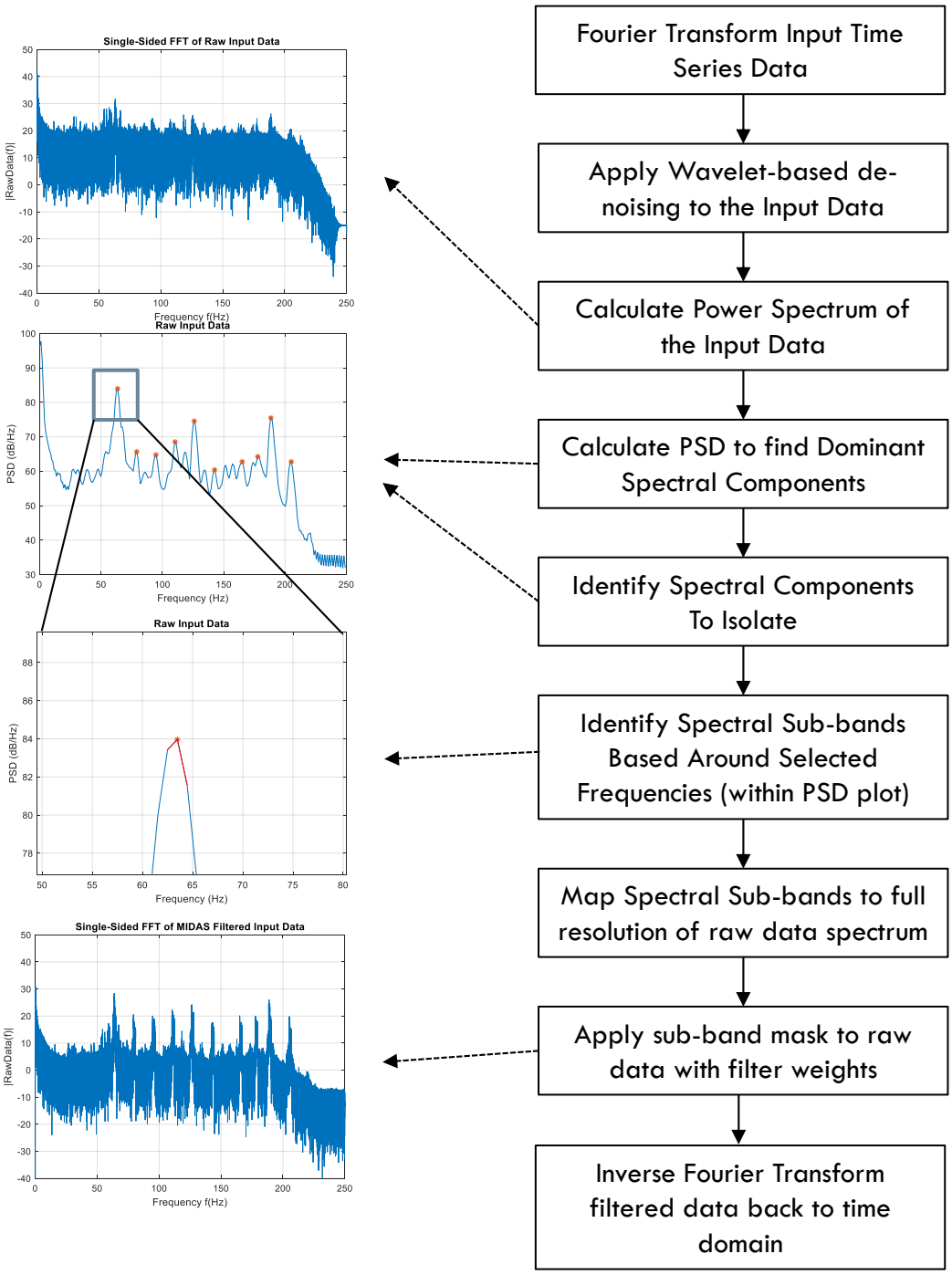


Figure 4-1 MIDAS Filter Detailed Algorithm

The MIDAS filter algorithm has been incorporated into a convenient user interface using the MATLAB [Mathworks] software tool. A graphical user interface (GUI) is used to manage the execution of the MIDAS software algorithm. Figure 4-2 below shows the initial GUI which uses default parameters to provide an initial pass through the algorithm and produce an initial filter result for the input data. The user can review these results, make adjustments to the analysis parameters and re-run the analysis to produce an alternative result. The left-most panel of the GUI includes the user-editable fields for the default parameters.

- Peak Prominence – Adjusts the amount by which spectral peaks must exceed their neighbors to be selected for inclusion by the MIDAS algorithm.
- % Sub-bandwidth – Adjusts the width of the inclusion bands that are applied around each elected frequency point. All frequencies within the sub-band width will be included in the application of the "in-band" spectral weighting function
- In-band Attenuation – Select the level of attenuation applied to all frequency content included within the selected sub-band width
- Out-of-band Attenuation – select the level of attenuation applied to all frequency content not included within the selected sub-band width

The left panel also includes a “Refresh” button which can be used to update the display to ensure that no stale data exists in any plot within the display. The final, and most important button on the left panel of the GUI is the “Select Frequencies” button. This button is used to bring up the detailed filter configuration GUI. When selected, a secondary screen will appear where additional actions are required before returning to the main GUI.

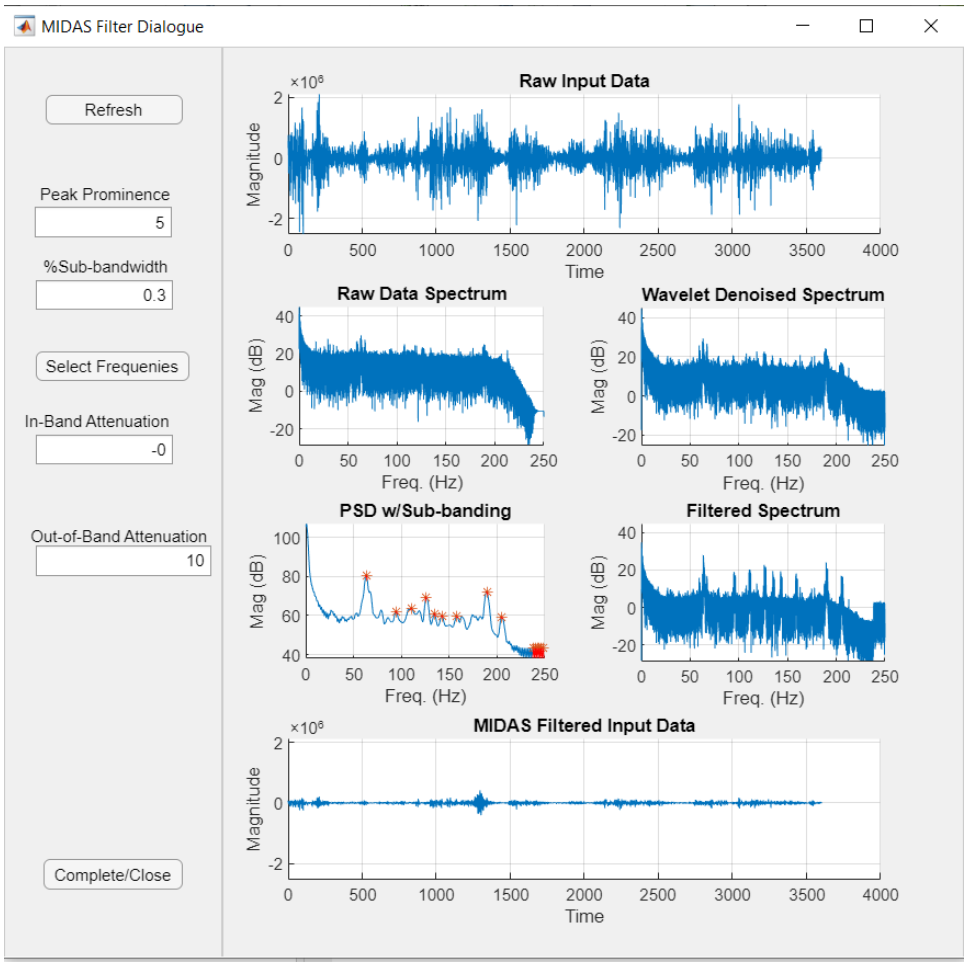


Figure 4-2 MIDAS Filter Processing GUI Example (Page 1)

The right side of the GUI includes a 5-panel display showing the currently active data set. The top plot shows the time domain response of the raw input data file with no processing applied. This provides a visual reference point for the user. The second row of the display includes two plots in a side-by-side configuration. The left-hand plot shows the frequency domain response of the raw data input file. The right-hand plot shows the frequency response of the raw data after it has been processed with the Wavelet de-noising pre-processor. Refer to Step 2 in Section 4.2 above for a description of this operation. The third row of the display also includes two plots in a side-by-side configuration. The left-hand plot shows the power spectral density (PSD) plot with the sub-banding and default frequency selections identified by asterisks. This plot is a miniature version of the "main" plot from the detailed filter configuration GUI that comes up when the user presses the "Select Frequencies" button. The right-hand plot on this row is the filtered spectrum plot for the raw input data based on the configuration/selections from the left-hand plot. The frequencies and sub-bands selected in the left-hand plot (actually in the detailed filter configuration GUI) are mapped back onto the raw data set where the spectral weight mask is applied and the resultant spectrum is computed. The final (bottom) row on the main GUI is the time domain plot for the MIDAS filtered raw data. This plot is the inverse Fourier transform of the spectrum shown in the right-hand plot of row 4. A comparison between the top and bottom plots of this GUI provides an indication of the improvement the MIDAS filter was able to apply to the current data set.

Figure 4-3 below shows the second GUI of the MIDAS tool, called the Detailed Filter Configuration GUI. This window allows the user to see a detailed view of the spectrum of the test data and make real-time changes to the response. By selecting or de-selecting the various frequency elements of the spectrum, the weighting function is modified and the overall spectral response is updated.

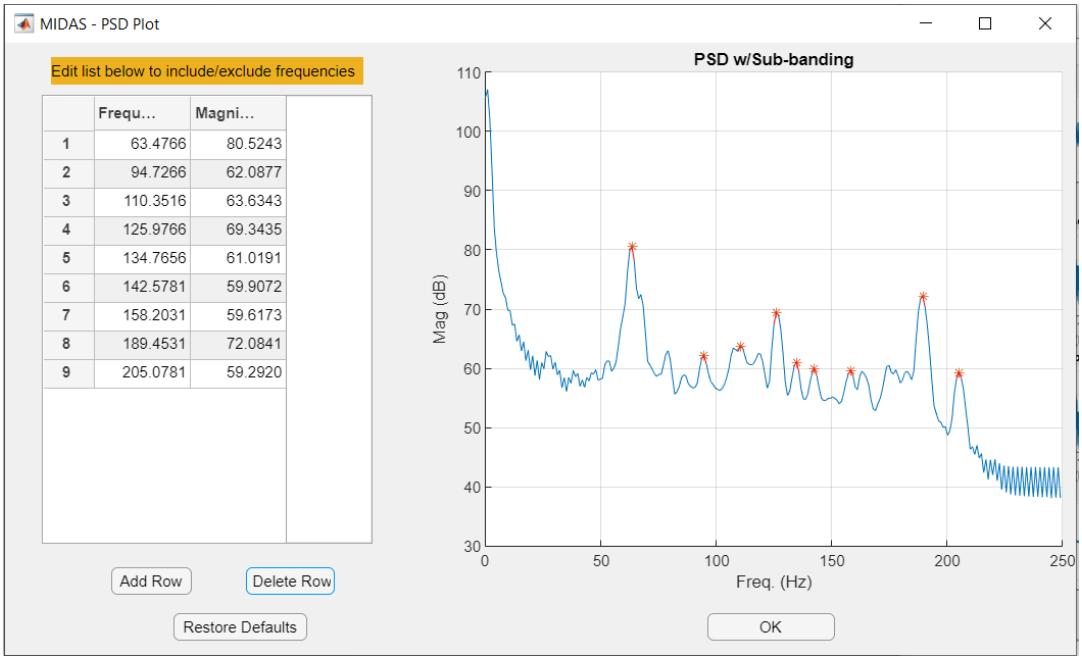


Figure 4-3 MIDAS Filter Processing GUI Example (Page 2)

The left-hand panel includes the frequency list for the current data set. This provides a tabular listing of each frequency that is currently selected and its associated magnitude. Every frequency value represented in the table also appears as a red asterisk on the PSD plot in the right-hand window. The defaults used by the MIDAS

filter mean that upon initialization of this GUI, there will be a small number off frequencies already pre-selected for the user. To delete an unwanted frequency, the user can select a row in the table and then press the “Delete Row” button. The row in the table will be cleared out and the corresponding red asterisk on the right-hand PSD plot will be removed. Alternatively, the user may select the asterisk on the right-hand plot using the mouse and then press the “Delete Row” button. To add a new frequency point to the table, the user presses the “Add Row’’ button. This will cause a new, blank row to appear at the bottom of the table and also activate the mouse-based input cursor. The user may now select a desired frequency point on the PSD plot. The user need not select exactly the point they want. As long as they are reasonably close, the MIDAS filter will “snap” to the nearest actual data point. (Note: there is a user-defined variable that governs the range of this snap function. ie, how close does the user need to be to an actual data point). When a new row is added, the table will automatically update to sort by frequency. For example, if the user entered a frequency in the center of the currently displayed bandwidth, the data would load into the new entry at the bottom row of the table, but would then automatically sort to its correct location in the middle of the table. There is also a “Restore Defaults” button on the left panel of this GUI. The user may select this button if they have made one or more changes to the data that they do not wish to keep. The user may decide to start over again by going back to the raw data. Restoring the defaults will e-load the raw data and re-apply the default parameter settings. Finally, when the user has completed making updates and wishes to “save” this filter configuration, the “OK”

button may be selected. This action will close the detailed filter configuration GUI and return the user to the main GUI. The filter parameters are passed to the main GUI and the displayed data is updated. Specifically, the plots on row 4 will be updated to reflect the changes in the filter parameters. By extension, the final plot on row 5 will also be updated since it is derived from those of row 4. At this point the MIDAS filtering operation is complete and the user can pass the output data to an external application. Since the MIDAS filter is iterative in nature, the process can be run again to adjust the output further.

# 5 Experimental Results

## 5.1 Experiment Overview

The MIDAS filter can be applied during the generalized signal processing flow as either a pre-processor (used to reduce the noise content in a signal prior to the application of some type of signal processing methodology) or as the primary filtering stage without the need for subsequent processing prior to executing the desired signal processing. To demonstrate the utility of the MIDAS filter, a standard signal processing application is used as a benchmarking tool. A variety of input signals of interest are applied to the tool and the various output figures of merit are compared to evaluate the efficacy of the MIDAS filter. In this case, the InfraMonitor signal processing tool developed by Los Alamos National Laboratories was selected as the benchmarking software tool. InfraMonitor was selected because it is well known and used among practitioners of seismic and infrasound analysis and it provides a robust set of accepted output metrics that can be used to assess the MIDAS filter.

## 5.2 Pure State Filter Overview

The InfraMonitor tool described above was selected due to its capability as an infrasound and seismic signal processing and analysis tool. The Pure State filter [Olsen, 2009] was also used in this experiment to provide a more direct comparative assessment of filter capability. In this experiment the test data signals were processed with three different types of filters: the band-pass filter, the Pure-State filter and the MIDAS filter. The InfraMonitor tool was then used as a common platform to assess the post-filtered results.

The Pure State filter is a data-adaptive filter that depends on cross-channel coherency to isolate signals of interest from noise sources such as wind, which would generally be expected to demonstrate incoherent behavior at typical infrasound sensor geometries [Olsen, Samson, 1981]. Figure 5-1 below shows the logic flow for the Pure State filter when applied to infrasound signals of interest.

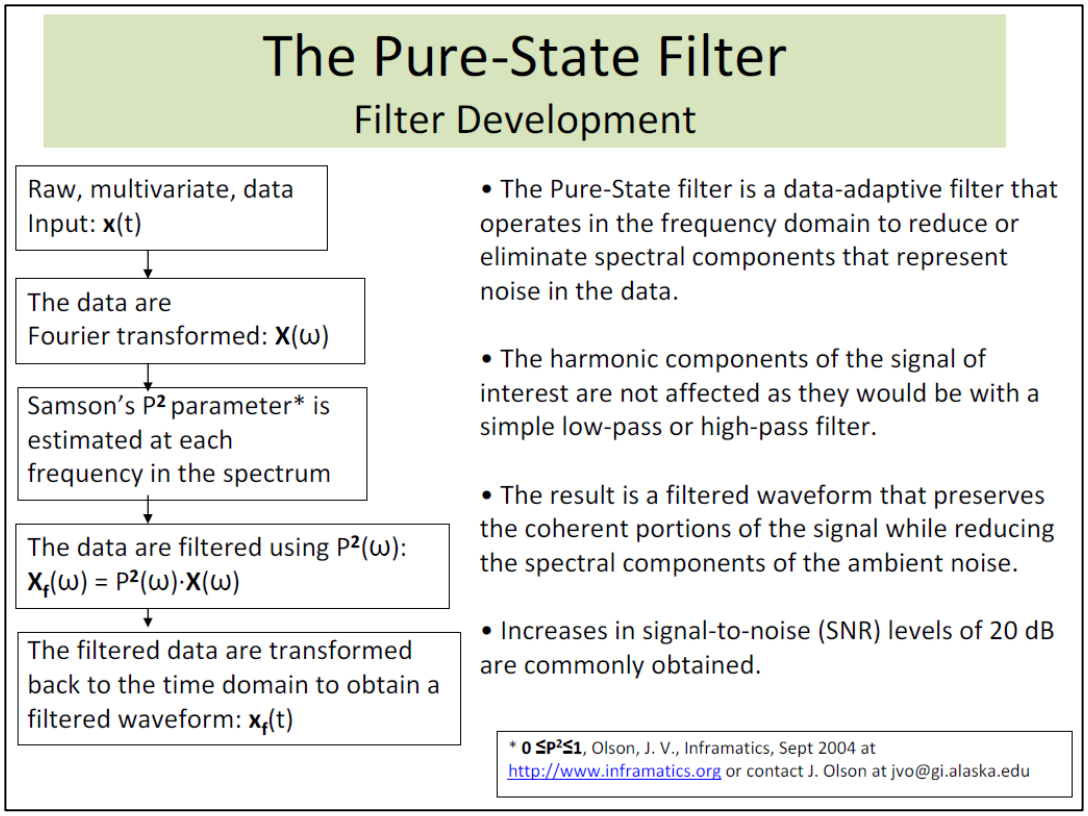


Figure 5-1 The Pure-State Filter Development Flow as Presented by J. Olsen at US Infrasound Team Meeting, Oxford MS. 2009 [Olsen, 2009]

Figure 5-2 below shows the process steps that a signal processing analyst might follow when using the Pure State filter in a typical infrasound signal processing application.

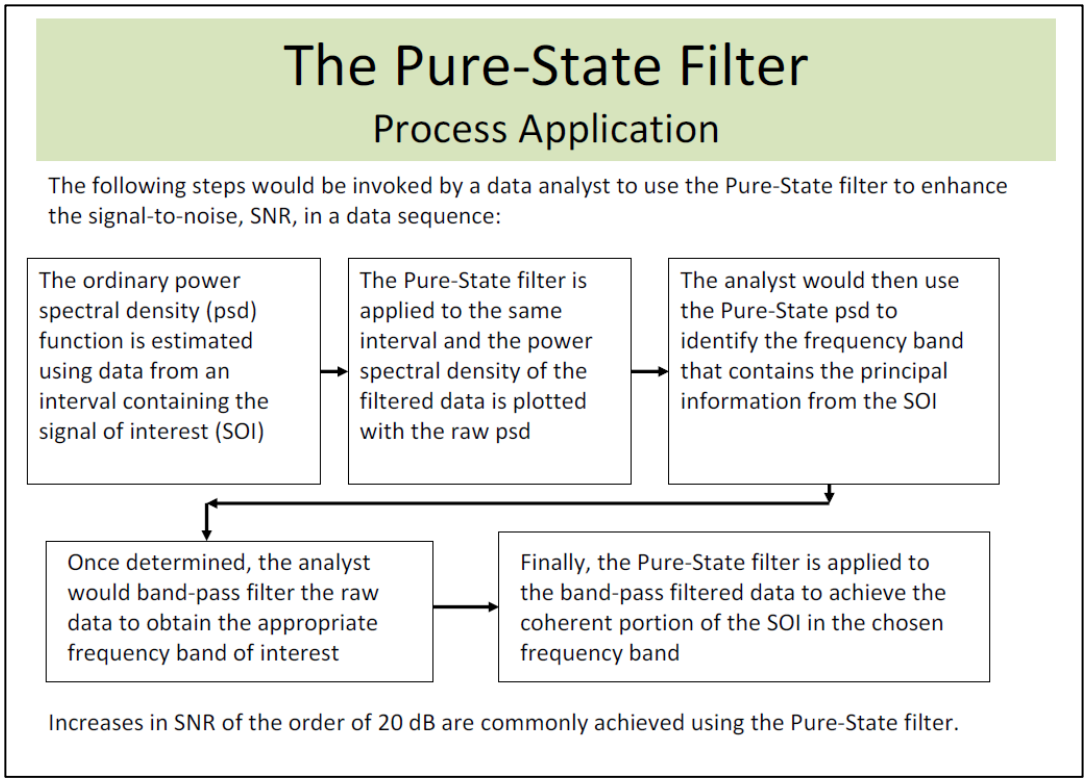


Figure 5-2 The Pure State Filter Process Application as Presented by J. Olsen at US Infrasound Team Meeting, Oxford MS. 2009 [Olsen, 2009]

## 5.3 Test Signals/Data Used for Experiment

Several signals were selected as "test" signals with a primary objective being to represent a wide cross-section of signals that are of interest to the seismic/infrasound signal processing community. Additionally, a wide range of signal sources was desired. To satisfy the dual criteria, the following test signals are presented in the following sections:

Table 5-1 Experiment Data Test Cases

| Set # | Title | Data Type | Classification | Description |
|---|---|---|---|---|
| 1 | USCG Boat | Infrasound/Seismic | Manmade | Experimental collection of test boat and background sources from 2010. |
| 2 | Atlas V | Infrasound/Seismic | Manmade | AtlasV launch from Cape Canaveral, Fl on 22 April 2010 |
| 3 | Acapulco Bolide | Infrasound/Seismic | Natural | Meteor breakup recorded over Acapulco |

| | | | | |
|---|---|---|---|---|
| 4 | Rocket Motor Detonation | Infrasound/Seismic | Manmade | Destructive demolition of obsolete ICBM rocket motors recorded from a test range in Utah |

### 5.3.1 U.S. Coast Guard Boat Experiment

In December of 2010 a joint research team fielded an infrasound monitoring array on the end of a pier at the U.S. Coast Guard station in Key West, Florida. This 6-channel array was part of the Mobile MASINT Ground Sensor System (M2UGS) being developed by the Northrup Grumman Corporation and used to source data products processed jointly with a team from the Florida Institute of Technology [Coots, et. al., 2016]. The M2UGS sensor array included 4 infrasound sensors and 2 seismic sensors. The target/test vehicle for the experiment was a United States Coast Guard boat. Figure 5-3 below shows a photograph of the sensor package and the USCG boat. This 33' vessel, called the SPC-LE Fast-Interceptor included 3 Mercury Verado outboard engines having 300 HP each.

Figure 5-3 USCG Boat Experiment – Infrasound/Seismic Sensor Deployment (top) & Test Boat (Bottom) Used as Part of Field Experiment Conducted in Key West Fl. December, 2010 [Coots, et. al, 2016]

To provide a range of signals for the sensor suite, the test subject boat made several laps over a predefined course. The boat left the end of the pier (adjacent to the sensor array) and then traveled outbound for approximately 1 mile to a channel buoy where the boat looped around and made a return to the pier. This course was repeated several times over the course of the experiment. While the response from the subject boat was collected, various "unintended" signals were also collected. During the

experiment various other boats entered and left the test area. Several aircraft flew overhead as well. All of these data sources were recorded in the experiments "ground truth" log. Figure 5-4 below shows a diagram of the sensor array geometry in the left panel. The array is configured in a common "Y" shape with infrasound sensors at the extrema and center of the array and two seismic sensors near the interior.

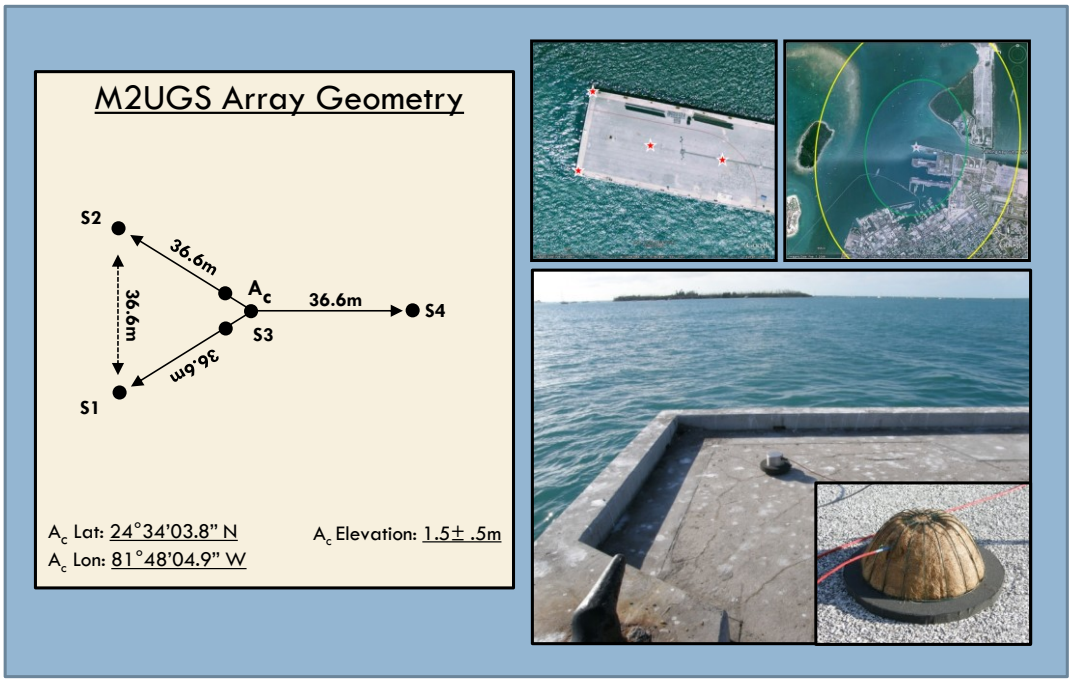


Figure 5-4 USCG Boat Experiment – Sensor Geometry and Physical Layout [Arrasmith, et. al., 2015]

In order to satisfy the Nyquist sampling theory, we must be able to sample at least two wavelengths along the array. Assuming a sound propagation speed of 343 m/s, the length of the array arm determines the frequency for the array by:

$$\frac{343\ m/s}{2*36.6m} = 4.78\ Hz \quad (1)$$

By equation N above, the M2GS array was designed for infrasound signals down to about 5 Hz. The right panel of Figure 5-4 shows aerial views of the pier where the experiment was conducted and the arrangement of the sensor array on the pier. The lower right panel shows photographs of the seismic and infrasound sensors.

Table 5-2 below provides a tabular listing of the sensor data for the USCG Key West experiment. The table indicates the array name (A439), element names, which type of infrasound micro barometer (sensor) was used for each element, and the coordinates for each sensor in latitude and longitude.

Table 5-2 USCG Boat Data – Sensor Locations

| Station Name | Element Name | Sensor Type | Latitude | Longitude |
|---|---|---|---|---|
| A439 | A4391 | Chapparal 2.0 | 24.5677 | -81.8016 |
| | A4392 | Chapparal 2.0 | 24.5677 | -81.8016 |
| | A4393 | Chapparal 2.0 | 24.5677 | -81.8016 |
| | A4394 | Chapparal 2.0 | 24.5677 | -81.8016 |
| | A4395 | Chapparal 2.0 | 24.5677 | -81.8016 |
| | A4396 | Chapparal 2.0 | 24.5677 | -81.8016 |

Processing of the U.S. Coast Guard boat data begins by using the standardized tool, Inframonitor to process the array data and thereby establish a baseline for the processed data results. We can then process the same data with the MIDAS filter and observe any changes in the results. The processing flow begins by pre-filtering the input data and then selecting the array of interest on which to search for detections. The adaptive F-statistic detection algorithm used by the Inframonitor tool typically provides improved results (fewer false detections) over standard F-detection methods by automatically adjusting to correlated background noise sources [Arrowsmith, 2012]. Figure 5-5 below shows the results of the Inframonitor processing with standard band-pass filtering applied (1-200Hz) and detections identified. In a general sense, the spiked responses represent some type of signal received by the array that is larger than the ambient noise which is represented by the constant line at the middle of the plot. In most cases the test conductor will capture a log of the test activity and any relevant events that occurred during the collection window. This "ground truth" log can be used during the post-processing effort to help identify which spikes in the time domain plot are actual signals of interest, which are extraneous signals and which are noise.

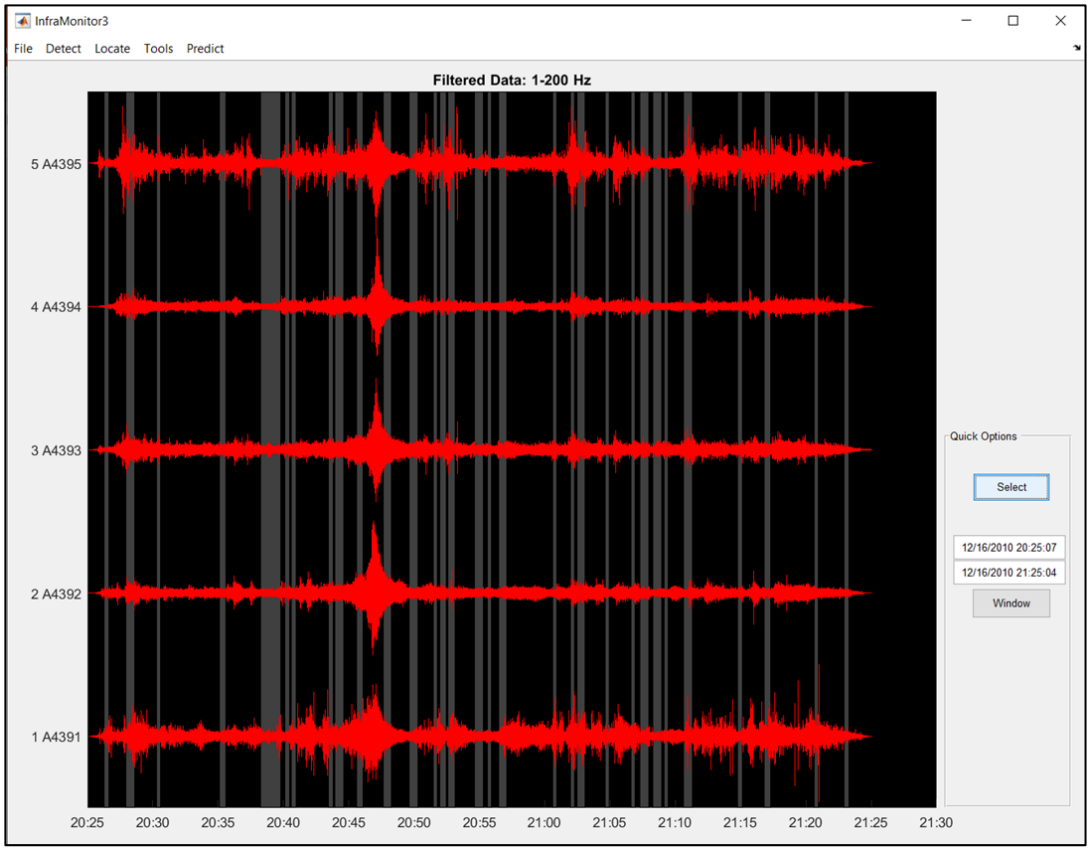


Figure 5-5 USCG Boat Data – Inframonitor Output with Standard Bandpass Filter Processing (1-200Hz) Showing Detections

Next, the detections can be identified by observing the vertical grey bars on the plot. The detections represent transient areas in the input signal having high signal-to-noise ratio. A review of the figure quickly identifies the challenge in processing data with low signal-to-noise ratio. The plot indicates many vertical bars, or detections that are actually false detections. These points in the input signal were identified by the detection algorithm because they met the threshold criteria for channel-to-channel coherency, transient response and signal-to-noise ratio. Unfortunately, low SNR may cause false detections due to seemingly correlated noise across the array.

An extension of the InfraMonitor tool called ImPlot is used to plot the detection results for a selected sensor channel. Figure 5-6 below shows the result for Channel #1 of the A4391 sensor data. Typically, selecting the highest F-statistic result within the trace is the preferred method to further resolve the detection. The F-statistic plot (shown in the top panel) is a measure of the correlation across all channels versus time. The second panel from the top shows the correlation coefficient and provides an indication of the incoming signal's phase relationship at each array channel. In this example the correlation coefficient for the selected array was 0.21. As this parameter is highly sensitive to the signal-to-noise of the input signal, effective pre-filtering of the data should improve this metric. The third panel from the top is the azimuth estimation back to the originating source event (or back-azimuth). The fourth panel from the top is the phase velocity plot and indicates the speed with which the incident sound field propagated across the array. The bottom panel on the plot shows a time domain view of the input data for the selected array channel.

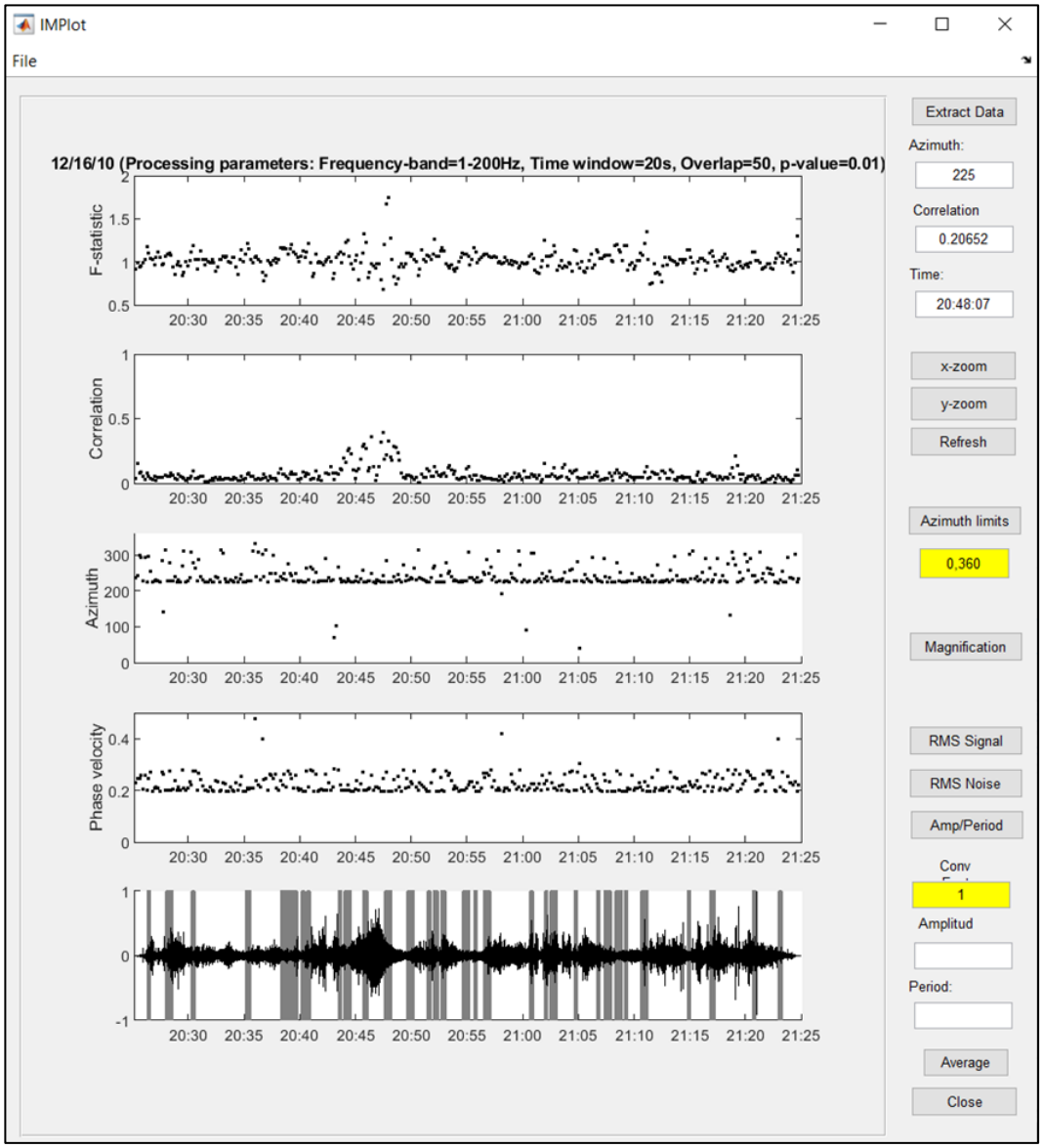


Figure 5-6 USCG Boat Data – IMPlot Output Showing Detections for Sensor A439 Channel #1 After Band-pass (1-200Hz) Filtering

The USCG boat data was also processed by using the Pure-State filter tool after the standard bandpass filter had been applied. The Pure State filter is a well-known and accepted filter tool within the infrasound and seismic community. As such, it provides a relevant metric for performance comparison when evaluating the MIDAS filter. The detection results for the Pure State filter are shown below in Figure 5-7.

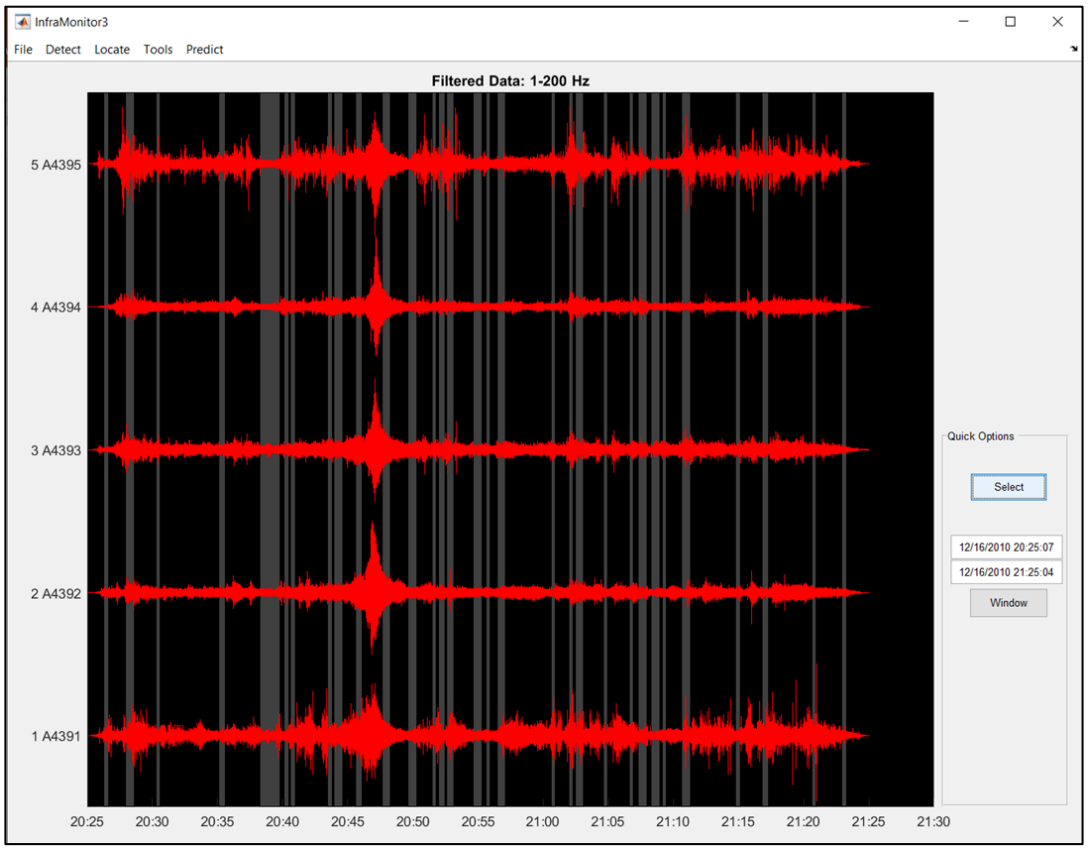


Figure 5-7 USCG Boat Data – Inframonitor Output with Pure-State Filter Processing (1-200Hz) Showing Detections

With the Pure-State filter, the correlation coefficient was improved relative to the bandpass filter alone. Specifically, the correlation improved from 0.21 to 0.42. The

number of detections was also increased relative to the bandpass filter alone (although in this case the increased number of detections is inconsistent with the ground truth). Additionally, the phase velocity and azimuth were nearly identical between the band-pass and the Pure State filters. Figure 5-8 below shows the result for Channel #1 of the A4391 sensor when processed with the Pure State filter.

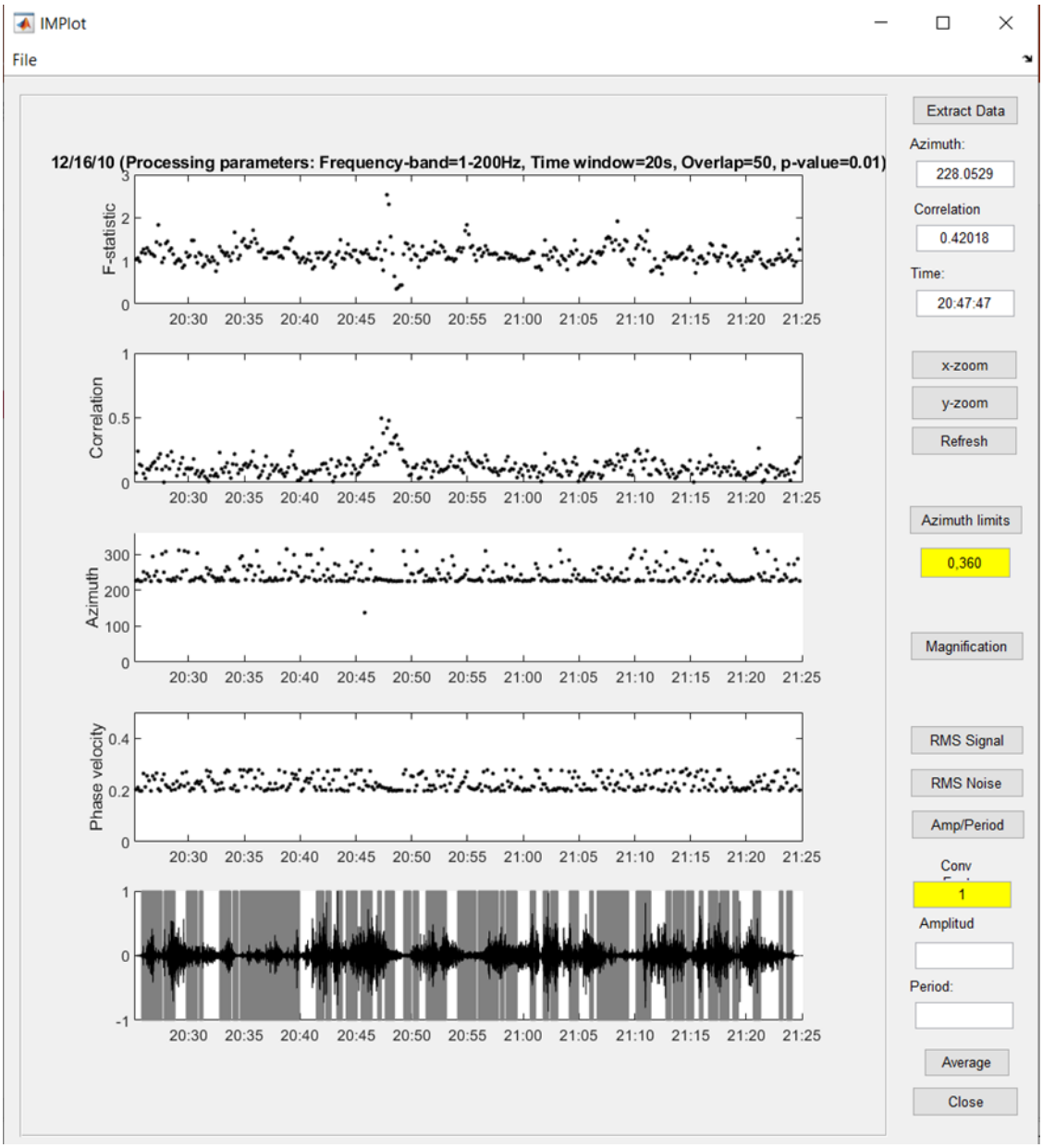


Figure 5-8 USCG Boat Data – IMPlot Output Showing Detections for Sensor A439 Channel #1 After Pure-State Filtering

Next, the same input data set was processed with the MIDAS filter for comparison to the bandpass and Pure State filter results. One observation that can be readily made upon review of the figure below is that the MIDAS filtered data seems to have a lower peak amplitude across the processing window, as much of the channel and station noise has already been filtered out. Additionally, the number of detections (indicated by the vertical gray bars in the plot) is very similar to the major detections previously identified in the bandpass filter case, and when compared to the ground truth, there are fewer false detection than were identified with the Pure State filter. Figure 5-9 below shows the result of the MIDAS filter processing.

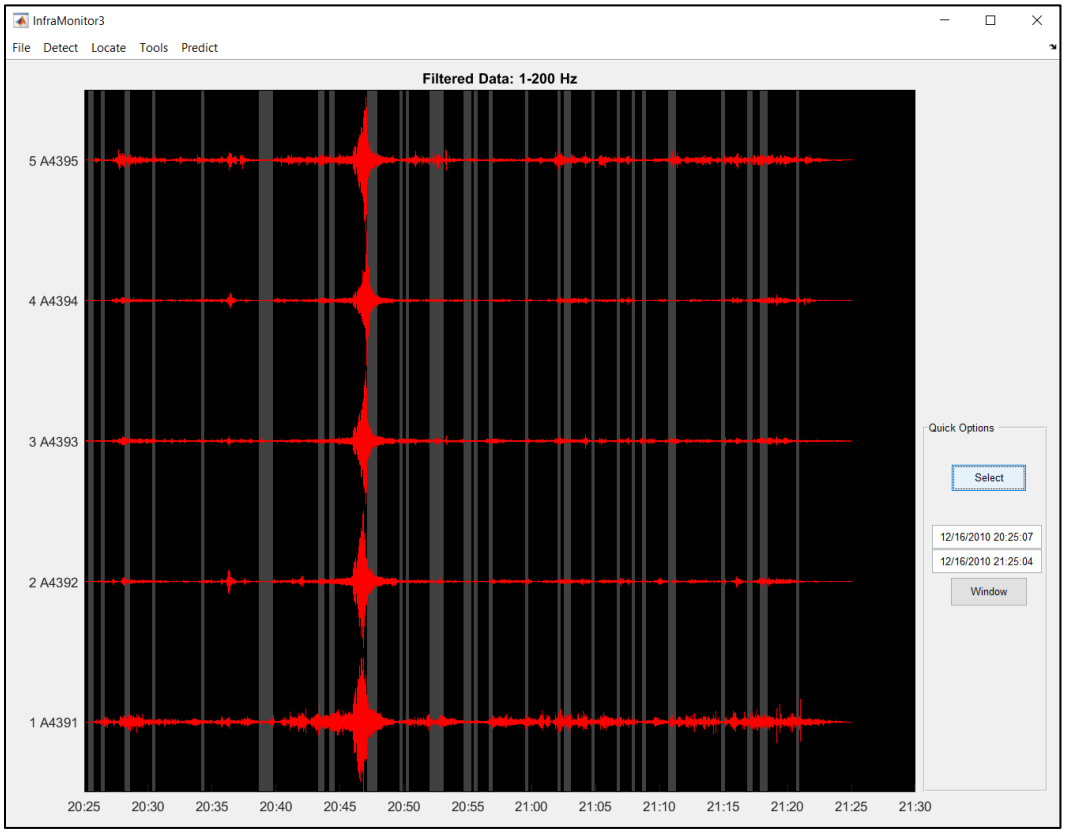


Figure 5-9 USCG Boat Data – Inframonitor Output with MIDAS Filter Processing (1-200Hz) Showing Detections

In the MIDAS filtered example, the USCG boat data produced significantly better correlation statistics than the standard (band-pass filter) method. In the MIDAS filtered case, when the same detection that was evaluated previously is processed, the result indicated a correlation coefficient of 0.469 in Figure 5-10 below. This is increased relative to the 0.21 seen earlier with the standard bandpass filter. The 0.469 is slightly better than the 0.42 observed with the Pure-State filter.

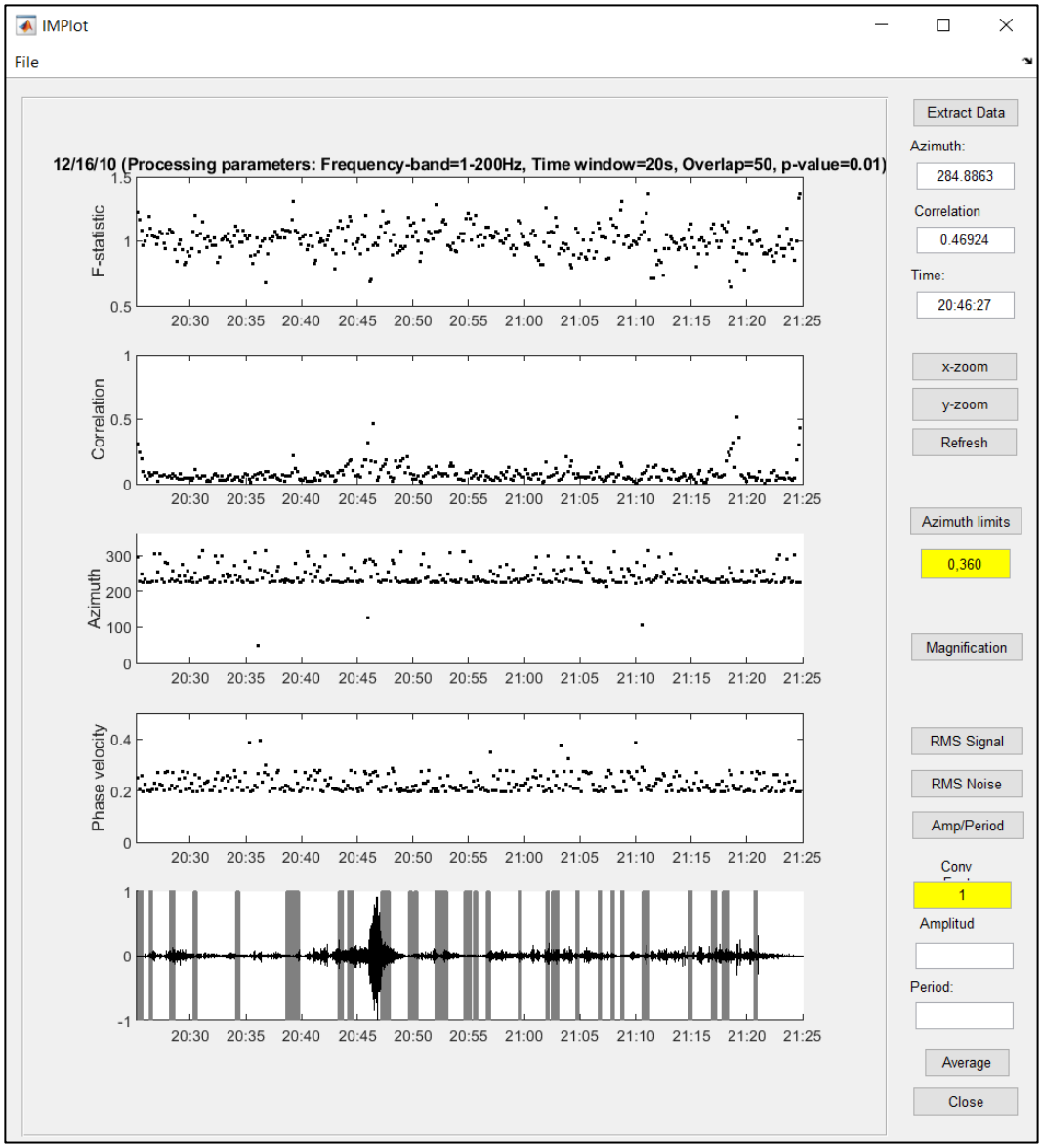


Figure 5-10 USCG Boat Data – IMPlot Output Showing Detections for Sensor A439 Channel #1 After MIDAS Filtering

## 5.3.2 Acapulco Bolide Experiment

On August 25, 2000 a meteor estimated to be approximately 10 feet in diameter entered the atmosphere over the Pacific Ocean and ultimately broke up off the coast of Acapulco, Mexico. Meteors that explode in the atmosphere in this way are called Bolides. This particular high-altitude blast had an estimated yield equivalent to that of 7,000 tons of TNT [Brown, ReVelle, Whittaker, 2001]. Numerous seismic and infrasound sensors around the globe recorded this event.

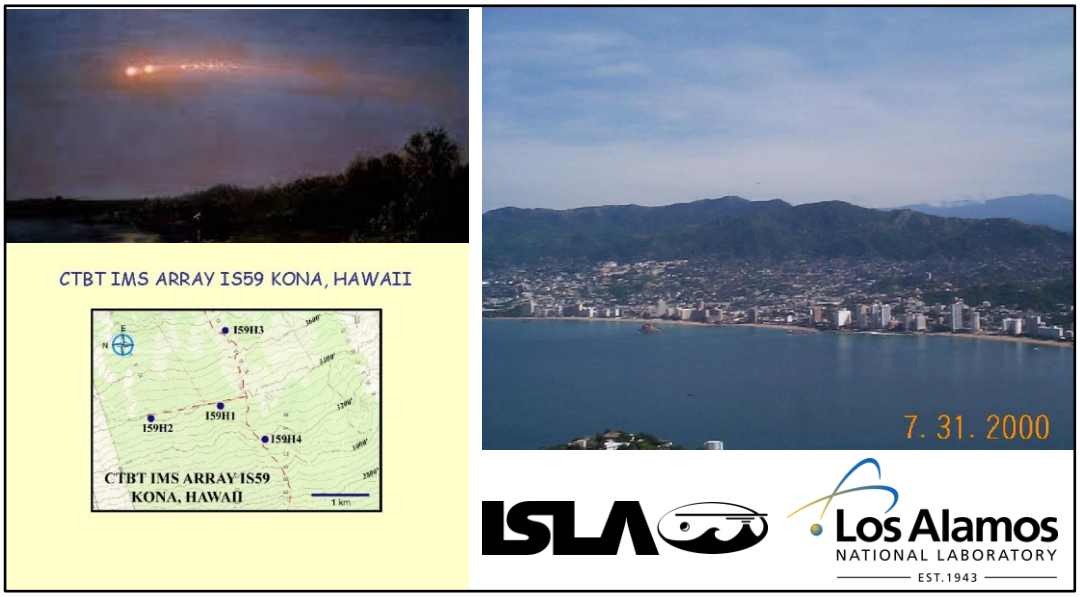


Figure 5-11 Acapulco Bolide Data – Sensor Geometry [Brown, et.al., 2001]

For this research, a data set was processed that was composed of infrasound data collected by sensors at the IMS array in Kona, Hawaii and the infrasound array at Los Alamos National Laboratory in New Mexico. Table 5-3 below provides a tabular listing of the sensor data for the Kona and Los Alamos arrays used in the Acapulco Bolide data collection. The table indicates the array names (I59H and DLIO), associated element names, which type of infrasound microbarometer (sensors) were used for each element, as well as the coordinates for each sensor in latitude and longitude.

Table 5-3 Acapulco Bolide Data – Sensor Locations

| Station Name | Element Name | Sensor Type | Latitude | Longitude |
|---|---|---|---|---|
| DLI0 | DLI01 | Chapparal 2.0 | 35.8741 | -106.3325 |
| | DLI02 | Chapparal 2.0 | 35.8636 | -106.3254 |
| | DLI03 | Chapparal 2.0 | 35.8655 | -106.3401 |
| | DLI04 | Chapparal 2.0 | 35.8676 | -106.3342 |
| I59H | I59H1 | Chapparal 2.0 | 40.07945 | -155.8951 |
| | I59H2 | Chapparal 2.0 | 40.08006 | -155.8819 |
| | I59H3 | Chapparal 2.0 | 40.07196 | -155.8994 |
| | I59H4 | Chapparal 2.0 | 40.07864 | -155.8934 |

Similar to our previous approach, processing of the Acapulco bolide data begins by using the standardized tool, Inframonitor to process the array data and thereby establish a baseline for the processed data results. As before, the processing flow

using the Inframonitor tool begins by pre-filtering the input data and then selecting the array of interest on which to search for detections. In this case, there were two arrays available (I59H and DLI0) with 4 channels each. The DLI0 array was chosen for processing and Figure 5-12 below shows the results for the band-pass filtered case. In this example, a single band of detections were identified at approximately 3:29 in the time history.

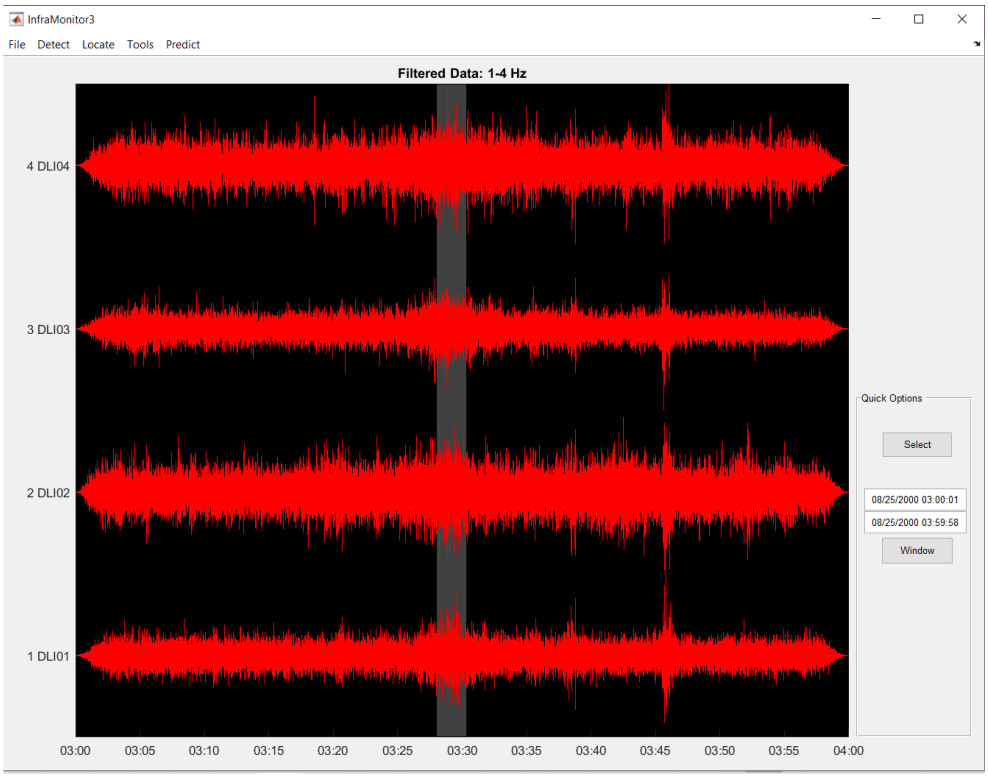


Figure 5-12 Acapulco Bolide Data – Inframonitor Output with Standard Bandpass Filter Processing (1-4Hz) Showing Detections

Selecting one of the dominant F-statistic results for processing identifies a strongly correlated portion of the input signal and provides a good candidate for a correlation coefficient baseline. In the Acapulco bolide example, the bandpass filtering method resulted in a correlation coefficient of 0.35. The detection data for sensor DLI0, Channel #1 is shown below in Figure 5-13.

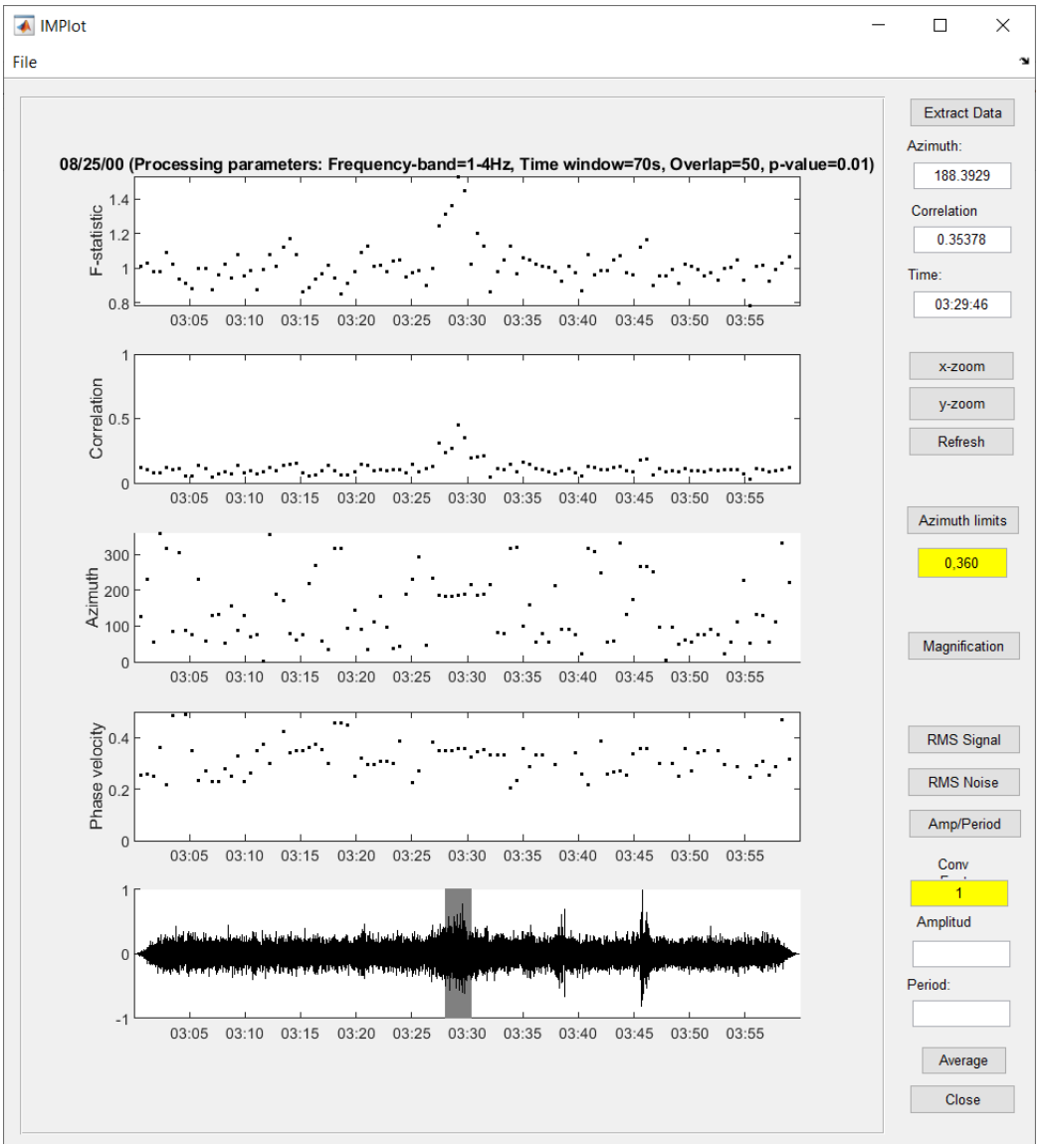


Figure 5-13 Acapulco Bolide Data – IMPlot Output Showing Detections for Sensor DLI0 Channel #1 After Band-pass Filtering

The Acapulco bolide data was also processed by using the Pure-State filter tool after the standard bandpass filter had been applied. The detection results for the Pure State filter are shown below in Figure 5-14.

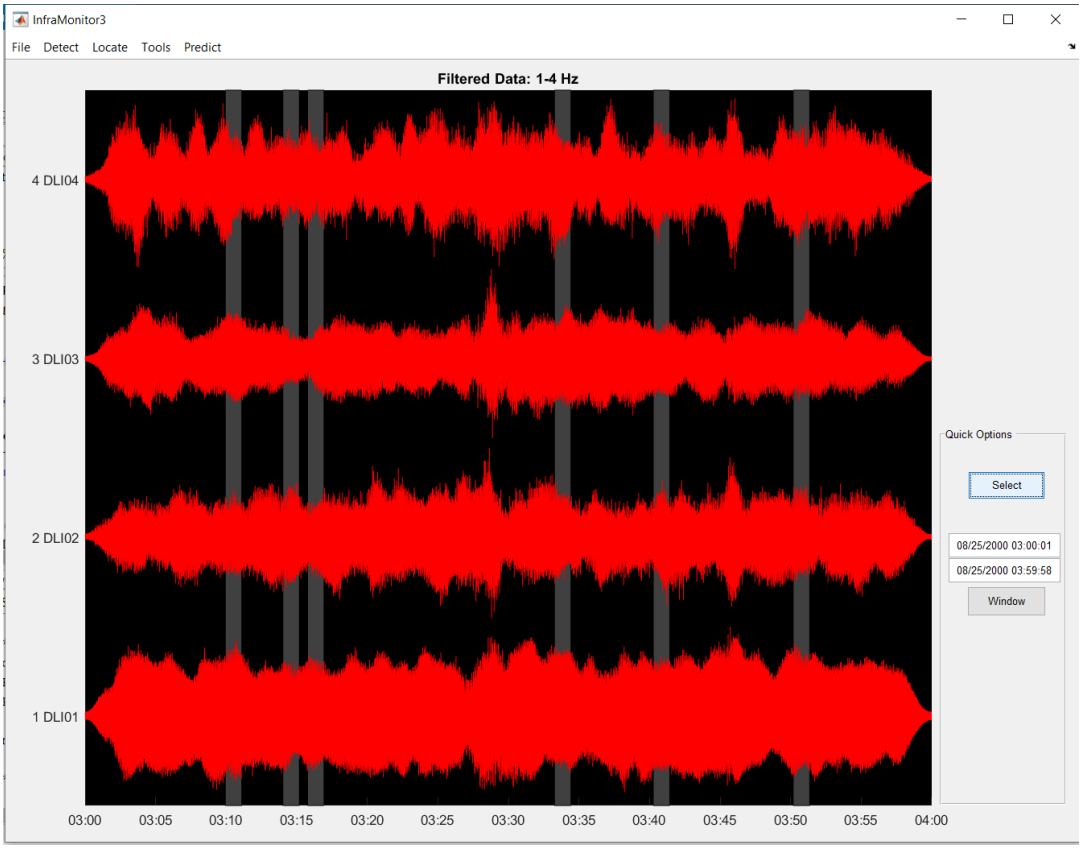


Figure 5-14 Acapulco Bolide Data – Inframonitor Output with Pure State Filter Processing (1-4Hz) Showing Detections

With the Pure-State filter, the correlation coefficient was improved relative to the bandpass filter alone. Specifically, the correlation improved from 0.35 to 0.61. The number of detections was also increased relative to the bandpass filter alone. Additionally, the phase velocity and azimuth were nearly identical between the band-pass and the Pure State filters. Figure 5-15 below shows the results of the Pure State filtering operation for the DLI0 Channel#1 signal.

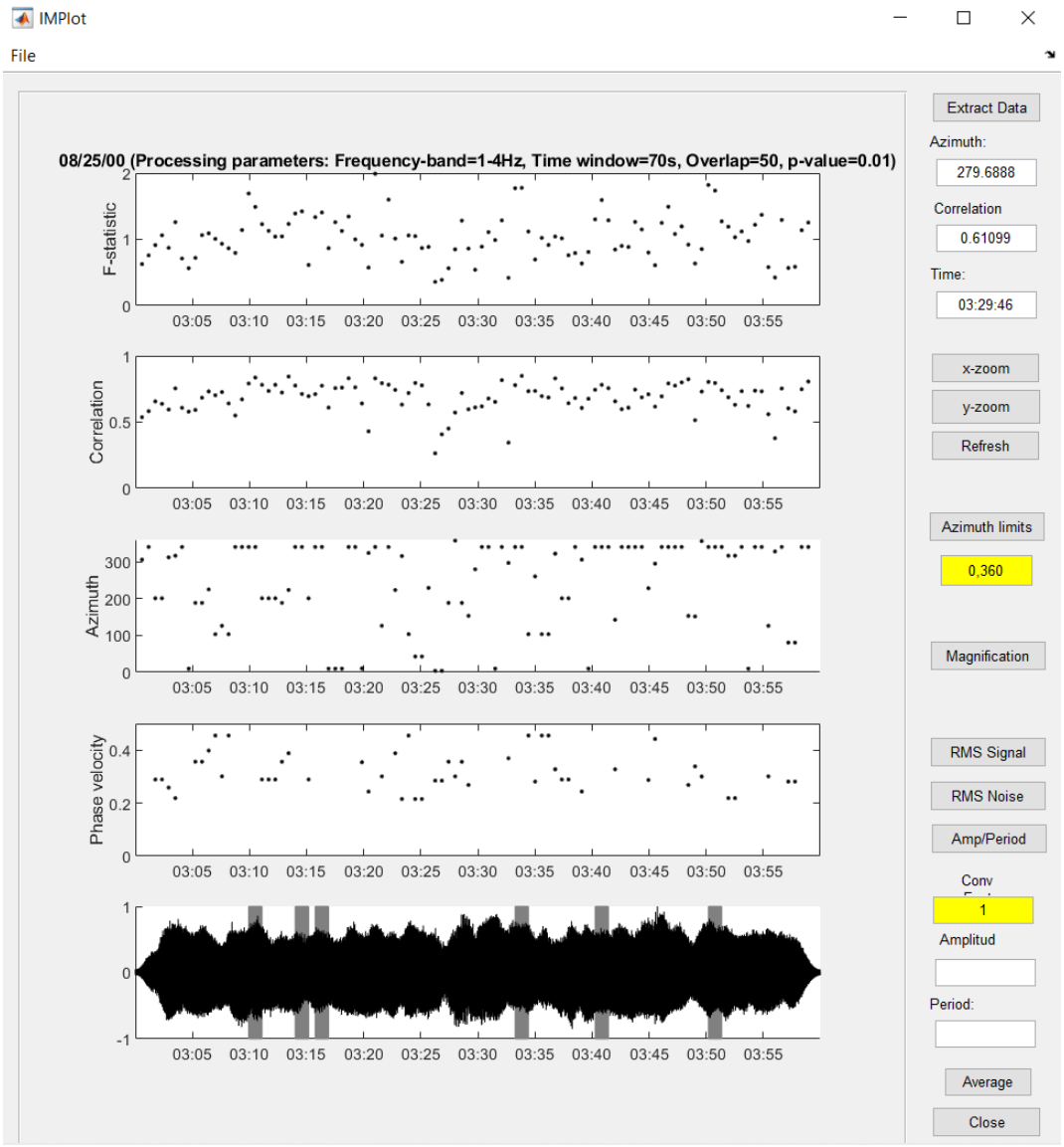


Figure 5-15 Acapulco Bolide Data – IMPlot Output Showing Detections for Sensor DLI0 Channel #1 After Pure State Filtering

Next, the same input data set was processed with the MIDAS filter for comparison, and the results are shown in Figure 5-16 below. One observation that can readily be made upon review of the figure below is that the MIDAS filtered data seems to have

a lower peak-to-peak amplitude across the processing window, since much of the channel and station noise has been filtered out. The time domain data after MIDAS filtering provides a much clearer view of the bolide signature than that of the bandpass filter. Additionally, the number of detections (indicated by the vertical gray bars in the plot) identified in the MIDAS filter case is increased.

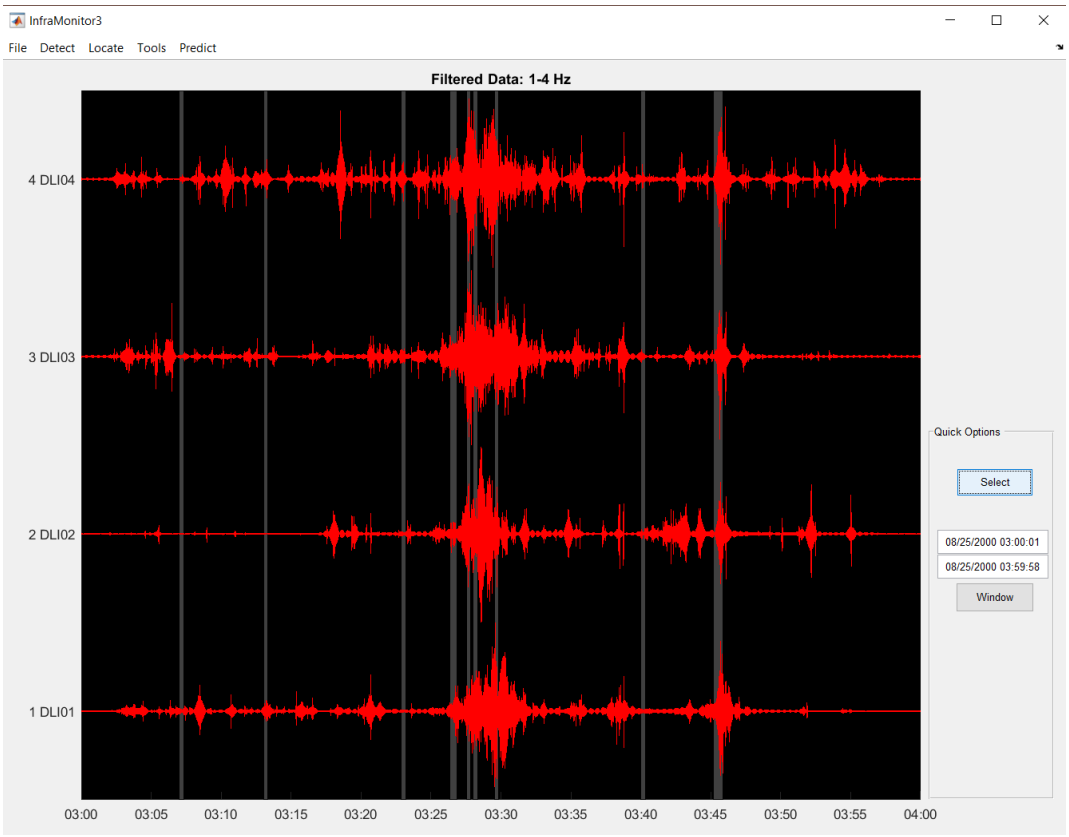


Figure 5-16 Acapulco Bolide Data – Inframonitor Output with MIDAS Filter Processing Showing Detections

In the MIDAS filtered example, the Acapulco bolide data produced significantly better correlation statistics than the standard (band-pass filter) method. In the MIDAS filtered case, when the same bolide detection that was evaluated previously is processed, the result indicated a correlation coefficient of 0.647. This is improved relative to the 0.35 seen earlier with the bandpass filter. The detection data for sensor DLI0, Channel #1 is shown below in Figure 5-17. Inspection of the lower panel (time domain plot) indicates a handful of additional detections as compared to the band-pass filtered case from Figure 5-12 above. The top panel (F-statistic) from Figure 5-17

has peaks at approximately 3:14, 3:21 & 3:45 indicting that these locations had higher correlations than surrounding regions but did not quite meet the detection threshold criteria. The additional signal improvement gained by processing with the MIDAS filter allowed the data to meet the detection threshold in these locations, hence the additional detections relative to the band-pass filter.

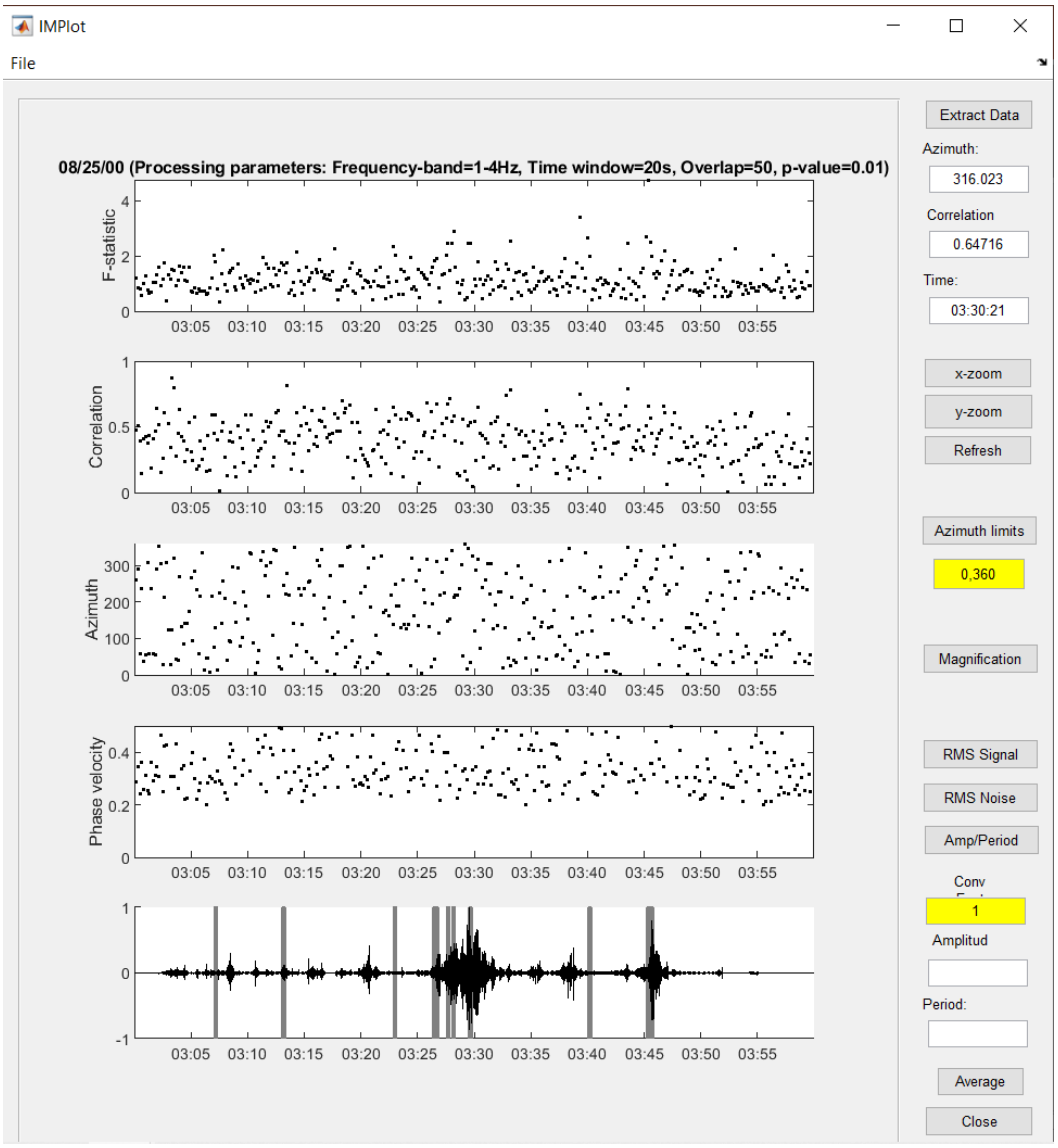


Figure 5-17 Acapulco Bolide Data – IMPlot Output Showing Detections for Sensor DLI0 Channel #1 After MIDAS Filtering

## 5.3.3 Utah Test and Training Range Experiment

An additional man-made data signal source evaluated during this research comes from explosions recorded at the Utah Test and Training Range (UTTR) at Hill Air Force Base. At a rate of approximately every two weeks, decommissioned ICBM rocket motor stages are disposed of by detonation at UTTR. These regular data sources provide an ample library of seismic and infrasound signals (with ground truth) that date back to at least 2005. Numerous infrasound stations, infrasound arrays and seismic sensors are deployed around the UTTR. For this research, data from 4 infrasound arrays (HMU, BGU, WMU and FSU) was processed and compared.

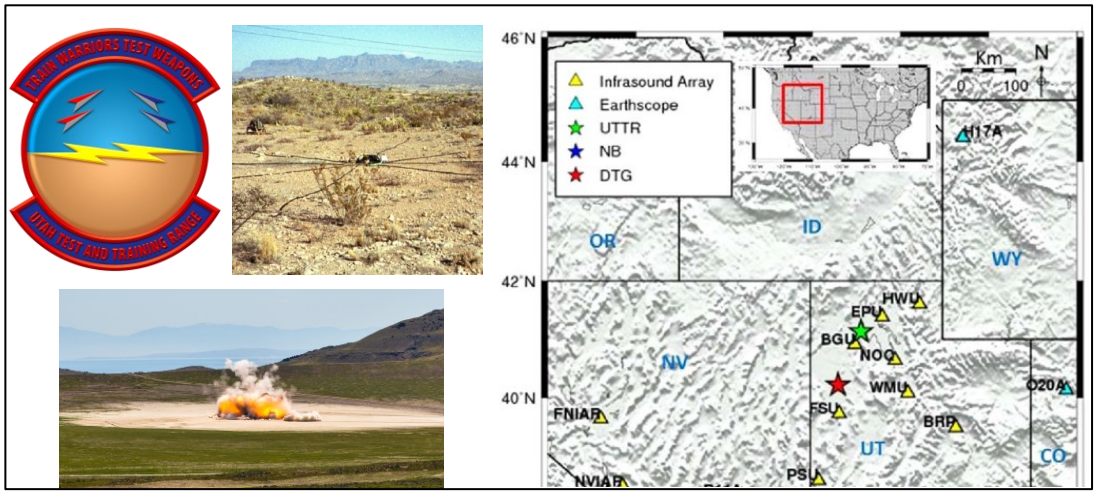


Figure 5-18 Utah Test and Training Range (UTTR) Data – Sensor Geometry and Physical Layout [Talmadge, et. al., 2011]

For this research, a data set was processed that was composed of infrasound data collected by sensors at 4 different locations in, and around the Utah Test and Training Range (UTTR) at Hill Air Force Base, Utah [Talmadge, et. al., 2011]. Table 5-4 below provides a tabular listing of the sensor data for the 4 arrays used in the UTTR data collection. The table indicates the array names (FSU, WMU, HMU and BGU), associated element names, which type of infrasound micro barometer (sensors) were used for each element, as well as the coordinates for each sensor in latitude and longitude.

Table 5-4 UTTR Data – Sensor Locations

| Station Name | Element Name | Sensor Type | Latitude | Longitude |
|---|---|---|---|---|
| FSU | FSU1 | Validyne | 39.72195 | -133.39132 |
| | FSU2 | Validyne | 39.72295 | -133.39204 |
| | FSU3 | Validyne | 39.72258 | -133.3904 |
| | FSU4 | Validyne | 39.72131 | -133.39036 |
| | FSU5 | Validyne | 39.72131 | -133.39204 |
| WMU | WMU1 | Chapparal 2.0 | 40.07945 | -111.83103 |
| | WMU2 | Chapparal 2.0 | 40.08006 | -111.82949 |
| | WMU3 | Chapparal 2.0 | 40.07196 | -111.82907 |
| | WMU4 | Chapparal 2.0 | 40.07864 | -111.83012 |
| | WMU5 | Chapparal 2.0 | 40.0794 | -111.83001 |
| HMU | HMU1 | Chapparal 2.0 | 41.6071 | -111.5642 |
| | HMU2 | Chapparal 2.0 | 41.6065 | -111.5659 |
| | HMU3 | Chapparal 2.0 | 41.6078 | -111.5656 |
| | HMU4 | Chapparal 2.0 | 41.6072 | -111.5652 |
| BGU | BGU1 | Chapparal 2.0 | 40.9204 | -113.0309 |
| | BGU2 | Chapparal 2.0 | 40.9207 | -113.0301 |
| | BGU3 | Chapparal 2.0 | 40.9203 | -113.0293 |
| | BGU4 | Chapparal 2.0 | 40.9215 | -113.0299 |

To establish a baseline, the processing flow (using the Inframonitor tool) begins by pre-filtering the input data and then selecting the array of interest on which to search for detections. In this example, the WMU infrasound array was used. The adaptive F-statistic detection algorithm indicates the major events within the data set. Selecting one for processing provides a correlation coefficient baseline. Figure 5-19 shows the results for the band-pass filtered case. In this case a single small band of

detections was identified at approximately 00:39 minutes into the data collection which correlated with the known ground truth for the actual explosion event. There were also two other small detections identified (00:43 and 00:57) that were false detections.

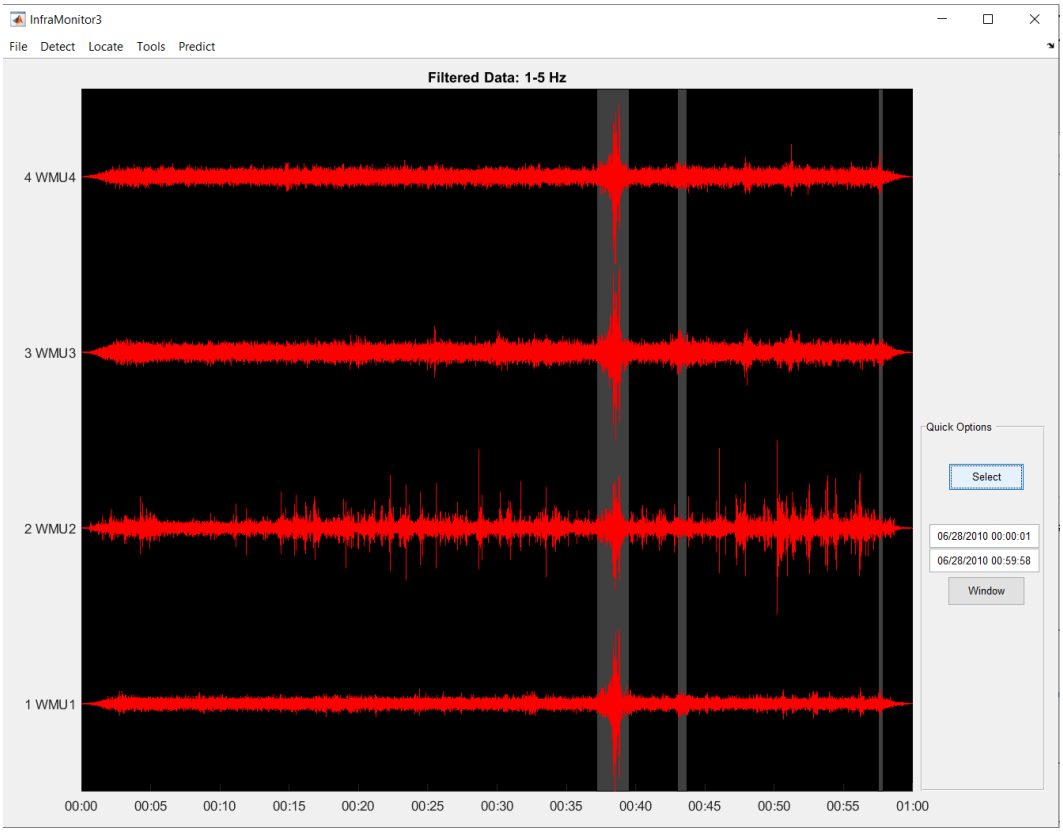


Figure 5-19 UTTR Data – Inframonitor Output with Standard Bandpass Filter Processing (1-5Hz) Showing Detections

In the UTTR example, the bandpass filtering method resulted in a correlation coefficient of 0.93. The detection data for sensor WMU, Channel #1 is shown below in Figure 5-20.

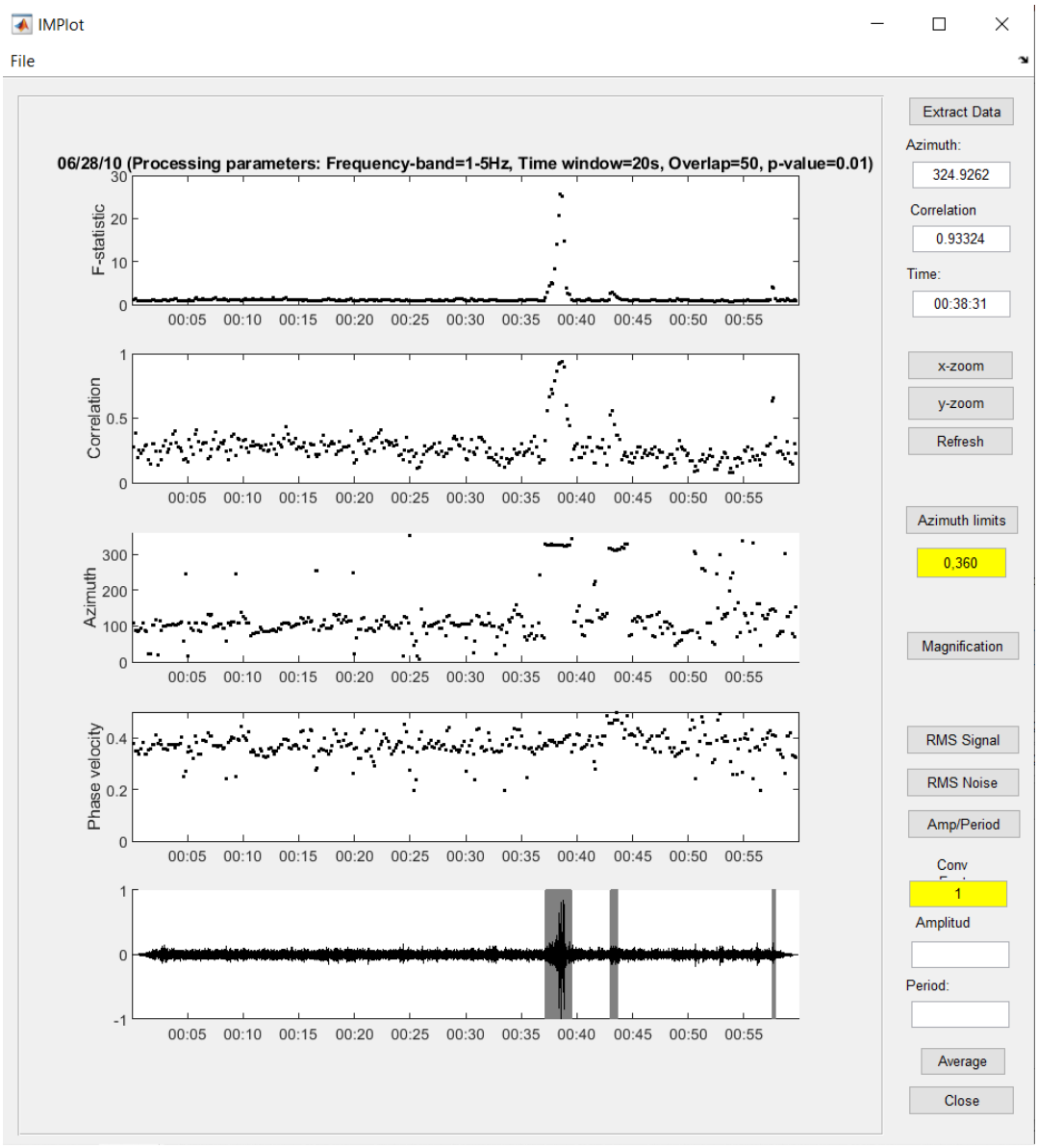


Figure 5-20 UTTR Data – IMPlot Output Showing Detections for Sensor WMU Channel #1 After Band-pass Filtering

Close inspection of the raw data indicates a single time-history event with a sharp, highly impulsive shape. This signature is indicative of an explosion event. A natural by-product of this highly impulsive signature is a strong correlation coefficient. This is consistent with the correlation coefficient of 0.93 that was reported with the band-pass filter. There is also an interesting secondary detection event identified approximately 5 seconds after the primary event, at ~00:44 seconds. Given the highly mountainous region of the test range as well as the various sensor arrays (including the WMU array being analyzed in this example), one might suspect this second detection could be attributed to a secondary detection from the primary event (multipath). However, closer inspection of the azimuth results in the third panel from the top show both the primary and secondary detected events have calculated back-azimuths of approximately 325 degrees. A multipath event would have not only been delayed in time, but also appeared to originate from a different direction. Given this, is seems that the secondary event detected may be attributed to secondary explosion the same site as the original explosion.

The UTTR data was also processed by using the Pure-State filter tool after the standard bandpass filter had been applied. With the Pure-State filter, the correlation coefficient was improved relative to the bandpass filter alone. Specifically, the correlation improved from 0.93 to 0.95. See Figure 5-21 below. The number of detections was also increased slightly relative to the bandpass filter alone (although in this case the increased number of detections shown to the left of the plot is a

processing artifact as inspection of the time domain plot and F-statistic plots indicate that there was no appreciable activity in the input signal channel prior to the primary explosion event at 00:39).

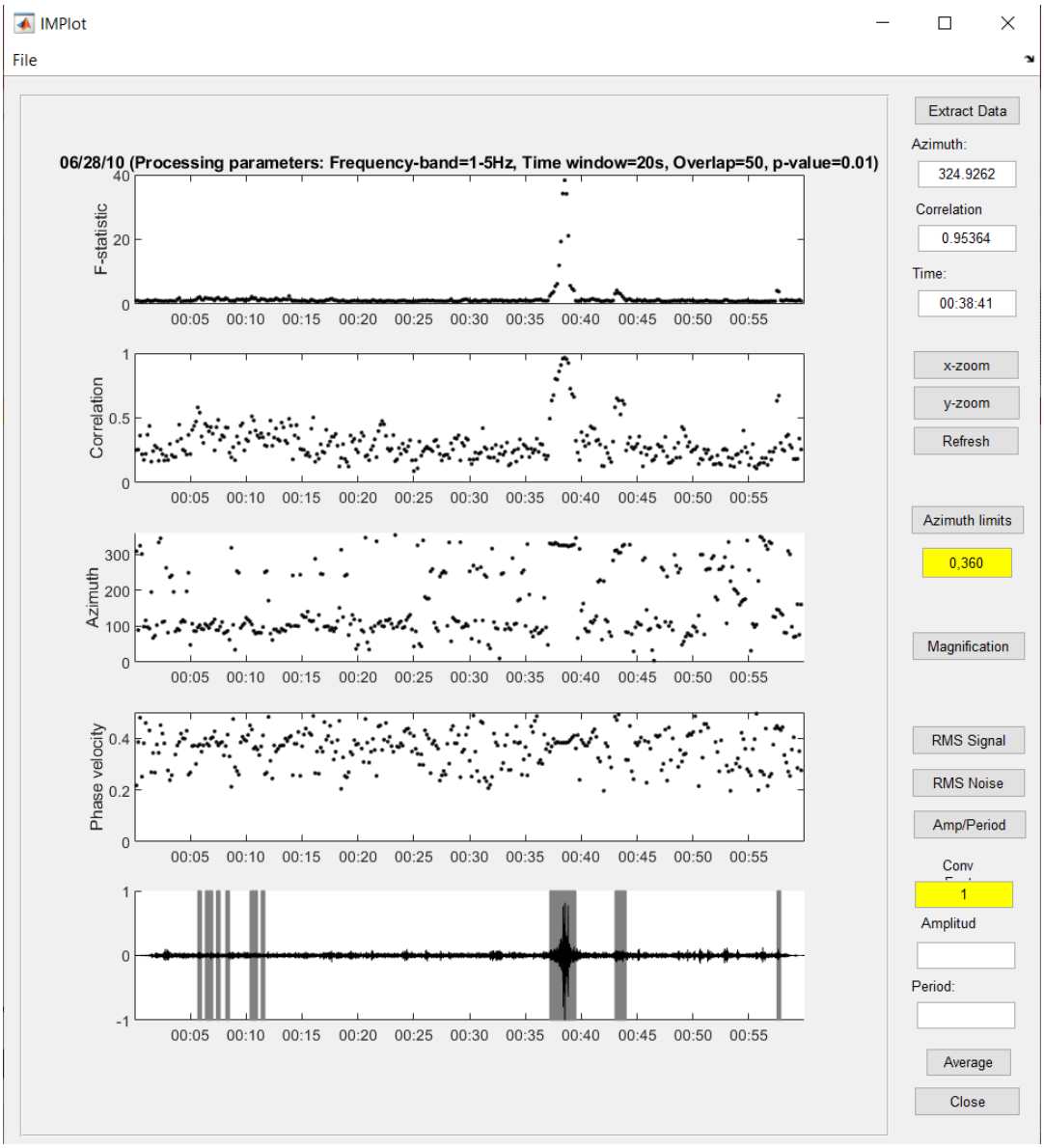


Figure 5-21 UTTR Data – IMPlot Output Showing Detections for Sensor WMU Channel #1 After Pure-State Filtering

Next, the same WMU input data set was processed with the MIDAS filter for comparison and the results are shown below in Figure 5-22.

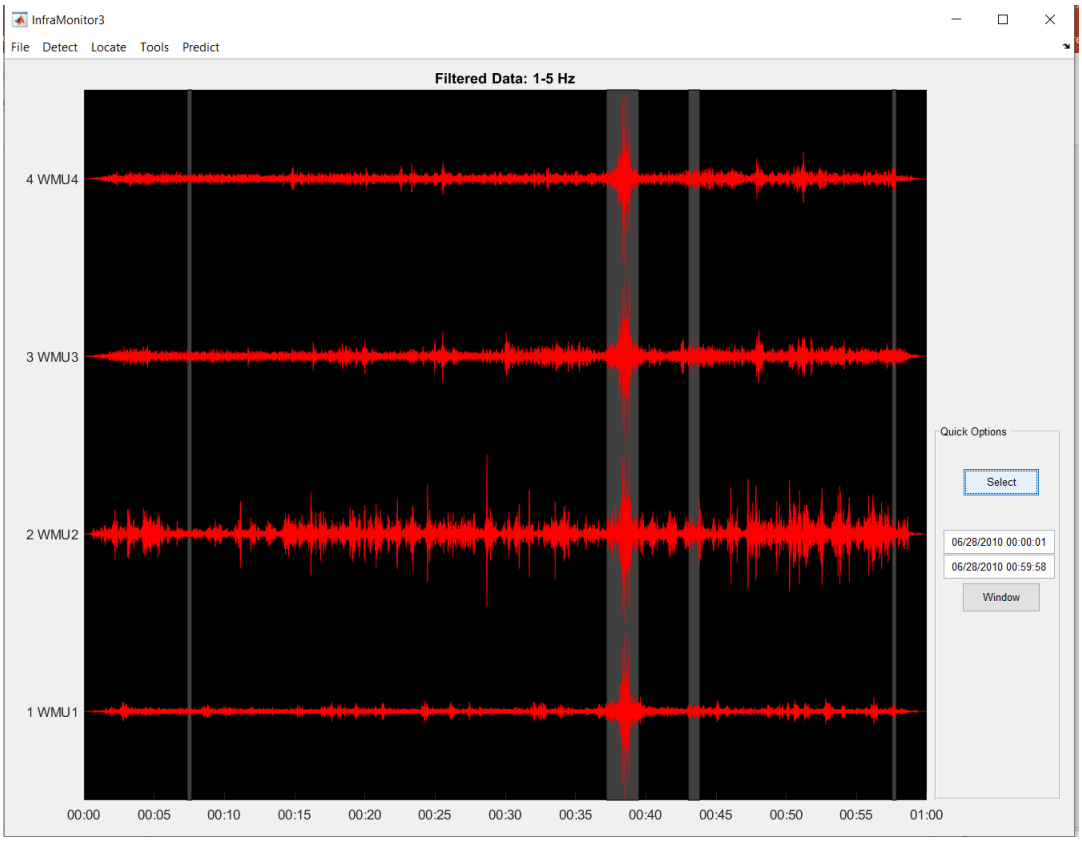


Figure 5-22 UTTR Data – Inframonitor Output with MIDAS Filter Processing Showing Detections

For the WMU data set, when processed with the MIDAS filter, the correlation coefficient is 0.97. This is slightly higher than the band-pass and Pure-State filtered results presented earlier. The detection results for the WMU sensor, Channel #1 are shown below in Figure 5-23. This particular data set is highly impulsive, has a high signal-to-noise ratio and is highly correlated across the array channels. As a result, the reported F-statistic is higher than seen on other experimental data sets. The correlation coefficients are also close to the ideal value of 1.0

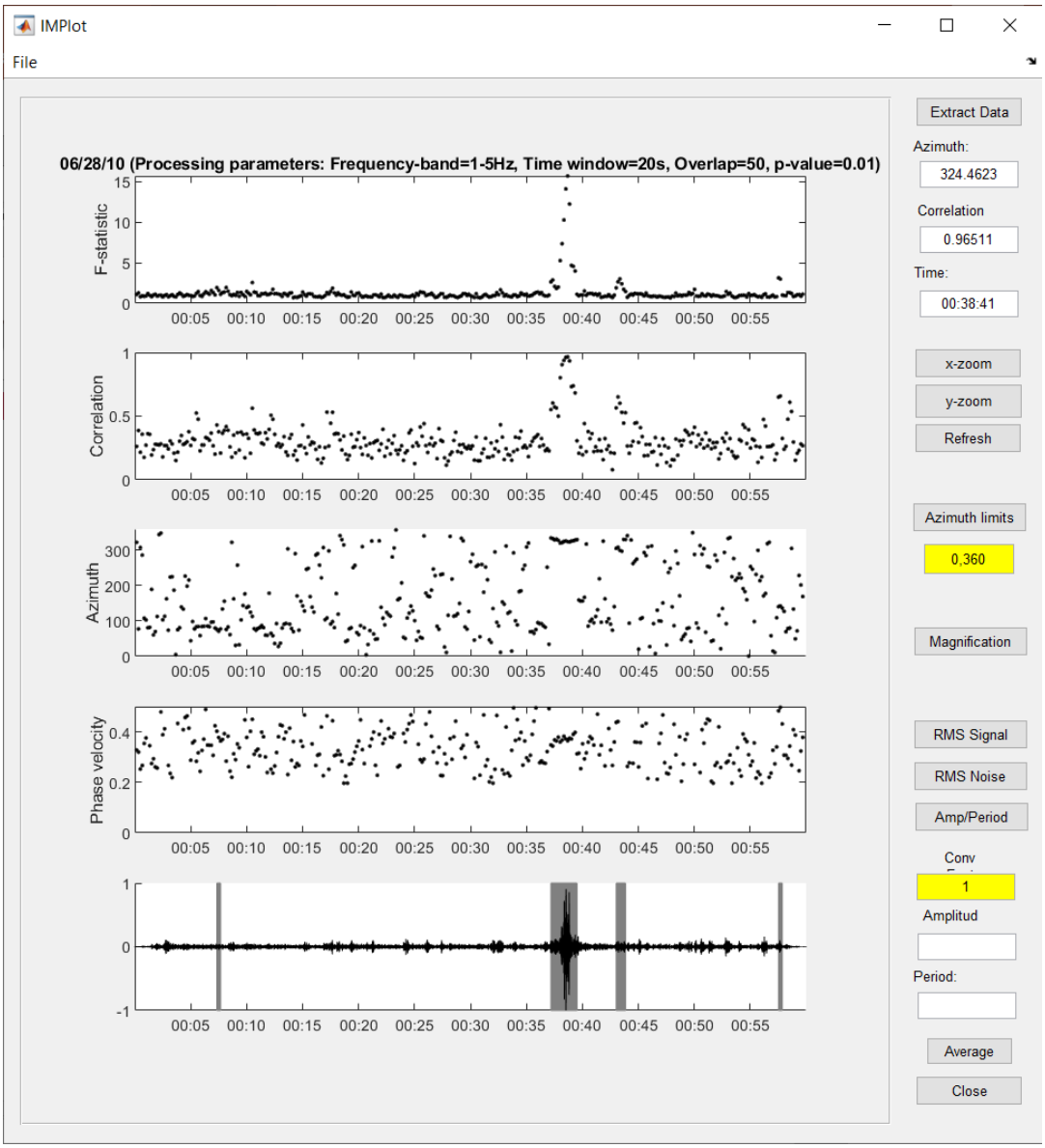


Figure 5-23 UTTR Data – IMPlot Output Showing Detections for Sensor WMU Channel #1 After MIDAS Filtering

### 5.3.4 Atlas V Launch Experiment

On April 22, 2010 the United Launch Alliance in cooperation with the Boeing Company, NASA and the United States Air Force launched the Orbital Test Vehicle-1 (OTV-1) aboard an Atlas V rocket from the Space Launch Complex 41 (SLC-41) at the Cape Canaveral Air Force Station in Florida [ULA, 2010]. Figure 5-24 below shows the launch profile for the OTV-1 mission aboard the Atlas-V rocket with the important details of the launch profile called out. This information can be used in conjunction with other ground truth data to aid in the classification of transient events identified within the input signals.

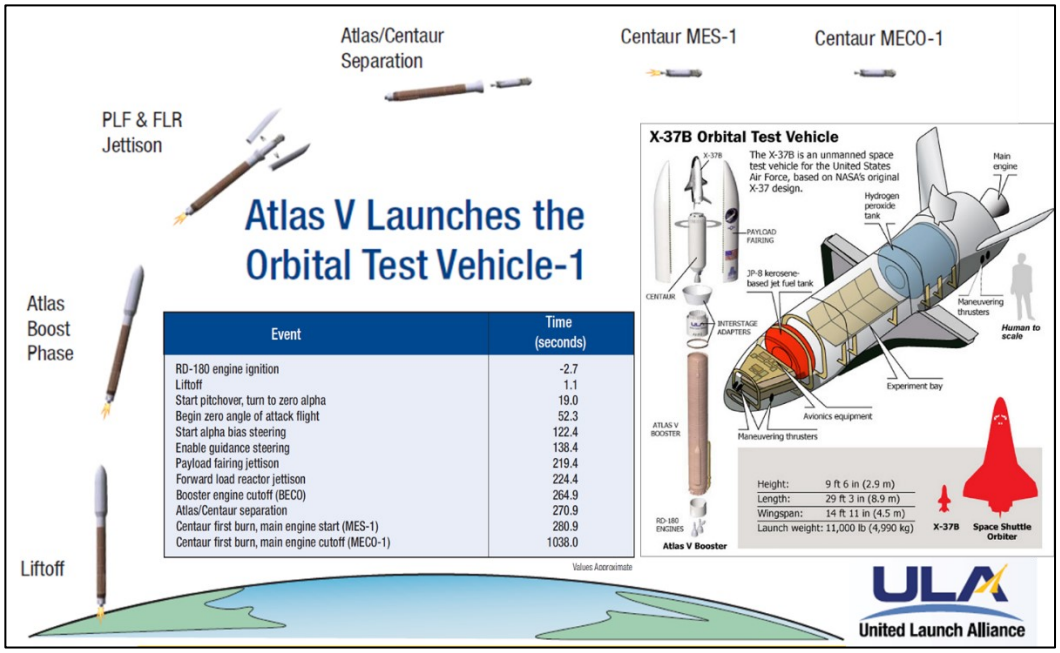


Figure 5-24 Atlas-V Launch Data – Launch Profile and Payload Configuration [ULA, 2010]

For this research, a data set was processed that was composed of infrasound data collected by 8 sensors located at the US Air Force Malabar Annex in Malabar, Fl. Table 5-5 below provides a tabular listing of the sensor data for the 8 sensors used in the AtlasV data collection. The table indicates the array name (MALB), associated element names, which type of infrasound micro barometer (sensors) were used for each element, as well as the coordinates for each sensor in latitude and longitude (Note: in this data set, the latitude and longitude coordinates are shown as identical for all sensors in the array. This is not typically the case as each sensor is usually spatially distributed at the site to provide channel-to-channel diversity to aid in

coherency assessment and source location. In this case, the lack of detailed ground truth data prevented the unique/correct identification of the individual sensor array elements.)

Table 5-5 Atlas Data – Sensor Locations

| Station Name | Element Name | Sensor Type | Latitude | Longitude |
|---|---|---|---|---|
| MALB | MALB1 | Chapparal 2.0 | 28.5835 | -80.5828 |
| | MALB2 | Chapparal 2.0 | 28.5835 | -80.5828 |
| | MALB3 | Chapparal 2.0 | 28.5835 | -80.5828 |
| | MALB4 | Chapparal 2.0 | 28.5835 | -80.5828 |
| | MALB5 | Chapparal 2.0 | 28.5835 | -80.5828 |
| | MALB6 | Chapparal 2.0 | 28.5835 | -80.5828 |
| | MALB7 | Chapparal 2.0 | 28.5835 | -80.5828 |
| | MALB8 | Chapparal 2.0 | 28.5835 | -80.5828 |

As before, processing of the Atlas V data begins by using the Inframonitor tool to process the array data and establish a baseline for the processed data results. The processing flow begins by pre-filtering the input data and then selecting the array of interest on which to search for detections. The adaptive F-statistic detection algorithm used by the Inframonitor tool typically provides detection results that give an indication of the major events within the data set. The results of the detection processing for the Atlas V data with the standard band-pass filtering method are shown below in Figure 5-25. In this case, 4 of the 8 available array elements were

selected for processing. Elements #5-8 were selected and are shown highlighted in red. The detection algorithm generated approximately 7 detection events, although none corresponded with the actual event, starting at approximately 23:57. The lack of a detection during the known event response indicates that the correlation-based detection criteria was not met in this region of the signal. A review of the computed F-statistic in Figure 5-26 below shows that no significant correlation of the input data was observed in the event region.

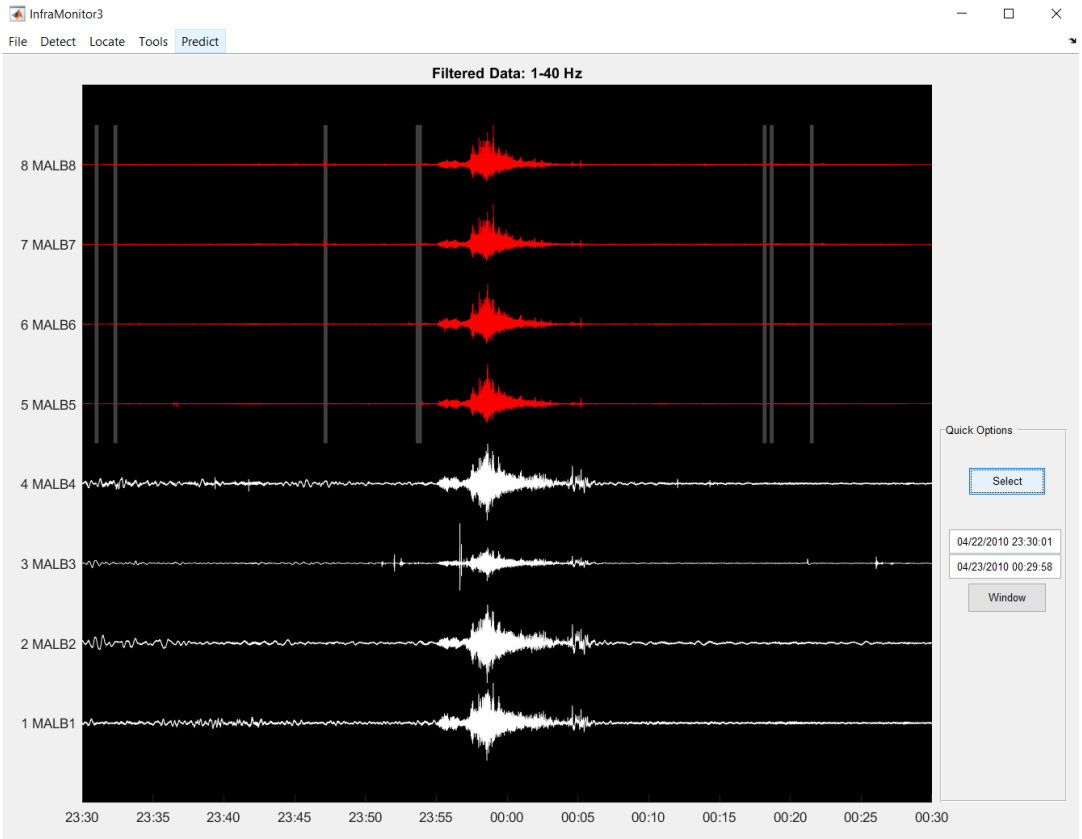


Figure 5-25 Atlas V Launch Data – Inframonitor Output with Standard Bandpass Filter Processing (1-40Hz) Showing Detections

For the Atlas V data set, when processed with the band-pass filter, the correlation coefficient is 0.38. In this example, the band-pass filter alone is not sufficient to isolate the signals of interest from the noise to allow the underlying channel-to-channel correlation to be identified by the detection algorithm. Unique observables in this case include the azimuth and phase velocity results in the 3rd and 4th panels. In each case the computed result is a flat line across the entire time window of the processed sample. This result is due to the use of constant latitude and longitude values for each sensor in the site description file used by the Inframonitor software (Reference Table 5-5.) Normally, the unique physical locations of each array sensor are used to process the back azimuth and the phase velocity for the signal. The constant value used in this case (due to the lack of a ground truth log) prevents the calculation of the azimuth and phase velocity parameters. The detection results for the ATLS sensor, Channel #1 are shown below in Figure 5-26.

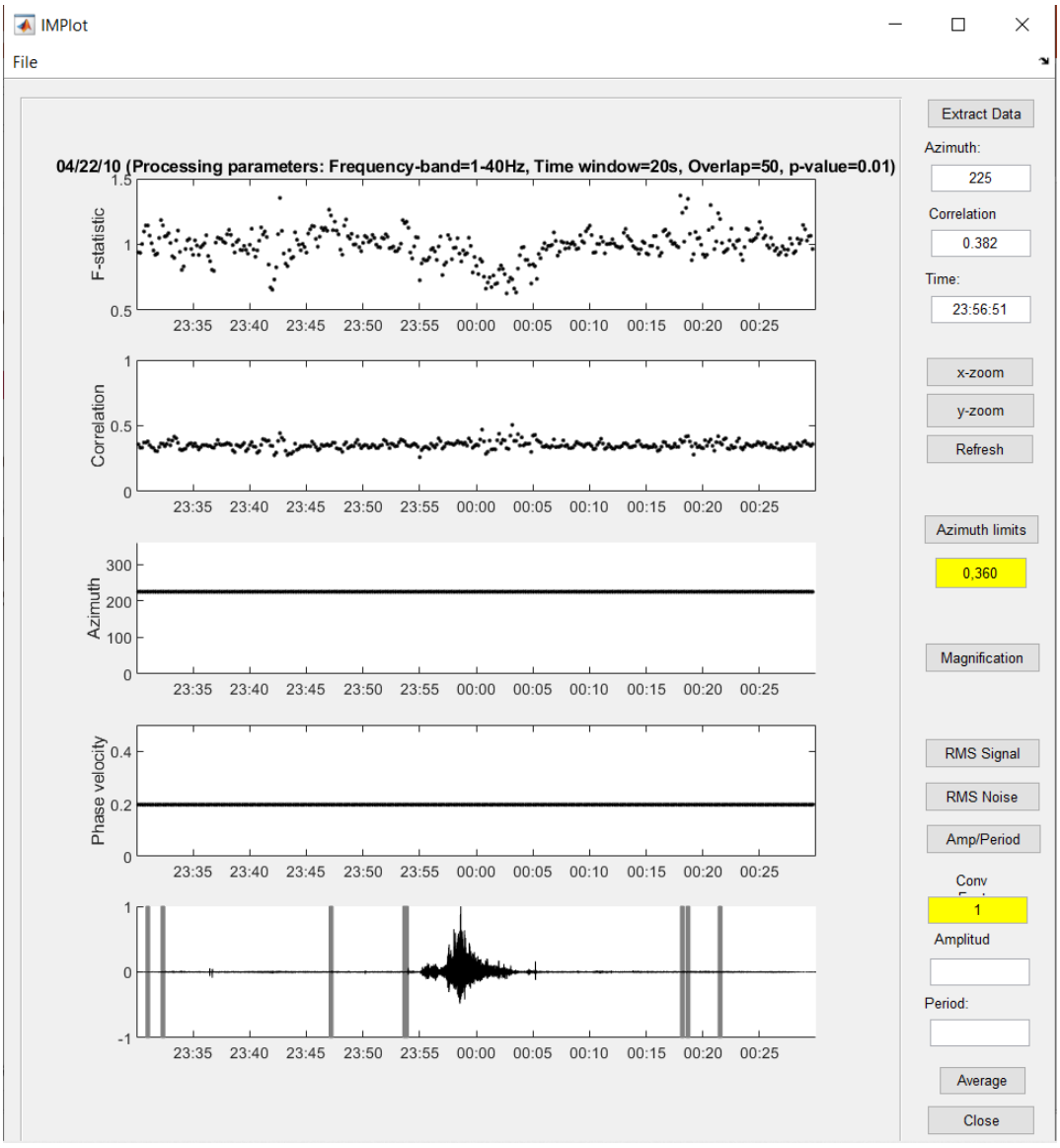


Figure 5-26 Atlas V Launch Data – IMPlot Output Showing Detections for Sensor DLI0 Channel #5 After Band-pass Filtering

The Atlas V data was also processed by using the Pure-State filter tool after the standard bandpass filter had been applied. See Figure 5-27 for the detection results.

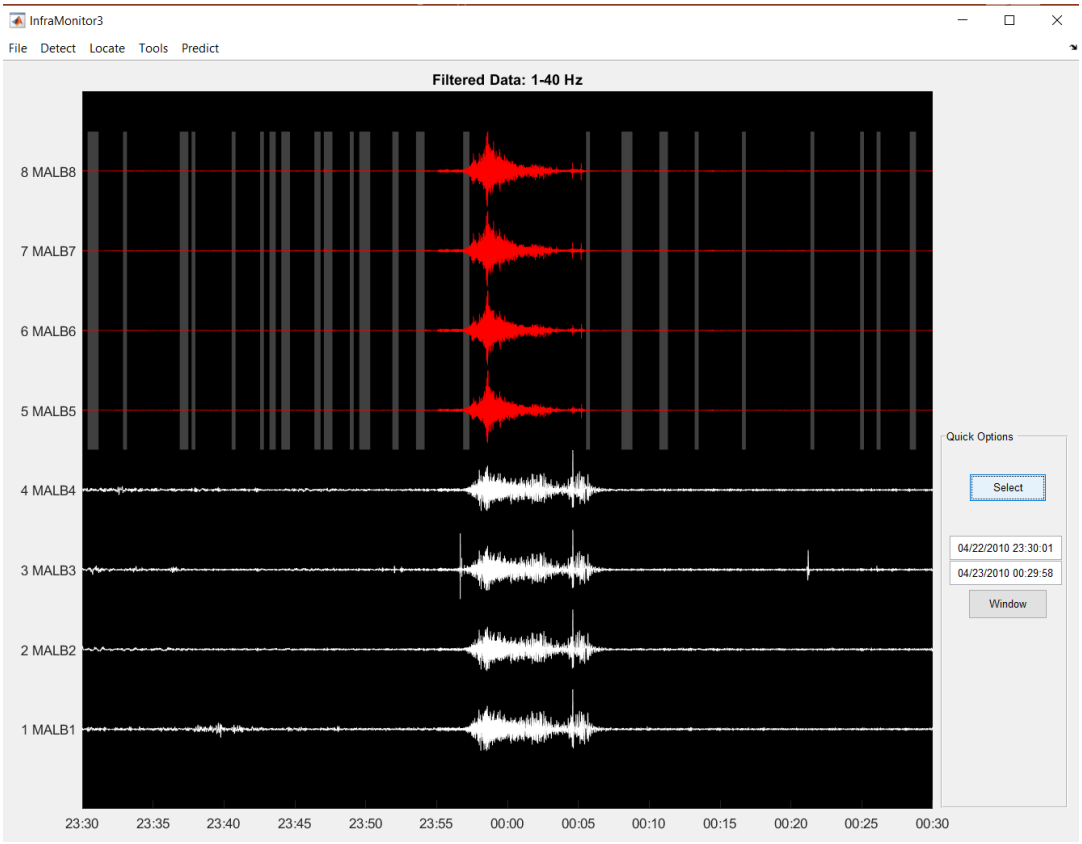


Figure 5-27 Atlas V Launch Data – Inframonitor Output with Pure-State Filter Processing Showing Detections

With the Pure-State filter, the correlation coefficient for the Atlas V data was improved relative to the bandpass filter alone. Specifically, the correlation improved from 0.38 to 0.47 as seen in Figure 5-28 below.

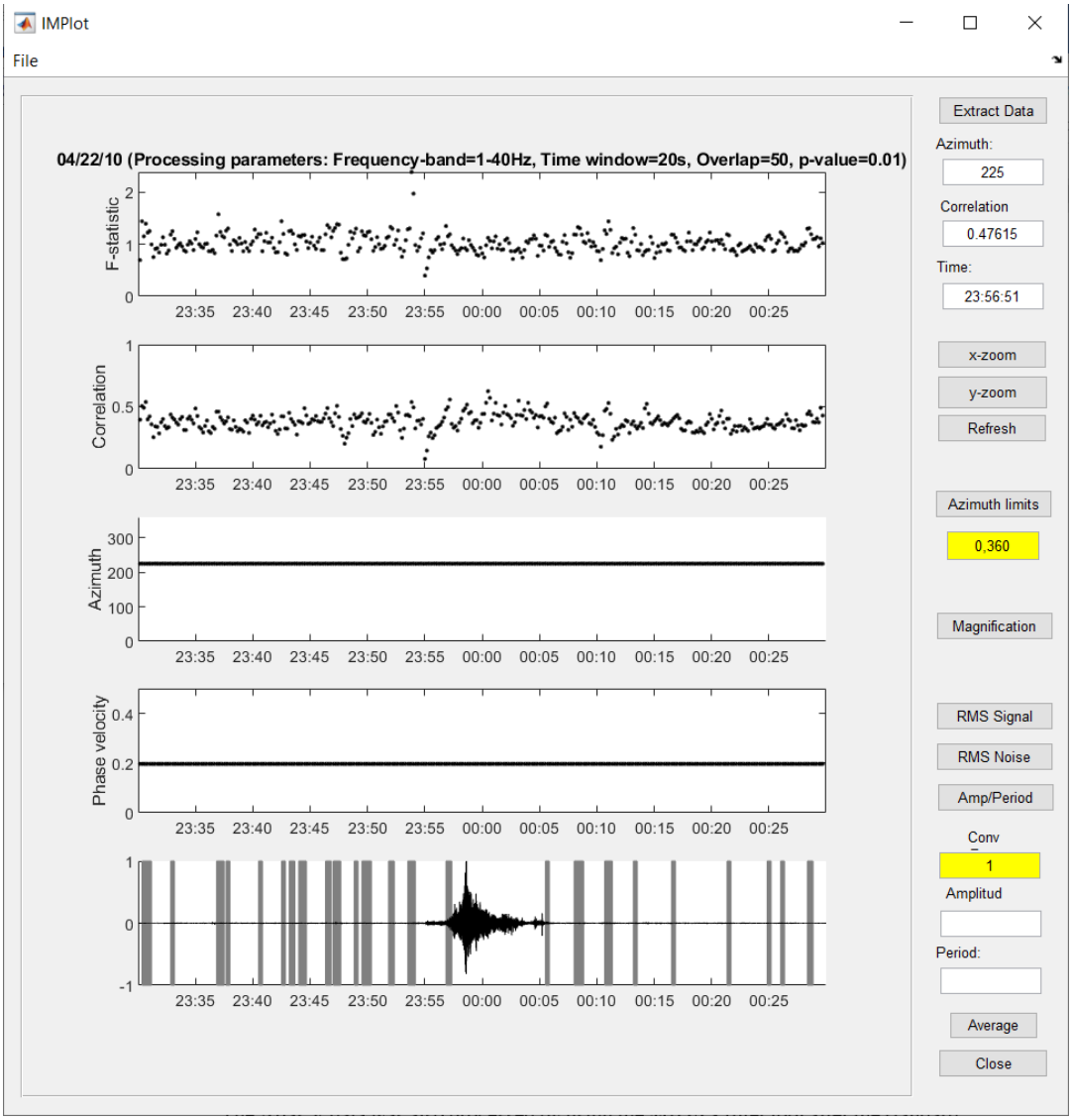


Figure 5-28 Atlas V Launch Data – IMPlot Output Showing Detections for Sensor DLI0 Channel #5 After Pure-State Filtering

The Atlas V data was also processed by using the MIDAS filter tool after the standard bandpass filter had been applied. See Figure 5-29 below for the detection results.

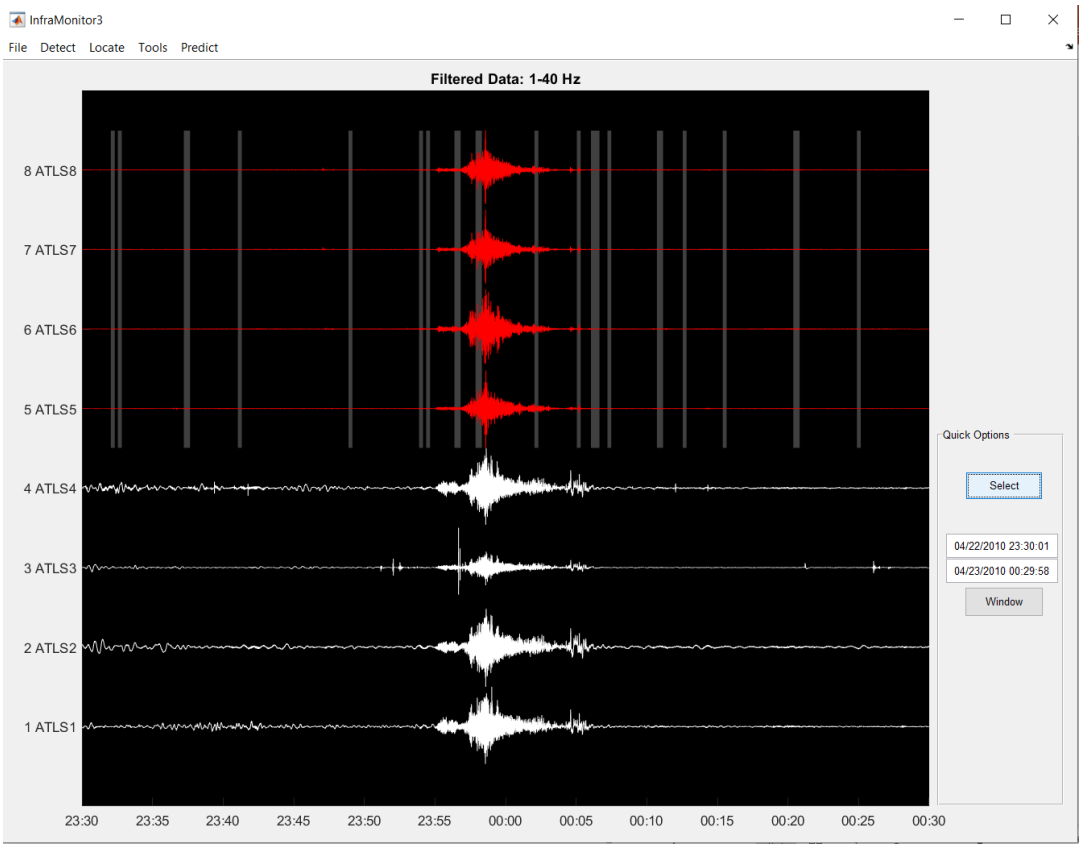


Figure 5-29 Atlas V Launch Data – Inframonitor Output with MIDAS Filter Processing Showing Detections

With the MIDAS filter, the correlation coefficient for the Atlas V data was improved relative to the bandpass filter and the Pure State Filter. Specifically, the correlation improved from 0.38 with the Band-pass filter and 0.47 with the Pure State filter to 0.53 with the MIDAS filter as seen in Figure 5-28 below.

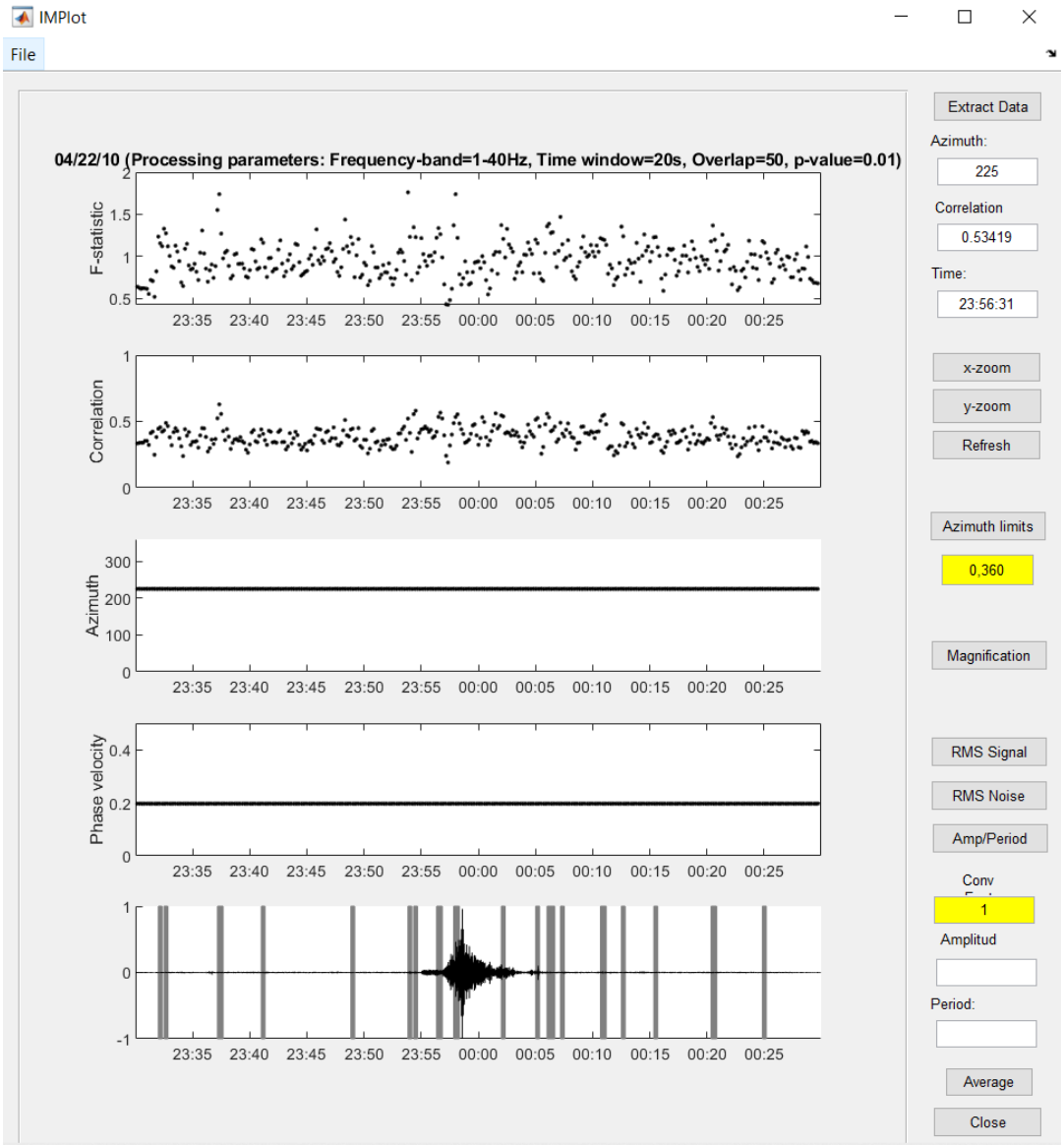


Figure 5-30 Atlas V Launch Data – IMPlot Output Showing Detections for Sensor DLI0 Channel #5 After MIDAS Filtering

## 5.4 Experimental Data Summary

In an attempt to provide a reasonable cross-section of data sources and types, this experiment evaluated data from a US Coast Guard Boat, a bolide, an Atlas V rocket launch and high-yield explosive detonations. The input data was processed with the InfraMonitor signal processing tool and the resulting detections were selected for further processing. In order to tailor the processing to the particular dataset, the InfraMonitor tool provides a set of "preference" settings that define how the detection algorithm will function. There are 4 primary parameters that the user can configure for the detection algorithm [Arrowsmith, 2012]:

1) Time Window: The processing time window should be set to the approximate signal durations of interest.

2) Overlap: The overlap between processing time windows. An overlap of 50% is recommended as an appropriate choice for most applications.

3) Adaptive Window: The adaptive window length must be set long enough to obtain a sufficient sample distribution, but short enough to account for temporal variations in ambient noise. We have found that an adaptive window length of 1 hour is appropriate for typical infrasound data.

4) P-statistic: The p-value affects the numbers and signal-to-noise ratios of detections obtained.

Table 5-6 below shows the summary of InfraMonitor parameters and processing results for each filter type.

Table 5-6 InfraMonitor Analysis Parameters and Output Statistics vs. Filter Type

| | Inframonitor Preferences | | | | | | | |
|---|---|---|---|---|---|---|---|---|
| Data Description | Time Window | Overlap | Adaptive Window | p-statistic | filter BW | F-statistic | azimuth | correlation |
| Band-pass Filter Results | | | | | | | | |
| USCG KW Boat Data | 20s | 50 | 3600 | 0.01 | 1-200 | 1.75 | 225 | 0.21 |
| UTTR Data | 20s | 50 | 3600 | 0.01 | 1-5 | 26 | 324.93 | 0.93 |
| Acapulco Bolide Data | 70s | 50 | 3600 | 0.01 | 1-4 | 1.6 | 188.39 | 0.35 |
| Atlas Launch Data | 20s | 50 | 3600 | 0.01 | 1-40 | 1.2 | 225 | 0.38 |
| Pure-State Results | | | | | | | | |
| USCG KW Boat Data | 20s | 50 | 3600 | 0.01 | 1-200 | 2.5 | 228.1 | 0.42 |
| UTTR Data | 20s | 50 | 3600 | 0.01 | 1-5 | 39 | 324.93 | 0.95 |
| Acapulco Bolide Data | 70s | 50 | 3600 | 0.01 | 1-4 | 1 | 279.68 | 0.61 |
| Atlas Launch Data | 20s | 50 | 3600 | 0.01 | 1-40 | 2 | 225 | 0.48 |
| MIDAS Results | | | | | | | | |
| USCG KW Boat Data | 20s | 50 | 3600 | 0.01 | 1-200 | 1.25 | 284.89 | 0.47 |
| UTTR Data | 20s | 50 | 3600 | 0.01 | 1-5 | 16.5 | 324.46 | 0.97 |
| Acapulco Bolide Data | 70s | 50 | 3600 | 0.01 | 1-4 | 2.5 | 316.02 | 0.65 |
| Atlas Launch Data | 20s | 50 | 3600 | 0.01 | 1-40 | 1.5 | 225 | 0.53 |

In all cases the Pure State filter improved the correlation coefficient metric over a standard band-pass filter. And in all cases the MIDAS filter improved the metric over the Pure State Filter. See Figure 5-31 below for the comparison of filter type. The only case where the MIDAS filter did not significantly exceed the performance of the Pure State filter was for the explosive detonation data from the UTTR data set. This is likely due to the impulsive nature of the data. Explosions are very high energy, short-duration events that produce signatures with high SNR and sharp, impulsive response signatures. The benefits of the MIDAS filter (isolating spectra relative to the surrounding noise) are minimized with these types of data.

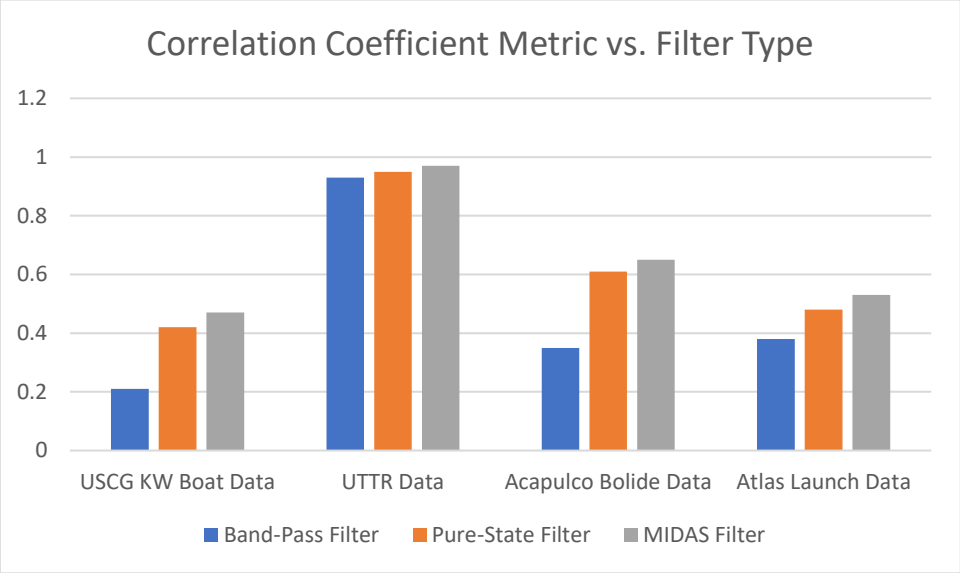


Figure 5-31 InfraMonitor Correlation Coefficient vs. Filter Type

## 5.5 Multicriteria Decision Analysis (MCDA) and Optimization

### 5.5.1 MCDA Overview

The practice of Multicriteria Decision Analysis (or Decision Making) is generally thought of as being separated into two key areas. Multi-attribute decision making considers the case where a fixed number of solutions exist and the decision maker must choose between one of them. With Multi-objective programming (or Multi-objective Linear Programming-MOLP) the decision maker must consider the optimization of some number of objectives in the presence of some number of constraints. In the classical presentation of MOLP problems the problem is represented mathematically as:

$$\begin{aligned} \text{Maximize:} \quad & z_1 = \mathbf{c}^1\mathbf{x} \\ & z_2 = \mathbf{c}^2\mathbf{x} \\ & \dots \\ & z_n = \mathbf{c}^k\mathbf{x} \end{aligned} \tag{2}$$

$$\begin{aligned} \text{subject to:} \quad & \mathbf{A}\mathbf{x} \leq b \\ & \mathbf{x} \geq 0, \end{aligned} \tag{3}$$

where $\mathbf{c}^k$ denotes one of the k-th objectives of the decision maker. The more common and compact vector notation consolidates the objective function coefficients, **c**, into the matric **C** and the objective values in the vector **z** as follows:

$$C = \begin{bmatrix} c^1 \\ c^2 \\ \vdots \\ c^k \end{bmatrix}, \ and \ z = \begin{bmatrix} z_1 \\ z_2 \\ \vdots \\ z_n \end{bmatrix} \tag{4}$$

which allows the optimization problem to be written as:

$$\text{maximize:} \quad \mathbf{z} = \mathbf{Cx} \tag{5}$$

$$\text{subject to:} \quad \mathbf{Ax} \leq \mathbf{b} \tag{6}$$

$$\mathbf{x} \geq 0$$

### 5.5.2 Optimization with the MIDAS Filter

Since the origins of the field of MCDA, there have been dozens of tools developed to aid decision makers in evaluating often conflicting objectives and system constraints with often uncertain input data. An evaluation of the MIDAS filter implementation with respect to optimization looks to address opportunities to reach optimization of the processing of signal of interest in terms of standard metrics such as the signal-to-noise ratio of the test signal. The various user-configurable software variables available to the analyst from within the MIDAS filter provide a means to parameterize the signal processing. For example, the prominence parameter allows the analyst to determine how the MIDAS filter responds to spectra within the input signal. As the prominence parameter is increased, a given frequency must "stand-out" more prominently within the power spectrum relative to its neighbors. Tailoring this parameter to a particular input signal can be useful in isolating signals of interest relative to the channel noise as well as separating desired signals relative to others. In addition to the prominence parameter, the MIDAS filter allows the analyst to adjust the sub-bandwidth setting. This parameter is used to determine how much spectral content is included with the "selected" signal of interest when filtered. This parameter might be increased when the input signals do not contain pure tones. Narrowing this parameter excludes additional signal content until only a discrete frequency of interest is isolated for filtering. Table 5-7 below lists the data gathered

during this experiment to develop the response surface and identify the optimum prominence and sub-bandwidth setting for the given input data set.

Table 5-7 Response Surface Data: Prominence and sub-bandwidth Values Used to Identify Maximum Input Signal SNR Improvement with MIDAS Filtering

| Improvement in SNR of Input Signal with MIDAS Filter | | | | | | |
|---|---|---|---|---|---|---|
| | | Prominence | | | | |
| | | 5 | 10 | 15 | 20 | 25 |
| Sub-bandwidth | 1 | 16.67 | 16.67 | 16.67 | 16.67 | 17.76 |
| | 2 | 13.47 | 13.47 | 13.47 | 13.47 | 14.82 |
| | 3 | 11.86 | 11.86 | 11.86 | 11.86 | 13.66 |
| | 4 | 9.57 | 9.57 | 9.57 | 9.57 | 11.15 |
| | 5 | 8.14 | 8.14 | 8.14 | 8.14 | 9.86 |
| | 6 | 7.38 | 7.38 | 7.38 | 7.38 | 9.26 |
| | 7 | 6.78 | 6.78 | 6.78 | 6.78 | 8.45 |
| | 8 | 6.21 | 6.21 | 6.21 | 6.21 | 7.78 |
| | 9 | 5.52 | 5.52 | 5.52 | 5.52 | 7.29 |
| | 10 | 5.09 | 5.09 | 5.09 | 5.09 | 6.86 |

Figure 5-32 below shows the response surface for the MIDAS filter. This surface represents the response of the MIDAS filter for a given input data set. Other data sets could have a different response surface depending on the spectral content of the input signal.

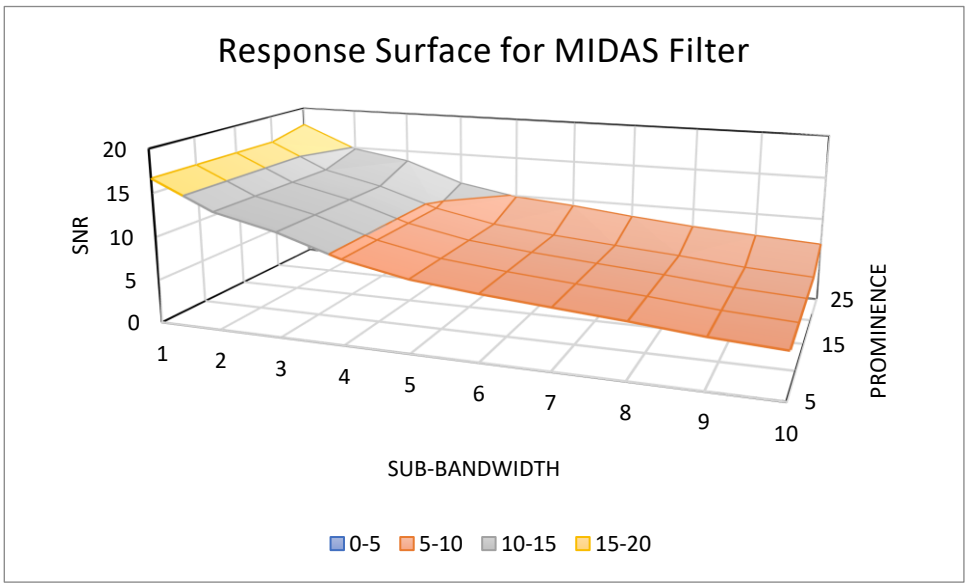


Figure 5-32 Response Surface for MIDAS Filter with Prominence (5-25) and Sub-bandwidth (1-10) Contrasted for Impact on Filtered Data SNR

As the figure above shows, there is an increase in the SNR result as the sub-bandwidth is decreased. This is due to the smaller amount of signal information being passed through the filter as the sub-bandwidth gets smaller (narrower). There is also a small increase in the SNR as the prominence is increased. This is due to the smaller number of "spikes" from the PSD plot being included in the filter (reference Figure 4-1). As the prominence is increased, fewer and fewer frequencies are identified for filtering, with all remaining content being rejected by the filter as noise. For the particular data set evaluated in this example, there is very little dependence between the prominence and the sub-bandwidth parameters. This is due to the structure of the power spectrum for the input signal. In this example, all of the signals of interest had fairly similar peak amplitudes. As a result, the prominence parameter passed all of

the signals of interest across the range evaluated until the final two settings (20 & 25 dB). An input signal with a wider variety of signal power, or a finer granularity on the prominence parameter would provide increased slope on the prominence axis. With the response surface optimization tool, the analyst typically attempts to move the operating point of the system to the highest (or lowest for a minimization problem) point on the surface. This point would define an optimum set of test parameters for processing the given input data set. In this example, the analyst would choose to select a small (narrow) sub-bandwidth setting and a large prominence setting. A choice of (1, 25) for sub-bandwidth and prominence respectively would provide an optimum filter result (maximum improvement of signal-to-noise ratio) for the data set used in this example.

# 6 Extensions to the MIDAS Filter Currently in Development

## 6.1 MIDAS Filter Extensions

To further the capability of the MIDAS filter, on-going research looks to extend the applicability of the filter to a more diverse set of signal processing problems. Image and speech analysis are common applications where the MIDAS filter may find use. While these alternative applications of the MIDAS filter necessarily require different analytical solutions versus the primary algorithm discussed in this dissertation, these extensions (and others) move the MIDAS filter from a single-focus analytical solution to more of a signal processing toolbox. It is therefore the desire of the research team to continue to develop the MIDAS filter to support a variety of needs in the signal processing community.

### 6.1.1 Image Processing Extension

In the image processing arena, there exists a wide range of analysis tools and methods designed to improve image quality. Many tools work to address errors in the so-

called entrance “pupil-plane” of an imaging system and deal with errors such as phase aberrations due to atmospheric turbulence. Many other tools deal with errors introduced by the very process of recording the image. The analog-to-digital sampling process can produce errors such as sampling noise and quantization error [Teo, 1994]. This particular extension of the MIDAS filter aims to work in concert with existing tools and serve as a pre-processor. In this capacity, the MIDAS filter would be used to reduce or remove sensor or channel-induced errors ascribable to the detector plane.

For this research, 10 modified realizations of an original test image were produced, each having a unique, random additive gaussian noise overlay applied. This would be analogous to a sensor (camera) collecting multiple samples of the same scene with the random noise representing errors added to the data by the sensor and/or the data acquisition system. If we assume that the scene does not significantly change from one capture event to the next, then we can argue that the pixels that vary across time are noise and those that are persistent are valid image data.

The MIDAS filter works by interrogating each image on a pixel-wise basis. Each image in the ensemble is processed in succession in a “sliding-window” sense, while the filter algorithm develops a n-image pixel intensity history. In this context, the image “intensity” is the gray-scale mapping of the pixel. This persistence function tends to reject pixel values that are varying from the ensemble mean. The length of the sliding window (number of images) is user selectable to accommodate dynamic

scenes. Depending on the particular analysis, the reference image may be a pristine, un-noised image, or the reference image may be the captured image that serves as the starting point for the denoising post processing. The peak signal-to-noise ratio (pSNR) is a well-known image quality metric that considers the variation between the reference and test images in a mean-squared sense. The pSNR is defined as:

$$pSNR = 10log_{10}\left(\frac{peakval^2}{MSE}\right), \tag{7}$$

where the peakval is the maximum pixel intensity in the image and MSE is the mean squared error between the test and reference images.

Given two images (x,y) with pixel size (m x n), the mean squared error, MSE is defined as:

$$MSE(x,y) = \frac{1}{mn}\sum_{i=1}^{m}\sum_{j=1}^{n}\left(x_{ij} - y_{ij}\right)^2 \tag{8}$$

Figure 6-1 below shows a typical progression of noise reduction with successive image realizations. (Note the image number at the left of the title and the pSNR at the right of title)

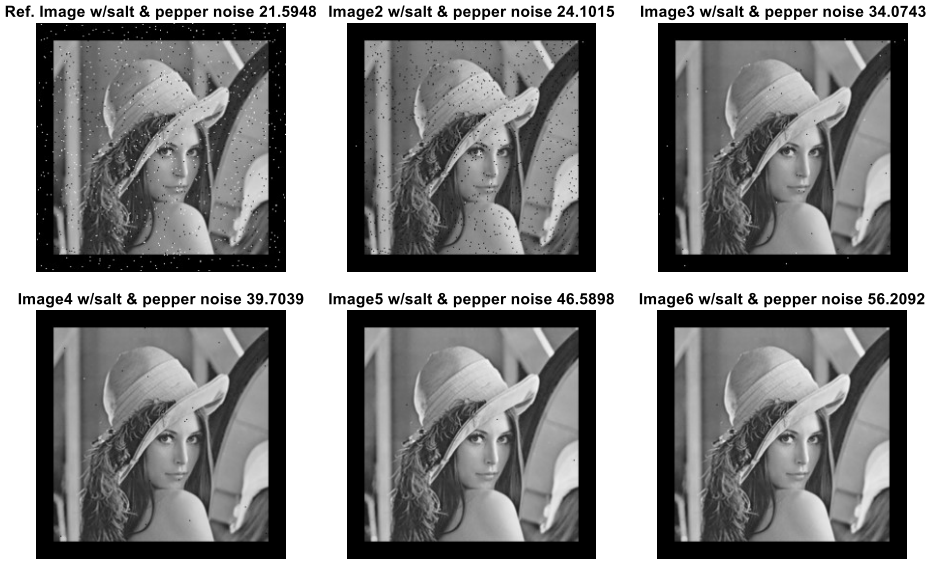


Figure 6-1 Image Noise Reduction With Successive Image Realizations Using the MIDAS Filter Image Processing Extension

The successive image realizations shown above in Figure 6-1 reflect the progressive improvement in image quality due to the filtering operation. Each new image includes less of the salt-and-pepper noise. The pSNR for the reference image was 21.59 dB and by the third iteration the pSNR had been improved to 34.07 dB. After all six iterations of the experiment, the pSNR had been increased to 56.21 dB.

Figure 6-2 below shows a typical rate of pSNR improvement as the number of additional realizations is increased.

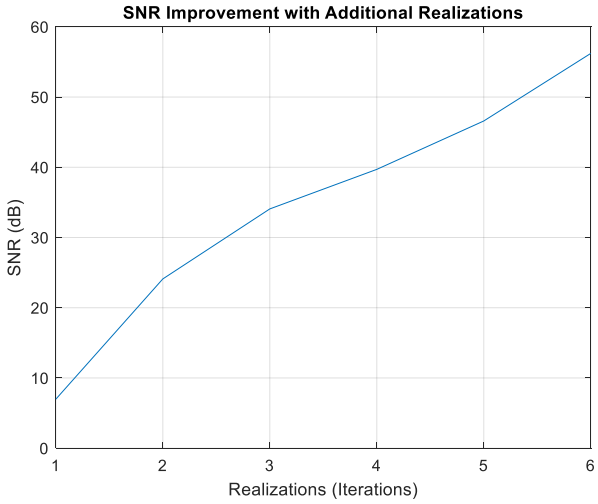


Figure 6-2 Increased Image SNR with Additional Realizations

Similar to the Signal-to-Noise Ratio metric, the Structural Similarity Index Measure (SSIM) is an image quality figure of merit that is based on the subjective assessment of the test image relative to a distortion free reference image. The SSIM metric has the dual benefit of not only a quantitative score in the global value metric provided, but also a qualitative measure in the form of the quality map of the image. This quality map identifies localized structure differences relative to the reference image.

The structural similarity index measure is the summation of a luminance, contrast and structural term and is defined as [Palubinskis][Wang][Sheikh]:

$$SSIM(x,y) = [l(x,y)^{\alpha}] \cdot \left[c(x,y)^{\beta}\right] \cdot [s(x,y)^{\gamma}], \tag{9}$$

where,

$$l(x,y) = \frac{2\mu_x\mu_y + C_1}{\mu_x^2 + \mu_y^2 + C_1} \tag{10}$$

$$c(x,y) = \frac{2\sigma_x\sigma_y + C_2}{\sigma_x^2 + \sigma_y^2 + C_2} \tag{11}$$

$$s(x,y) = \frac{\sigma_{xy} + C_3}{\sigma_x\sigma_y + C_3} \tag{12}$$

which simplifies to:

$$SSIM(x,y) = \frac{(2\mu_x\mu_y + C_1)(2\sigma_{xy} + C_2)}{(\mu_x^2 + \mu_y^2 + C_1)(\sigma_x^2 + \sigma_y^2 + C_2)} \tag{13}$$

Given images (x,y) in the above expressions: $\mu_x$, $\mu_y$, $\sigma_x$, $\sigma_y$ represent the image means and standard deviations while $\sigma_{xy}$ represents the cross-covariance for the images. The constants $C_1$, $C_2$, $C_3$ are present to prevent a zero denominator, and were set to 1 for this experiment.

For evaluating the MIDAS filter using the SSIM metric, a similar approach was used to that of the pSNR metric above. A series of noisy images were created and the SSIM metric was used to evaluate the progressive improvement of the filter as successive realizations of the image were processed with the MIDAS filter. Figure 6-3 below shows the SSIM score and quality image map for several of the realizations (Image number at the left of the image title and pSNR for the upper row, and SSIM score at the right of the title for the lower row).

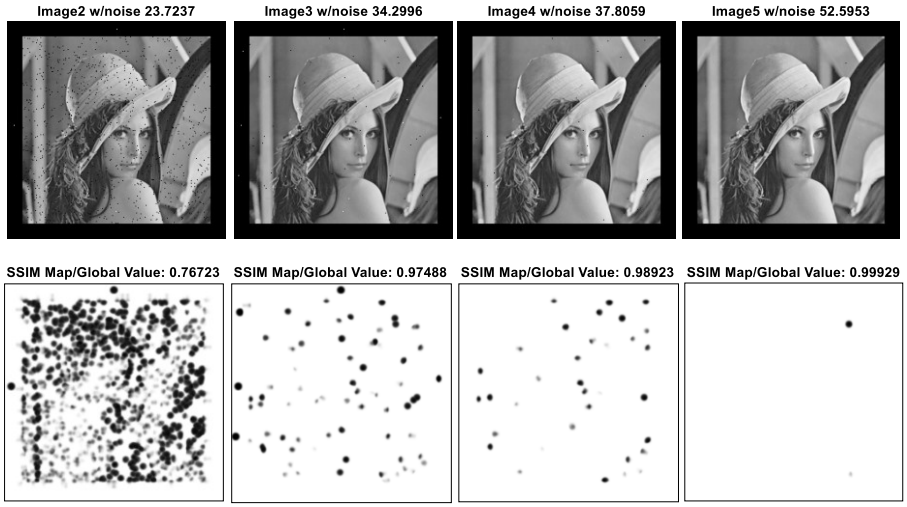


Figure 6-3 SSIM Assessment of Noise Reduction with Additional Realizations of Image

As Figure 6-3 indicates, increasing realizations of the test image reduces the residual noise in the image. In this example, the final image SNR was 52.59 dB. In conjunction with the pSNR metric, the quality map at the bottom of Figure 6-3 shows continuous improvement with additional realizations. In this case, the final quality score achieved from the SSIM metric for the global map was 0.99929, with 1.0 being the best value.

As an alternative to the pSNR and the SSIM, the Perception Based Image Quality Evaluator (PIQE) metric is an image quality assessment tool that is purely based on the input image [Venkatanath]. No reference image is needed for this metric. The PIQE metric computes statistics based on localized evaluations of errors within the test image. Figure 6-4 below shows the progression of noise reduction in the test

images with additional realizations using the PIQE metric. As with the examples above, the pSNR score for each filtered image is shown in the image title, while the PIQE score for each image is plotted below the images.

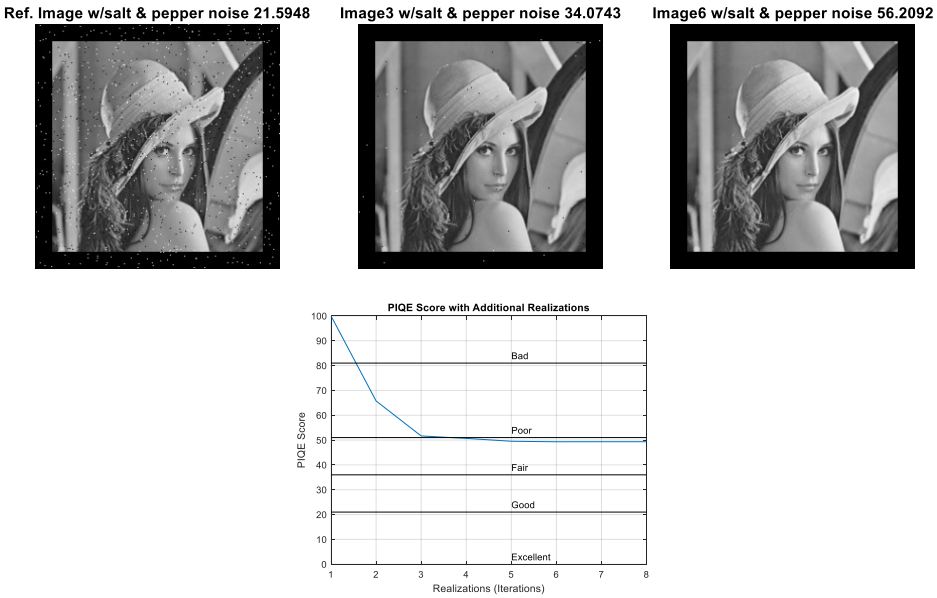


Figure 6-4 PIQE Assessment of Noise Reduction with Additional Realizations of Image

The PIQE metric assigns the image quality score based on preset threshold values. Lower scores for this metric indicate better filter results, with scores in the mid-ranges being common. Very high contrast images and/or images having low spatial variance generally achieve lower (better) PIQE scores.

### 6.1.2 Speech Processing Extension

Another common application of signal processing is for speech analysis. Various tools and methods exist for identifying key phrases embedded in speech patterns, isolating speech in the presence of noisy backgrounds, or even speech recognition analysis. The MIDAS filter has also been extended to include various aspects of speech analysis. Initially, the tool has been applied to the problem of isolating an echo or delayed signal within a speech pattern and attempt to correct it. This is a signal processing problem that might present itself when someone makes a speech inside an auditorium and the acoustics of the room are such that an echo is presented at the location of the microphone. This might come from a reflection off of a wall or the ceiling. In either case, the recorded sound information will include a composite of the original, intended signal superimposed with the echo, which is a copy of the original signal delayed in time by some small amount. The Cepstrum is a convenient tool for identifying echoes in speech or other signals of interest, and has been applied by the MIDAS filter to do the same.

In 1963 Bogert, Healy and Tukey published their seminal paper called “The Quefrency Analysis on Time Series for Echoes: Cepstrum, Pseudoautocovariance, Cross-Cepstrum and Saphe Cracking” [Bogert, et. al., 1963]. A primary observation of this work was that the logarithm of the power spectrum of a signal containing an echo also had a periodic component due to that echo. And the power spectrum of this logarithm of the original power spectrum will have a peak at the frequency of the

echo [Oppenheim]. The term “Cepstrum” is a manipulation of the word Spectrum, to acknowledge the abnormal operation of time and frequency space operations that are in play during cepstral analysis. The complex cepstrum of a signal is defined as the inverse Fourier transform of the logarithm of the magnitude of the Fourier transform of a sequence:

$$c_x[n] = \frac{1}{2\pi}\int_{-\pi}^{\pi} log\left|X(e^{j\omega})\right| e^{j\omega n} d\omega \tag{14}$$

where the Fourier transform of x(n) is given by,

$$\hat{X}\left(e^{j\omega}\right) = log\left|X(e^{j\omega})\right| + j\angle X(e^{j\omega}) \tag{15}$$

Additionally, for the real-valued input sequence, x[n], $\log\left|X(e^{j\omega})\right|$ is an even function and $j\angle X(e^{j\omega})$ is an odd function. Therefore, the inverse transform of $\hat{X}(e^{j\omega})$ is a real-valued function. Since $c_x[n]$ is based only on the Fourier Transform magnitude, it is not invertable which means that the original signal, x[n] cannot be recovered from the real cepstrum, $c_x[n]$.

To provide an example of the echo/delay removal capability of the current MIDAS filter extension, a sample speech signal was used. In this case a speech recording was imported that included a man reciting a portion of the children's rhyme, "Mary had a little lamb." To simulate an echo in the recoding, the sound file was augmented with a delayed version of the speech. In this example the echo was set to a 0.25 second delay. This might simulate an echo from a wall or other object in the room in which the speaker is standing while the sound was being recorded. Additionally, the echo is reduced in amplitude to simulate the attenuation that a reflected echo would undergo. Figure 6-5 below shows the time domain response of the original signal along with an overlay of the delayed and attenuated echo signal. The lower half of the plot shows the original and echo signals combined. This composite signal is what the microphone might pick up and what might subsequently be recorded. This distorted signal would require processing to remove the echo from the original signal and return the speech to its intended level of quality.

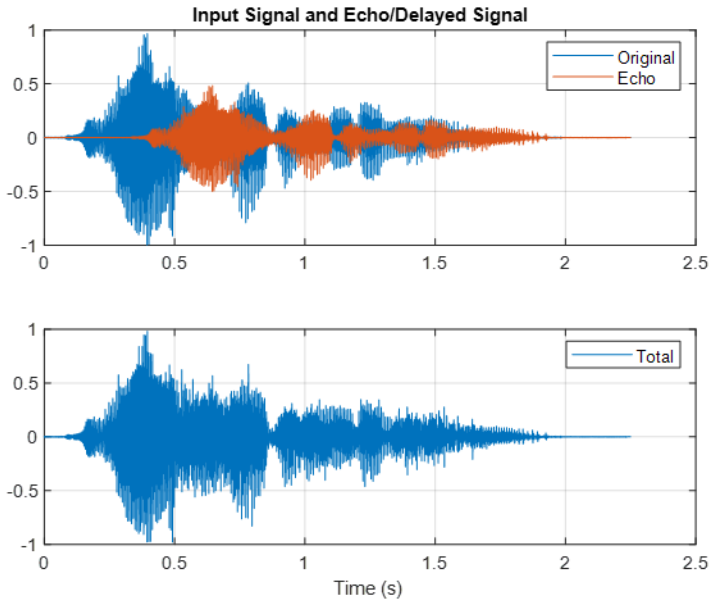


Figure 6-5 Speech Processing Example- Original and Delayed Signals

Figure 6-6 below shows the computed cepstrum for the composite speech signal (original + echo). The cepstral analysis identifies the location of the start of the delayed signal which is represented with a spike at 0.25 seconds. Note the plot shown in Figure 6-6 shows two sets of duplicate responses. Since the cepstrum is a Fourier process, the result contains an image on the opposite side of the zero point that represents the negative frequencies.

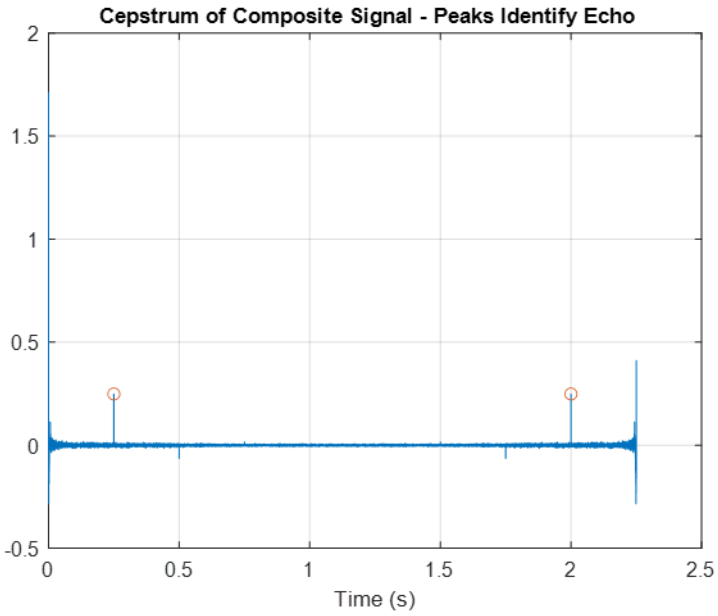


Figure 6-6 Cepstrum of Composite Speech Signal

Once the location of the echo is determined, the cepstrum data (cepstra) can be edited (liftered) to remove the undesired content. For this implementation, an IIR filter using the known delay was used to remove the echo from the input signal. The filter had the general form:

$$y(n) = w(n) + \alpha w(n - \Delta), \tag{16}$$

$$where\ the\ delay, \Delta = 0.25\ seconds\ and\ \alpha\ is\ the\ attenuation$$

Figure 6-7 below shows the original signal (top), the original + echo (2nd from top), the composite signal (3rd from top) and the MIDAS filtered signal (bottom). In this

case the MIDAS filter was able to remove the echo/delayed signal from the speech and restore the original signal quality.

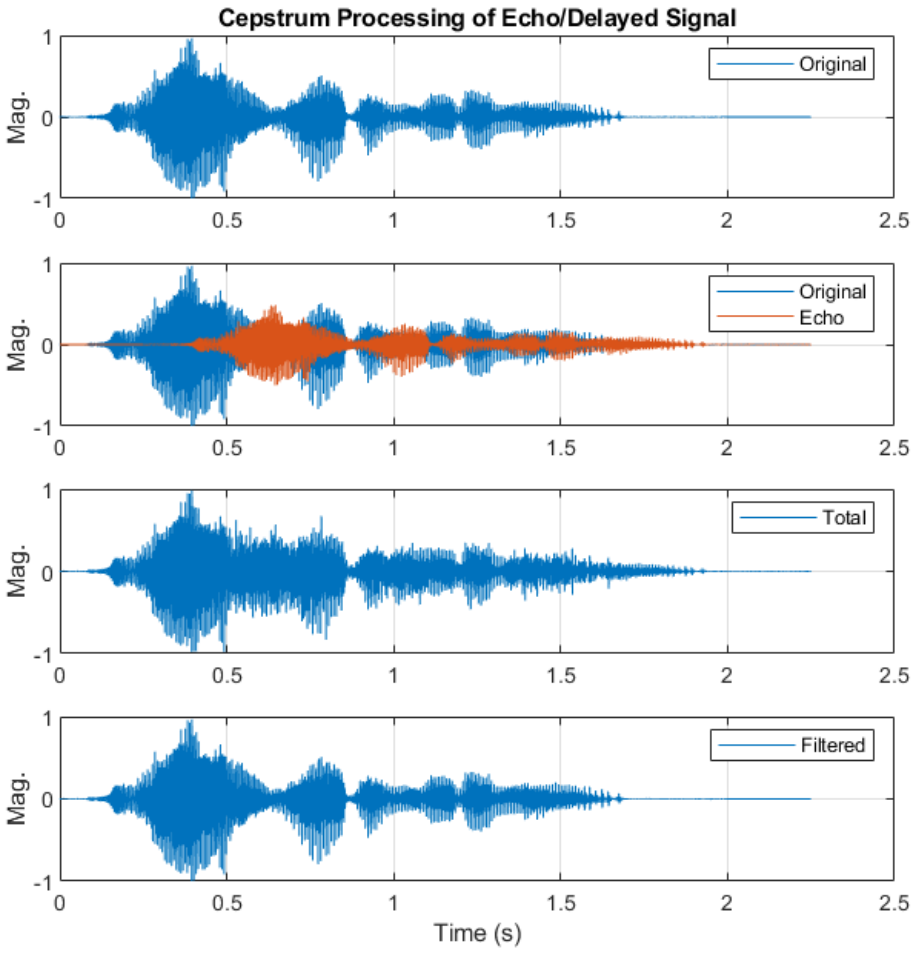


Figure 6-7 Cepstral Speech Processing Example Showing Original, Original+Echo, Composite and MIDAS-filtered Result

# 7 Conclusions

The MIDAS filter has been developed to provide additional flexibility to the signal analyst when looking to exploit complex data signals. The MIDAS filter emphasizes the isolation of desired spectra in the frequency domain through the use of targeted sub-band selection and spectral weighting. Unique aspects of the MIDAS filter include the data-adaptive selection of dominant spectra as well as the iterative adjustment of the input signal as the sub-banding is adjusted by the user. This functionality has been incorporated into a MATLAB GUI for ease of distribution and use by practitioners.

The MIDAS filter has been shown to effectively identify and isolate spectra embedded within signals having very low SNR. In fact, if the user has a-priori knowledge of the target signal frequency of interest, the MIDAS filter can effectively isolate it relative to adjacent frequencies.

The InfraMonitor software tool was used to provide a standardized point of reference to compare the MIDAS filter to other, canonical filter types including the Pure State Filter and a standard band-pass filter. A series of test signals collected from a variety of infrasound sensors across the United States were processed with InfraMonitor. The adaptive F-statistic detection algorithm was used to identify detections within

each sensor channel and certain channels were selected for detection processing. The coherence coefficient (which is a measure of the phase relationship between each of the channels) is highly sensitive to the SNR of the input data. As such, improvement by filtering should yield an improved coherence coefficient metric. The MIDAS filter performed better than the Pure-state filter and the band-pass filter for all test signals with the exception of the explosive detonations. This is likely due to the nature of the data being extremely impulsive and typically having a high SNR without the need for any pre-filtering. This pre-existing "goodness" in the test signal minimizes the inherent benefit/capability of the MIDAS filter.

Two in-process extensions of the MIDAS filter were discussed. The desire to expand the capability of the MIDAS filter into additional areas of signal processing has lead the research team to investigate additional possibilities for the filter. Currently speech analysis and image processing extensions are being developed. In the speech analysis extension, the use of cepstral analysis was shown as a means to identify and filter out a delayed echo from a speech pattern. For the image processing extension, the use of a sliding window-based persistence function was shown to be effective in de-noising a sample image. The use of several standard image quality metrics provides a qualitative and quantitative means by which to assess the filter efficacy and image improvement.

# 8 Future Work

The MIDAS filter has been developed in support of the research described herein. During the process of developing the tool, studying industry needs and current practices and collaborating with signal processing practitioners, there have been several possible enhancements that have been identified. Continued research to extend the capability of the MIDAS filter can be expected to further increase its utility and value to its users. Some of the identified enhancements that should be pursued are presented here:

1) Variable sub-band filter weights: The current version of the MIDAS filter allows the analyst to select attenuation weights for the in-band and out-of-band filter masks that get applied after the sub-band selection stage. An identified enhancement would allow the filter to accommodate variable, unique weights for the selected sub-bands. This would allow, for example, the user to custom "tune" the attenuation based on the signature of the input signal with some frequencies getting more attenuation than others.
2) Variable sub-band bandwidths: The current version of the MIDAS filter allows the analyst to select which frequencies to apply the in-band weighting function to. By default, all selected frequencies are filtered with the same sub-bandwidth. Additionally, all other frequencies are attenuated

by the out-of-band weighting function. An enhancement would allow the user to individually vary the unique bandwidth of each selected sub-band.

3) "Chirp"-processing: Certain types of noise signatures (possibly wind) may manifest themselves in such a way that a correction at constant frequency may not be optimal. In some cases, a linear FM ("chirp") response may better match the response of the noise and thus be a better filtering mechanism.

4) Cross-channel Coherency Analysis: Current signal processing tools such as MatSeis, InfraMonitor and the Pure-State filter process multiple channels of data simultaneously to determine any channel-to-channel coherency that may exist. This correlation is a contributor to other products such as back-azimuth and phase velocity at the array. The MIDAS filter currently processes each data channel separately, however the additional data that may be exploited through array-level processing could add significant utility to future versions of the MIDAS filter.

# 9 References


Arrasmith, W., Coots, E., "Systems Engineering Modeling and Comparative Analysis of Various Infrasound Signals of Interest", International Journal of Modeling and Optimization, Vol 5, No. 3, June 2015

Arrowsmith, S., Marcillo, O., Drob, D., "A framework for estimating stratospheric wind speeds from unknown sources and application to the 2010 December 25 bolide", Geophysical Journal International, 2013, 195, 491-503

Arrowsmith, S., "Inframonitor Users Guide", Rev. 3.1, Dated 3/28/2012

Bass, Henry E., Hetzer, Claus H., "An Overview of Absorption and Dispersion of Infrasound in the Upper Atmosphere," *Inframatics,* Number 15, September, 2006.

Berchok, C., Bradley, D., Gabrielson, T., "St. Lawrence blue whale vocalizations revisited: Characterization of calls detected from 1998 to 2001", J. Acoust. Soc. Am. 120 (4), October 2006, pp. 2340-2354

Bedard, A., Georges, T., "Atmospheric Infrasound", Physics Today, March 2000, pp. 32-37

Bedard, A., "Low-Frequency Atmospheric Acoustic Energy Associated with Vortices Produced by Thunderstorms", National Oceanic and Atmospheric Administration/Environmental Research Laboratories/Environmental Technology Laboratory, Monthly Weather Review, Vol. 133, 2005

Bedard, A., Bartram, B., Keane, A., Welsh, D., Nishiyama, R., "The Infrasound Network (ISNET): Background, Design Details, and Display Capability as an 88D Adjunct Tornado Detection Tool", National Oceanic and Atmospheric Administration, Environmental Technology Laboratory

Blom, P., Marcillo, O., Arrowsmith, S., "Improved Bayesian Infrasonic Source Localization for regional infrasound", Geophysics Journal International, (2015) 203, 1682-1693

Bogert, B.P., Healy, M.J.R. and Tukey, J.W. in Proc.of the Symp. on Time Series Analysis, by M. Rosenblatt (Ed.), (1963) "The Quefrency Alanysis of Time series for Echoes: Cepstrum, Pseudo-Autocovariance, Cross-Cepstrum, and Saphe Cracking". Wiley, NY, pp 209-243.

Brown, P., D. ReVelle, R. Whittaker, Los Alamos National Laboratories News Release, May 2001

Capon, J., "High-Resolution Frequency-Wavenumber Spectrum Analysis", IEEE Proceedings, Vol. 57, No. 8, Aug. 1969, pp.1408-1418

Childers, D.G., Skinner, D.P. and Kemerait, R.C. (1977) "The Cepstrum: a Guide to Processing", Proc. IEEE, 65(10), pp1428-1443.

Christie, D., Kennett, B., "Detection of Nuclear Explosions Using Infrasound Techniques", Air Force Research Laboratory, Final Report (#AFRL-RV-HA-TR-2007-1151), 2007

Christie, D., "Recent developments in infrasound monitoring technology: application to CTBT verification", CBTO Spectrum 2007, Article XIV Conference special Edition (Issue 10)

Coots, E., Arrasmith, W., Skowbo, E., Olsen, J., Webster, B., "Target Detection and Classification From Sub-optimal Experimental Data Using Principal Component Analysis and Feature Vector Masking", International Journal of Modeling and Optimization, Vol 6, No. 2, April 2016

de-Groot-Hedlin, C., "Finite-difference time-domain synthesis of infrasound propagation through an absorbing atmosphere", *The Journal of the Acoustical Society of America*, 124, 1430, 2008

Eskicioglu, A. M., and Fisher, P. S., "Image quality measures and their performance", *IEEE Transactions on Communications*, vol. 43, no. 12, pp. 2959-2965, 1995.

Farges, T., Blanc, E., "Characteristics of infrasound from lightning and sprites near thunderstorm areas", Journal of Geophysical Research, Vol. 115

Frazier, W., Talmadge, C., Park, J., Waxler, R., Assink, J., "Acoustic detection, tracking, and characterization of three Tornadoes", J. Acoust. Soc. Am., 135, 1742 – 1751

Garces, M. and Hetzer, C., "Characterization of the Infrasound Field in the Central Pacific", Technical Report DTRA-TR-03-47, Prepared for the Defense Threat Reduction Agency, Fort Belvoir Virginia, June 2006

Garces, M., "Infrasonic signals generated by volcanic eruptions", IGARSS2000, IEEE2000 International Geoscience and Remote Sensing Symposium. Taking the

Pulse of the Planet: The Role of Remote Sensing in Managing the Environment. Proceedings (CAT. No. 00CH37120)

Green, D., Bowers, D., “Estimating the Detection Capability of the International Monitoring System infrasound network”, *Journal of Geophysical Research*, VOL. 115

Hale, M., Arrowsmith, S., Hayward, C., Burlacu, R., Pankow, K., Stump, B., Randall, G., Taylor, S., “Infrasound Signal Characteristics from Small Earthquakes”, *2010 Monitoring Research Review: Ground-Based Nuclear Explosion Monitoring Technologies*, Proposal No. BAA09-49

Hale, M., Arrowsmith, S., Hayward, C., “Infrasound Signal Characteristics From Small Earthquakes”, 2010 Monitoring Research Review: Ground-Based Nuclear Explosion Monitoring Technologies

Hedlin, M., Berger, J., “Evaluation of Infrasonic Noise Reduction Filters”, 23rd Seismic Research Review: Worldwide Monitoring of Nuclear Explosions, October 2-5, 2001

Hedlin, D., Raspet, R., “Infrasonic wind-noise reduction by barriers and spatial filters”, *The Journal of the Acoustical Society of America*, 2003

Horé, A., and Ziou, D., "Image Quality Metrics: PSNR vs. SSIM," *2010 20th International Conference on Pattern Recognition*, 2010, pp. 2366-2369

Jain, A. and Bhateja, V., "A full-reference image quality metric for objective evaluation in spatial domain," *2011 International Conference on Communication and Industrial Application*, 2011, pp. 1-5

Kijima, M., Miyagawa, Y., Oshita, H., Segawa, N., Yazawa, M., Yamamoto, M. “Poster Abstract: Multiple Door Opening/Closing Detection System Using Infrasound Sensor”, 2018 17th ACM/IEEE International Conference on Information Processing in Sensor Networks

Kim, K., Lees, J., Ruiz, M., “Acoustic multipole source model for volcanic explosions and inversion for source parameters”, Geophysical Journal International, 2012, 191, 1192-1204

Le Pichon, A., M. A. Garcés, E. Blanc, M. Barthelemy, and D. P. Drob (2002), “Acoustic propagation and atmosphere characteristics derived from infrasonic waves generated by the Concorde”, J. Acoust. Soc. Am., 111, 629 – 641

MATLAB, The Mathworks, inc. , www.mathworks.com

Masurkar, A., Daruwala, R., and Turkar, V., "A Novel Method to Remove Speckle from Polar Images using Morphological Operations," *2020 IEEE India Geoscience and Remote Sensing Symposium (InGARSS)*, 2020, pp. 126-129

McLaughlin, K., Gault, A., Brown, D., "Infrasonic Detection of Rocket Launches", US Army Space and Missile Defense Command, Contract No. DASG60-96-C-0064

Mittal, A. K. Moorthy and A. C. Bovik, "No-Reference Image Quality Assessment in the Spatial Domain," in *IEEE Transactions on Image Processing*, vol. 21, no. 12, pp. 4695-4708, Dec. 2012

Modrak, R.T., Arrowsmith, S.J. & Anderson, D.N., 2010, "A Bayesian framework for infrasound location", Geophysics Journal International, 181, 399-405.

Mutschlecner, J. P. and R. W. Whitaker (2005), "Infrasound from earthquakes", *Journal of Geophysical Research,* 110

O 'Day, D. Kelly, http://chartsgraphs.wordpress.com, January 31, 2011.

Olsen, J. V., and Szuberla C. A. L., "Processing infrasonic array data", *Handbook of Signal Processing in Acoustics*, V2, Havelock et al., eds, Springer Verlag, 2009

Olsen, J. V., "The Pure-State Filter: Applications to Infrasound Data", *U.S. Infrasound Team Meeting*, Oxford, MS., January 2009

Olsen, J, "Noise Suppression Using Data-Adaptive polarization Filters: Applications to Infrasonic Data", *J. Acoust. Soc. Am*., 72, 1456 – 1460

Oppenheim, A., Schafer, R., "Discrete-Time Signal Processing", Ch. 10, Fourier Analysis of Signals Using the Discrete Fourier transform, 3rd Edition, pp. 792-889

Palubinskas,G., "Mystery behind similarity measures mse and SSIM," *2014 IEEE International Conference on Image Processing (ICIP)*, 2014, pp. 575-579

Park, S., Ham, F., Lowrie, C., "Discrimination of infrasound events using parallel neural network classification banks", Nonlinear Analysis 63 (2005) e859 – e865

Pepyne, D., Zink, M., Brotzge, J., Knapp, E., Mendes, A., McCarthy, B., Klaiber, S., and Benito-Figueroa, B. “An Integrated RADAR-Infrasound Network for Meteorological Infrasound Detection and Analysis”

Revelle, D. O., “Acoustic-Gravity Waves from Impulsive Sources in the Atmosphere,” *Infrasound Monitoring for Atmospheric Studies,* pp. 305-359, Springer, 2010.

Ripepe, M., Marchetti, M., “Array tracking of infrasonic sources at Stromboli volcano”, Geophysical Research Letters, VOL. 29, NO. 22, 2076

Samson, J and Olson, J., “Data adaptive polarization filters for multi-channel geophysical data”, *Geophysics*, 46, 1423, 1981.

Sciotto, M., Cannata, A., Di Grazia, G., Gresta, S., Privitera, E., Spina, L., “Seismoacoustic investigations of paroxysmal activity at Mt. Etna volcano: New insights into the 16 November 2006 eruption”, *Journal of Geophysical Research: Space Physics*, 116

Shao, X.-M., and E. H. Lay (2016), “The origin of infrasonic ionosphere oscillations over tropospheric thunderstorms”, *Journal of Geophysical Research: Space Physics*, 121

Sheikh, H. R., Z. Wang, L. Cormack and A.C. Bovik, "LIVE Image Quality Assessment Database” Release 2, http://live.ece.utexas.edu/research/quality

Szuberla, C., Arnoult, K., Olsen, J., “Discrimination of near-field infrasound sources based on time-difference of arrival information”, J. Acoust. Soc. Am., (2006) 120

Szuberla, C., Olsen, J., Arnoult, K., “Explosion Localization via Infrasound”, J. Acoust. Soc. Am., (2009) 126

Talmadge, Carrick & Waxler, Roger & Kleinert, Daniel & Nava, Sue & Assink, Jelle & Buchanan, Hank. (2011). “Utah Testing and Training Range 2010: Large scale infrasound sensor deployment to Utah and Idaho”, *Journal of The Acoustical Society of America*

Tan, H. L., Li, Z., Tan, Y. H., Rahardja, S. and Yeo, C., "A Perceptually Relevant MSE-Based Image Quality Metric," in *IEEE Transactions on Image Processing*, vol. 22, no. 11, pp. 4447-4459, Nov. 2013

Teo, P. C., and Heeger, D. J., “Perceptual image distortion”, Proceedings of the 1st IEEE International Conference on Image Processing, pp. 982-986, 1994.

"The Infrasound Network and how it Works", https://www.ctbto.org/verification-regime/monitoring-technologies-how-they-work/infrasound-monitoring/

United Launch Alliance, Orbital Test Vehicle-1, Mission Overview, 2010, https://ula.bsshost.me/docs/default-source/news-items/av_otv_mob.pdf

Van der Weken, D., Nachtegael, M., and Kerre, E. E., "Image quality evaluation", *Proceedings of the 6th International Conference on Signal Processing*, vol. 1, pp. 711-714, 2002.

Venkatanath, N., Praneeth, D., Chandrasekhar, Bh. M., Channappayya, S. S. and Medasani, S. S., "Blind Image Quality Evaluation Using Perception Based Features", In *Proceedings of the 21st National Conference on Communications (NCC).* Piscataway, NJ: IEEE, 2015.

Walker, K., Zumberge, M., Berger, J., Hedlin, M., "Determining Infrasound Phase Velocity Direction With a Three-arm OFIS", 28th Seismic Research Review: Ground-Based Nuclear Explosion Monitoring Technologies

Wang, Z., and Bovik, A.C., "A Universal Image Quality Index," *IEEE Signal Processing Letters,* vol. 9, no. 3, pp. 81–84, March 2002.

Wang, Z., Bovik, A.C., Sheikh, H.R. and Simoncelli, E.P., "Image quality assessment: from error visibility to structural similarity," *IEEE Transactions on Image Processing,* vol.13, no.4, pp. 600- 612, April 2004.

Welch, P.D. (1967). "The Use of Fast Fourier Transform for the Estimation of Power Spectra: A Method Based on Averaging Over Short, Modified Periodograms," IEEE Trans. Audio Electroacoustics, Vol. AU-15, pp. 70-73.

Wijayakulasooriya, J., "Automatic Recognition of Elephant Infrasound Calls Using Formant Analysis and Hidden Markov Model", *2011 6th International Conference on Industrial and Information Systems*, ICIIS 2011, Aug. 16-19, 2011, Sri Lanka

# Appendix A

While this dissertation has dealt primarily with acoustic signals and sources, there exists an interesting analog between acoustic and electromagnetic wave theory. Any discussion on electromagnetic wave propagation, can begin with Maxwell's equations and specifically, Ampere's Law and Faraday's Law which deal with time-varying electric and magnetic fields. These two equations are shown below in integral form.

$$\oint_c \vec{E} \cdot dl = -\frac{d}{dt}\int_s \vec{B} \cdot ds \tag{A.1}$$

These laws state that the time-varying magnetic fields generate electric fields. The electric field, $\vec{E}$ along contour c is equal to the time varying magnetic flux density, $\vec{B}$ along surface s. The minus sign on the right-hand side indicates that the force of the induced electric field is in the direction which opposes the magnetic flux that is producing it. Known as Lenz's Law, this phenomenon explains the behavior of inductive elements which resist instantaneous changes in current. Equation A.2 (including the permeability, $\mu_0$ and the permittivity, $\varepsilon_0$) states that the time-varying electric fields generate magnetic fields.

$$\oint_c \frac{\vec{B}}{\mu_0} \cdot dl = \int_s \vec{J} \cdot ds + \frac{d}{dt}\int_s \in_0 \vec{E} \cdot ds \tag{A.2}$$

The magnetic flux, $\vec{B}$ along contour c is equal to the total current crossing surface s that is enclosed by contour c. The first term on the right-hand side, $\int_s \vec{J} \cdot ds$ represents the current due to charges crossing through surface s. The second term on the right-hand side, $\frac{d}{dt}\int_s \in_0 \vec{E} \cdot ds$ is the displacement current and represents the current due to the time-varying electric flux, $\in_0 \vec{E}$ crossing the area s, enclosed by contour, c. Considering Faraday's Law and Ampere's Law together, we see that electric fields and magnetic fields create each other. This behavior is what enables the propagation of an electromagnetic wave. The integral form of Maxwell's equations facilitates an easier, more intuitive understanding of propagation concepts, but they are limited to simple geometries. Of more value would be expressions that can explain the relationships between electric and magnetic fields for all points in space. Maxwell's equations written in differential form do just that by taking the limiting cases of the contours and surfaces used in the integral forms. To develop Maxwell's equations in differential form we start with Faraday's Law in integral form as shown below:

$$\oint_c \vec{E} \cdot dl = -\frac{d}{dt}\int_s \vec{B} \cdot ds \tag{A.3}$$

By applying Stokes' Theorem which provides a relationship between the line integral and the surface integral:

$$\int_l \vec{F} \cdot dl = \int_s curl\, \vec{F} \cdot ds \tag{A.4}$$

We can rewrite Faraday's Law as:

$$\oint_c \vec{E} \cdot dl = \int_s \nabla \times \vec{E} \cdot ds = -\int_s \frac{\partial \vec{B}}{\partial t} \cdot ds \tag{A.5}$$

which reduces to,

$$\nabla \times \vec{E} = -\frac{\partial \vec{B}}{\partial t} \tag{A.6}$$

This is the differential form of Faraday's Law, which indicates that the curl of the electric field, $\vec{E}$ is equal to the decreasing magnetic flux density at that point. Again, emphasizing the opposing relationship of Lenz Law.

Similarly, we can develop the relationship for Ampere's Law by starting with the integral form:

$$\oint_c \frac{\vec{B}}{\mu_0} \cdot dl = \int_s \vec{J} \cdot ds + \frac{d}{dt}\int_s \epsilon_0 \vec{E} \cdot ds \tag{A.7}$$

Applying Stokes' Theorem we can rewrite the above as:

$$\oint_c \frac{\vec{B}}{\mu_0} \cdot dl = \int_s \nabla \times \frac{\vec{B}}{\mu_0} \cdot ds = \int_s \vec{J} \cdot ds + \int_s \frac{\partial \epsilon_0 \vec{E}}{\partial t} \cdot ds \tag{A.8}$$

which reduces to:

$$\nabla \times \frac{\vec{B}}{\mu_0} = \vec{J} + \frac{\partial \epsilon_0 \vec{E}}{\partial t} \tag{A.9}$$

Equation A.9 states that the curl of the magnetic field divided by the permeability, $\frac{\vec{B}}{\mu_0}$ is equal to the current density, $\vec{J}$ and the derivative of the electric field, $\frac{\partial \epsilon_0 \vec{E}}{\partial t}$.

The above expressions for Ampere's and Faraday's Laws in differential form explain the relationship between electric and magnetic fields. Since we are interested in the propagation of these fields, we can now develop the wave equations that exist beyond the influence of the point charges that initially created the electric and magnetic fields. Without the influence of the source charges, we can zero-out the current density, $\vec{J}$ due to the absence of charge motion and re-write equations (A-6) & (A-9) as:

$$\nabla \times \vec{E} = -\frac{\partial \vec{B}}{\partial t} \quad and \quad \nabla \times \frac{\vec{B}}{\mu_0} = \frac{\partial \epsilon_0 \vec{E}}{\partial t} \tag{A.10}$$

To better understand the propagation behavior of the electric and magnetic fields, we wish to use the above equations but decouple the electric and magnetic fields. Applying the curl operator to the Ampere's Law expression above, we can write:

$$\nabla \times \nabla \times \vec{E} = -\frac{\partial}{\partial t} \nabla \times \vec{B} \tag{A.11}$$

Substituting in the left-hand side of the Faraday Law expression above gives us:

$$\nabla \times \nabla \times \vec{E} = -\frac{\partial}{\partial t}\left(\mu_0 \epsilon_0 \frac{\partial \vec{E}}{\partial t}\right) = -\mu_0 \epsilon_0 \frac{\partial^2 \vec{E}}{\partial t^2} \tag{A.12}$$

or:

$$\nabla^2 \vec{E} - \mu_0 \epsilon_0 \frac{\partial^2 \vec{E}}{\partial t^2} = 0 \tag{A.13}$$

Equation A.13, above, is known as the homogeneous vector wave equation for the electric field in a source-free region.

Similarly, we can isolate the magnetic flux density, $\vec{B}$ by applying the curl operator to Faraday's Law above to get:

$$\nabla \times \nabla \times \vec{B} = -\mu_0 \epsilon_0 \frac{\partial}{\partial t} \left( \nabla \times \vec{E} \right) \tag{A.14}$$

Substituting the right-hand side of Ampere's Law into the above equation gives us:

$$\nabla \times \nabla \times \vec{B} = -\mu_0 \epsilon_0 \frac{\partial}{\partial t} \left( -\frac{\partial \vec{B}}{\partial t} \right) = \mu_0 \epsilon_0 \frac{\partial^2 \vec{B}}{\partial t^2} \tag{A.15}$$

or:

$$\nabla^2 \vec{B} - \mu_0 \epsilon_0 \frac{\partial^2 \vec{B}}{\partial t^2} = 0 \tag{A.16}$$

This expression is known as the homogeneous vector wave equation for the magnetic field in a source-free region.

Going back to the analogy to acoustic wave theory, sound pressure and velocity are analogous to the electric and magnetic fields. For example, the Ampere's Law equation above which describes the change in the magnetic field with respect to time, which is modulated by the permeability, $\mu_0$ and the permittivity, $\varepsilon_0$. Having a similar form, the acoustic wave equation shown is below:

$$\rho_0 \nabla \left[ \frac{1}{\rho_0} \nabla p \right] - \frac{1}{c^2} \frac{\partial^2 p}{\partial t^2} = 0 \qquad \text{(A.17)}$$

where $\rho_0$ is the instantaneous density of the medium and p is the pressure.

Equation A.17 describes the change in the pressure, p of the acoustic wave as it is modulated by the velocity of sound propagation, c. In the analysis of an infrasound or seismic signal, of particular interest is the change in sound pressure level versus time when considering that the propagated sound energy is proportional to the density, $\rho_0$, of the medium through which it is moving. Analogously, the study of a propagating electromagnetic wave often considers the change in electric or magnetic field intensity versus time, recognizing that the propagation of the electromagnetic energy is proportional to the permeability, $\mu_0$ and the permittivity, $\varepsilon_0$, of the medium through which it is moving.